Force microscopy of magnetic nanoparticles

James Claxton

Thesis submitted for the degree of Master of Science in Physics

60 Credits

Department of Physics

Faculty of Mathematics and Natural Sciences

UNIVERSITY OF OSLO

May 2021

Force microscopy of magnetic nanoparticles

James Claxton

Acknowledgment

I would like to thank all those who supported directly or indirectly towards the submission of this master thesis.

Abstract

Biologically produced nanoparticles have attracted considerable attention for their significant potential application in biomedicine and industrial processes. In this thesis, atomic and magnetic force microscopy is used to characterise the size, location, and magnetic properties of palladium and palladium iron nanoparticles. Imaging shows that these nanoparticles are localised extracellularly and possibly in the periplasmic space. The signal above palladium-iron nanoparticles, of size 50 ± 10 nm, suggests significant magnetic behaviour, and palladium nanoparticles show possible magnetic activity. The magnetic signals also suggest that the nanoparticles behave as superparamagnetic or ferromagnetic nanoparticles.

List of abbreviations

MFM	Magnetic force microscopy
AFM	Atomic force microscopy
Pd	Palladium
Pd-Fe	Palladium-iron

Contents

1 Introduction **1**

2 Theory and background **2**

2.1 Magnetic nanoparticles 2

2.1.1 Magnetic materials 2

2.1.2 Magnetic nanoparticles and superparamagnetism 3

2.1.3 Palladium nanoparticles produced by bacteria 5

2.2 Scanning probe microscopy measurements of magnetic nanoparticles 6

2.2.1 Comparison of AFM & MFM to other methods 6

2.2.2 AFM basic principles 7

2.2.3 Modes of AFM 7

2.2.4 AFM channels 10

2.2.5 Spring systems 11

2.2.6 Laser detection in AFM 13

2.2.7 Principles of MFM 16

2.2.8 Direction of sensitivity 17

2.2.9 Challenges and possible solutions in MFM measurements 18

2.2.10 Artefacts 19

2.2.11 Convolution effects of the tip and sample 22

3 Materials & methods **24**

3.1 Production of nanoparticles with bacteria 24

3.2 List of samples and tip specifications 24

3.3 Size and location of nanoparticles 25

3.4 Isolating magnetic interaction from short-range surface interaction and background interaction 26

3.5 Comparison of MFM and AFM probes 26

3.6 Data Analysis 26

3.7 Sample mounting and laser alignment 29

4 Results **31**

4.1 Size and location of nanoparticles 31

4.2 Properties of samples specific to the application of MFM (sample A) 36
4.3 Isolating magnetic interaction from short-range surface interaction and background interaction 39
4.3.1 Background interaction 39
4.3.2 Short-range surface interaction 39
4.3.3 Force spectroscopy 43
4.3.4 Comparing magnetic signals from Pd-Fe and Pd nanoparticles (samples A and B) 45
4.4 Comparison of MFM and AFM probes 48
4.4.1 Apparent size of nanoparticles and bacteria (Samples A and C) 48
4.4.2 Force spectroscopy (Sample C) 50
4.5 MFM artefacts and interpreting the signals 52
4.5.1 Micrometre resolution imaging 52
4.5.2 Nanometre resolution imaging 53
4.5.3 Nanometre resolution imaging 2 54

5 Discussion **56**
5.1 Size and location of nanoparticles 56
5.2 Properties of samples specific to the application of MFM 57
5.3 Isolating magnetic interaction from short-range surface interaction and background interaction 58
5.3.1 Background interaction 58
5.3.2 Short-range surface interaction 58
5.3.3 Comparing magnetic signals from Pd-Fe and Pd nanoparticles (sample A and B) 59
5.4 Comparison of MFM and AFM probes 60
5.5 MFM artefacts and interpreting the signals 61

6 Conclusion **62**

7 Future Outlook **63**

A Comparison of MFM and AFM probes **70**

B MFM artefacts and interpreting signals **71**

C Sequential magnetic mapping - NAP 2020 **72**

1 Introduction

Palladium (Pd) nanoparticles have excellent catalytic, physical, chemical and optical properties [1]. This has led to novel experiments that show the use of palladium nanoparticles for antimicrobial applications [2], as catalysts [3,4], and in anti-cancer treatment [5]. Pd, though often non-magnetic, is known to be near a magnetic instability, and in size range, 2 - 16 nm, shows ferromagnetic behaviour [6, 7]. In addition, small amounts of nickel added to Pd can stabilise ferromagnetic behaviour even in bulk [6, 8]. The addition of iron could also have the same effect. If magnetism can be stabilised in Pd and Pd-Fe nanoparticles, this would be very beneficial since magnetic nanoparticles are an avenue of growing interest for applications in biomedical nanotechnology [9–12].

However, physicochemical methods for producing nanoparticles are damaging to the environment [13,14]. Therefore, a biological route has gained interest [15,16], but we do not know enough about the properties of biologically synthesised Pd nanoparticles. Magnetic force microscopy (MFM) could be a valuable tool for their characterisation. MFM allows the measurement of the ultra-low magnetic field with nanoscale spatial resolution and the simultaneous measurement of the topography. MFM is a scanning probe technique operating as a mode of atomic force microscopy (AFM) using a tip with a magnetic coating. MFM and AFM will be explained later in more detail. Despite the research of characterising nanoparticles using MFM [17–22], there is little to no research done on Pd or Pd-Fe nanoparticles using MFM. For this reason, research is necessary to characterise these biologically synthesised nanoparticles and to study how the MFM tool can characterise them.

The main goal of this thesis is to explore how MFM can be used as a tool for characterising the location, size, and magnetic properties of bacterially produced palladium and palladium-iron nanoparticles.

The sub-goals of this thesis are the following:

1. To investigate where the nanoparticles produced by bacteria are located and their size. More specifically, investigating whether they are outside or inside the bacteria or inside the bacterial membrane. In addition, to find out if measurements of the same bacteria across several cross-sections can provide more information of where the nanoparticles are localised and their quantity.

2. Use the MFM method to investigate the samples' material differences and how the measure-

ments change with MFM parameters.

3. To investigate if AFM and MFM can be used to isolate the magnetic interaction from the short-range surface interaction and possible electrostatic/background interaction.

4. To investigate sources of artefacts and to study how to interpret the signals.

The outline of this thesis is as follows. Chapter 1 is this introduction. Chapter 2 covers background and theory. First presented is an overview of magnetic materials in nanoparticle form, how they differ from the material in bulk, and a brief discussion on the biological synthesis of Pd nanoparticles. Following this, the method of AFM is introduced, covering the basic principles, modes, and signals measured. Then, the MFM method is introduced, explaining possible ways to isolate magnetic interaction from other interaction. Following this, possible artefacts in AFM and MFM are discussed, and the work done by others to interpret signals.

Chapter 3 introduces the samples, the nanoparticle production process, and the data analysis methods. In addition, the method for using the AFM is explained, and how to mount the samples. Chapter 4 shows the results of the experiments, which is discussed in Chapter 5. Finally, in Chapter 6, conclusions are written, and avenues of possible future work are outlined.

2 Theory and background

2.1 Magnetic nanoparticles

2.1.1 Magnetic materials

We can classify materials by their magnetic properties based upon how they behave in a magnetic field. A paramagnetic or diamagnetic response manifests itself if an applied field induces a weak positive or negative magnetisation, respectively. This magnetisation disappears when the field is turned off—ferromagnetic materials, on the other hand, exhibit remnant magnetisation (Fig. 2.1). After a magnetic field is applied to the material and subsequently removed, the material remains magnetised. They, therefore, also show features of hysteresis (Fig. 2.1). Hysteresis is a phenomenon in which the magnetic history of the material affects its current magnetic state. It originates in the fact that energy is required to rotate domains in a magnetic material.

Magnetic domains are the smallest unit of magnetic order in a magnetic material. Magnetic

order is determined not just by a single atom but is a collective phenomenon originating in the inter-atomic exchange interaction between atomic moments. Anisotropy in crystals causes the spins to couple with the preferential anisotropy direction. The distance with which electron spins remain in the same direction in ferromagnets defines the size of a magnetic domain [23, 24]. In bulk, there is competition between this short-range exchange interaction and the long-range magnetostatic interaction to reduce the magnetic energy of the system. This competition results in the re-orientation of the domains.

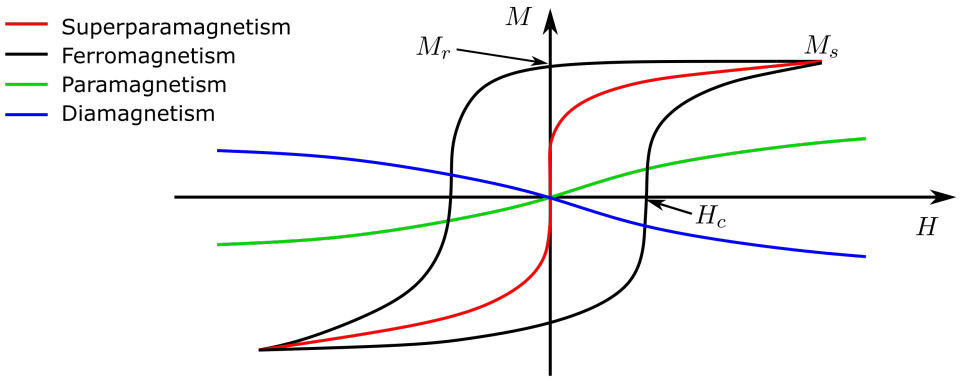

Figure 2.1: Schematic of a hysteresis loop, characterising different magnetic behaviour. On the x-axis is applied magnetic field H, and on the y-axis is magnetisation M. As indicated, M_s is saturation magnetisation, M_r is remanence magnetisation, and H_c is the coercive field.

2.1.2 Magnetic nanoparticles and superparamagnetism

Nanoparticles differ from their bulk counterpart due to surface and quantum effects [7,25,26]. As the surface-to-volume ratio increases, several property changes occur: hysteresis is no longer evident in magnetisation curves [27], ferromagnetic behaviour is replaced by superparamagnetic behaviour [6] (Fig. 2.1), and magnetic order appears in previously considered non-magnetic materials [7].

Applying a magnetic field to bulk magnetic material will begin to align the domains in the direction of the applied field until it is saturated. Magnetic saturation is when all the domains are aligned, and hence, the magnetisation will increase no further even if a larger magnetic field is applied. If one could isolate a magnetic domain by removing its neighbouring domains, it would still have a strong internal magnetic field. By definition, single domains have saturated magnetisation since they have no other neighbouring domains to align with. Typically, a single-domain particle has a diameter of less than 100 nm [25].

The difference in properties between materials in bulk and single-domain is due to the differences between domain wall movement and spin reversal, respectively. Since a single domain has no domain walls, the magnetisation vector can be rotated only via spin reversals [28]. By applying a magnetic field, the magnetic domain wall movement in bulk requires much less energy than the reversal of a single magnetic domain. For this reason, moving from multi-domain to single-domain structures leads to an increase in coercivity. Coercivity is the resistance to change in magnetisation. The size at which magnetic particles have the highest coercivity is in the region between 10 and 100 nm in diameter, although this is material dependant [25]. Reducing the diameter below this size causes the coercivity to drop to zero, entering the so-called superparamagnetic regime [25].

The coercivity of tiny single-domains rapidly drops to zero because thermal effects begin to cause rapid spin reversals. The magnetic behaviour of single domains is dependent on their temperature, as well as size. In uniaxial symmetry, the direction of magnetisation of single magnetic domains rotates parallel to some easy axis (Fig. 2.2a). Without any applied magnetic field, the magnetic moment of the domain has the same probability of being in either direction along the easy axis. This is illustrated by the well (solid line) in Fig. 2.2b. The magnetic moment is reversed between the two directions by thermal excitation over the energy barrier, i.e. when $kT > KV$, where k is Boltzmann's constant, T is the temperature of the particle, K is the magnetic anisotropy energy, and V is the volume of the particle. This energy barrier leads to a temperature known as the blocking temperature since it freezes or blocks spin reversals in the domain. The blocking temperature defines a value above which spins have enough thermal energy to overcome the anisotropy barrier KV. However, this blocking temperature is not an intrinsic property of the material or nanoparticle. It changes depending on the experiment [25].

By applying a magnetic field H, the direction of the magnetic moment is perturbed, causing a greater probability of the magnetic moment being in one direction than the other, as shown by the dotted line in Fig. 2.2b.

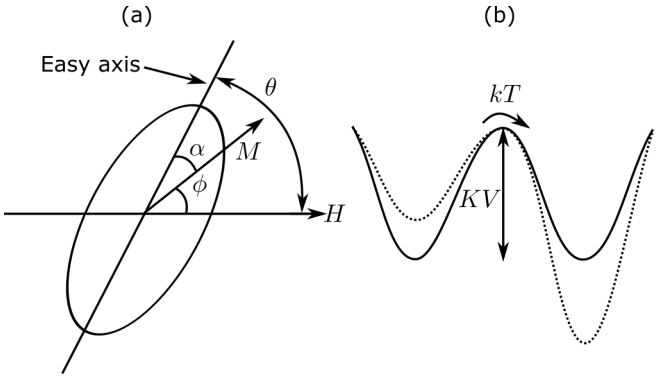

Figure 2.2: (a) Schematic of a prolate spheroid showing the direction of magnetisation M of a superparamagnetic nanoparticle at an angle ϕ to an applied magnetic field H. θ gives the angle between the applied field and the anisotropy axis. (b) The magnetic potential energy as a function of the angle α. The minima occur at $\alpha = 0$ and π. The solid line indicates the potential without any applied field, and the dashed line indicates the potential in a field applied along the anisotropy axis.

The reason that magnetic order appears in non-magnetic material when in nanoparticle form is due to surface atoms [6]. In nanoparticles, the surface-to-volume ratio is much greater than in bulk. For this reason, there are more surface atoms. Surface changes such as vacancies, broken bonds, and lattice strain cause a disordered region of spins at the surface. The magnetic anisotropy in nanoparticles can increase by up to two orders of magnitude due to these surface atoms [29, 30].

Pd, specifically, is known to be near a magnetic instability in bulk, having a high density of states close to the Fermi energy. The addition of 2.3% Ni is enough to stabilise ferromagnetism in bulk Pd [6, 8]. The addition of iron could also give similar results since iron, like nickel, is ferromagnetic. In [6], Pd nanoparticles of various sizes (2, 3, 5 and 10 nm) were studied. The authors found that the magnetisation was approximately inversely proportional to particle size. This proportionality suggests a core/shell structure in Pd. More specifically, a structure with a magnetic surface and a non-magnetic core.

2.1.3 Palladium nanoparticles produced by bacteria

Despite Pd nanoparticles' volume of applications [3–5], the current processes of producing Pd nanoparticles can be energy-intensive [14]. For this reason, new methods of creating these nanoparticles more efficiently are very desirable [31], and a biological solution has gained much inter-

est [15, 16].

The biosynthesis of nanoparticles, in general, is of interest since the process is less costly, can be done at lower temperatures and pressures, and with non-toxic chemicals [32] in comparison to physicochemical treatments [13]. Also, it is possible to scale up the biosynthesis for industrial production [33]. Biosynthesis of nanoparticles has been done with plants [34, 35], but microorganisms are found to perform better due to their larger surface-to-volume ratio. The process by which bacteria produce nanoparticles begins with an uptake phase in which the bacteria take metal ions from the solution outside the bacteria. Next, in the reduction phase, the bacteria reduce the metal ions to form nanoparticles. Metal ions can be reduced in several locations: inside the cell (intracellular), outside or on the cell's surface (extracellular), or in the periplasmic space. For Pd nanoparticles, biosynthesis was first done by Lloyd et al. in 1998 [36] using *Desulfovibrio desulfuricans*. The palladium nanoparticles were localised on the surface of the cell (extracellular) and in the periplasmic space.

Next, we will introduce the AFM and MFM methods and examine how they can be applied to the study of nanoparticles.

2.2 Scanning probe microscopy measurements of magnetic nanoparticles

2.2.1 Comparison of AFM & MFM to other methods

MFM, which is within the class of scanning probe techniques, is highly useful for measuring magnetism on the nanoscale [17, 37]. MFM is an operational mode of AFM, both of which were developed in 1986-1987 [38, 39]. The difference being, MFM operates with a magnetic probe and AFM with a non-magnetic probe. The MFM probes are often manufactured by coating an AFM probe with magnetic material. Compared to other methods, the advantage of MFM is in the spatial resolution, which can be down to 10 nm [37]. This resolution is possible due to advanced low noise electronics [22] and the development of sharp tips. Sharp tips with a small radius of curvature at the tip apex allow only a small volume to interact with the sample as it scans. For this reason, both AFM and MFM are very successful instruments for characterising nanoparticles and surfaces on the nanoscale [40].

The advantages of MFM over other techniques, such as superconducting quantum interference devices (SQUIDs), magnetic resonance force microscopy (MRFM) and Hall probes, is that MFM

can be used in various environments [41], which can be specific to the application. MFM can be used in ambient conditions, ultra-high vacuum, and at low temperatures. Usually, some conditions in the environment need to be maintained through the experiment, which is possible with MFM. Specific to measuring magnetism, MFM is beneficial, compared to the alternative methods above, when resolution is necessary below 1 μm [41]. In addition, in contrast to more traditionally used transmission or scanning electron microscopy, MFM allows the simultaneous measurement of the topography and the magnetic signal [17].

2.2.2 AFM basic principles

The basic principle of AFM is that a cantilever with a tip at the end is moved in the z direction above a surface (Fig. 2.3). Attractive and repulsive forces acting between the tip and the sample causes the cantilever to deflect. A laser, reflected at the top of the cantilever, hits a photodetector, and the signal is measured.

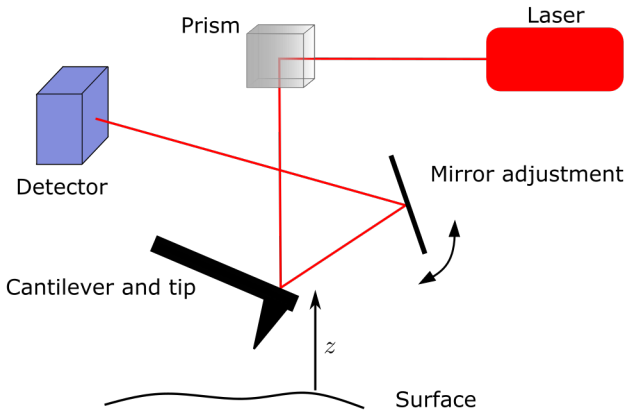

Figure 2.3: Schematic showing the laser reflected at the top of the cantilever. The laser is sent through a prism, reflected at the cantilever, reflected again at a mirror before finally arriving at the detector.

2.2.3 Modes of AFM

Here is an outline of some of the AFM modes which this thesis uses. First, we will cover AC mode, contact mode, and force spectroscopy before going onto lift mode/two-pass technique, common in MFM.

AC/tapping mode: AC mode involves oscillating a cantilever with a tip at the end and scanning above a surface. As the tip scans, it interacts with the surface, which in turn causes the cantilever to deflect, and the laser and detector measures the cantilever deflection. Typically, the cantilever is driven near to its resonance frequency. If the cantilever and tip are far away from any surface or force potential, the cantilever will oscillate with some "free" amplitude, A_0. Extending the oscillating cantilever towards the surface causes the amplitude to change. By interacting with the surface causes A_0 to reduce to an amplitude A. Via the feedback loop in the AFM, the amplitude A remains at a constant value. The AFM-user controls this value of A (so-called the "setpoint"). In AC mode, the setpoint is in Volts. The z-piezo is responsible for adjusting the height of the cantilever above a surface to fulfil this damping requirement on the amplitude – i.e. making sure the actual amplitude of the cantilever is as close as possible to the setpoint throughout the scan.

Hence, by enforcing the setpoint, the force with which the tip taps the sample's surface is also controlled. For this reason, rather than directly measuring the height surface features, the AFM is probing the height by applying a constant force. Another effect of enforcing a setpoint is a shift in the effective resonance frequency and effective spring constant, possibly resulting in instabilities. These instabilities are further mentioned in section 2.2.5.

Using AC mode, J. Legleiter [42], demonstrated through simulation and experiment that increasing the setpoint led to a decrease in the tapping force of the probe for all drive frequencies. Applying a greater tapping force, in turn, leads to significantly more compression of the surface during scanning. Also presented in [42], is that the maximum tapping force during one oscillation of the cantilever was greater for harder surfaces. The total tapping force over one complete oscillation was the same for hard and soft surfaces – since this is kept constant by the setpoint. However, tapping the softer material, the peak force was less than the peak force measured while tapping the harder material. Whilst, the duration of contact with the softer material was longer than the harder material.

The Lennard-Jones potential can describe the interaction between atoms at short distances. The potential is a sum contribution from van der Waals interaction, an attractive potential and the repulsive Pauli interaction, which sets in at close distances. In AC mode, the tip intermittently makes contact with the surface in the attractive part of the potential (Fig. 2.4).

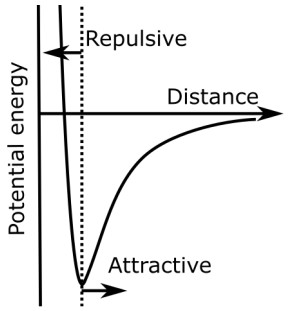

Figure 2.4: Schematic of the Lennard-Jones potential.

Contract mode The tip is in constant contact with the surface in contact mode, operating in the repulsive region (Fig. 2.4). Contact mode is not appropriate, however, for soft samples, which this strong interaction could damage.

Force spectroscopy: In force spectroscopy, the cantilever is displaced only vertically by the z-piezo. It does not do line scans. At a chosen point on the sample, the microscope takes measurements while changing the tip-sample distance. Force spectroscopy is advantageous since it is of interest to find how the tip-sample interaction changes with the vertical distance.

Lift mode/two-pass technique: The lift mode/two-pass technique is an extension of AC mode. After the first scan (normal AC mode), the z-piezo raises the probe upwards, away from the surface (Fig. 2.5). The AFM performs the second pass by oscillating the probe at the resonance frequency, while the piezoelectrics move the probe to follow the topography measured during the first pass. The result is that in the second pass, the tip-sample distance is constant throughout the scan. This tip-sample distance is called the lift height. The AFM repeats the two passes for each line, which builds an image. In both the first and second pass, all six information channels are recorded, which are explained in the next section.

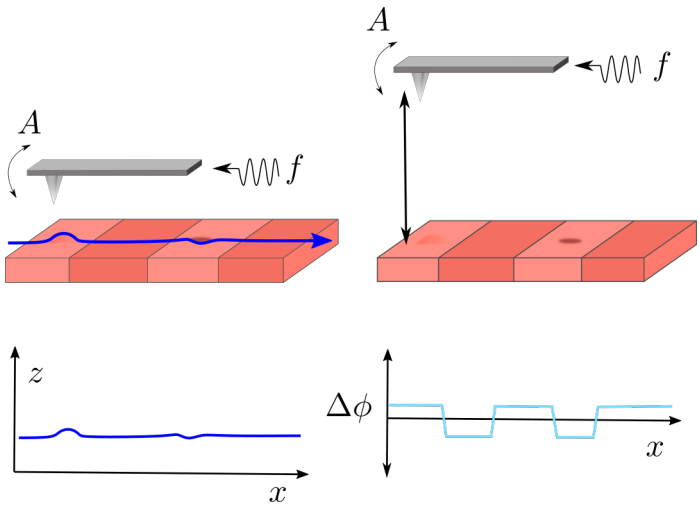

Figure 2.5: Lift mode/two-pass technique schematic. The first pass measures the topography close to the surface, as indicated in the lower left, showing z against x. Next, in the second pass, the piezoelectrics move the tip to follow the topography to achieve a constant lift height. A constant lift height means that the tip is approximately always the same distance from the surface. In the second pass, the phase shift, compared to the drive frequency f, is recorded. The phase shift $\Delta\phi$ as a function of lateral displacement x is shown in the lower right. The dark red indicates regions containing magnetic material.

2.2.4 AFM channels

As the cantilever and tip scan a surface, in total, there are six channels of information recorded by the AFM. These are the height, the amplitude of oscillations, the phase shift of the oscillations from the drive frequency, the error signal, the vertical deflection, and the height (measured) – which is an alternative to the first height channel. The AFM measures both the height and height (measured) channel via the feedback loop. The height (measured) channel is similar to the regular height channel; however, it accounts for the error in the piezoelectrics. The z-piezo, used to move the cantilever, can suffer from non-linearity due to hysteresis when a voltage is applied. For this reason, the AFM is fitted with a capacitive sensor to account for the non-linearity of the z-piezo. This capacitive sensor measures the length of the z-piezo and makes corrections, recorded in the height (measured) channel. The height (measured) channel is recommended instead of the regular height channel for scanning rough surfaces with height features over 100 nm. The JPK Nanowizard (which is the model of AFM used in this thesis) manual recommends calibrating the height channel every six months due to the hysteresis of the z-piezo.

As the oscillating cantilever scans a surface, there is a change in phase, amplitude, and oscillation frequency due to the surface force gradient. It is not proportional to force itself, as is presented by the following equations. Due to the sample force gradient, the shift in the cantilever oscillation amplitude A, phase ϕ and resonance frequency f_0 are:

$$\Delta A = \frac{A_0 Q_c}{2k_c^2}\left(\frac{dF_z}{dz}\right)^2 \tag{1}$$

$$\Delta\phi = -\frac{Q_c}{k_c}\frac{dF_z}{dz} \tag{2}$$

$$\Delta f_0 = -\frac{f_0}{2k_c}\frac{dF_z}{dz}, \tag{3}$$

where Q_c is the quality factor of the first resonance in air, k_c is the spring constant of the cantilever in air, A_0 is the amplitude at the resonance frequency f_0 in air - without external forces, F_z is the force in the z-direction, and z is the distance along the z-direction [43]. At edges or rapid changes in height over small lateral distances, transients appear. These transients occur because the feedback loop is trying to return the probe amplitude to the setpoint value. The error signal and deflection channels can be used as an indication of these transients.

2.2.5 Spring systems

The main things which characterise the behaviour of the scanning tip at close distances to a surface are the tip geometry, the force function, and the compliance or stiffness of the tip. We first take a look at the geometry of the tip. The radius of the tip apex influences the interaction between it and the surface. The proportionality between the tip radius and adhesion (attractive) forces is linear [44, 45]. Hence, the larger the tip radius, the greater the adhesion forces between the tip and surface. A tip with a sizeable interacting volume and surface could lead to undesirable artefacts. Artefacts will be discussed in later sections. A tip with a small radius has the advantage that forces can be measured more quickly. This results in negligible viscous forces and less tip contamination [44]. Tip contamination is when the tip picks up a piece of the sample and scans with the piece attached.

Second, we look at the force function. Because AFM is probing the height by applying a constant force, AFM cannot easily distinguish a smooth surface with heterogeneous forces from a rough surface with homogeneous forces. The additional heterogeneity could be electrostatic

forces, capillary forces, viscous forces, adhesion forces, and more [44]. Hence, AFM results can be ambiguous since the tip is influenced by different forces and at different degrees as it scans. This interaction makes recording the topography of a surface a challenge. In addition, it is also important to note that van der Waals forces are not the same between materials [46]; the interaction between the tip and a heterogeneous surface (in terms of surface material) can lead to different interaction.

Thirdly we look at compliance or stiffness. The location at which the stress or strain on the cantilever is measured is not the same as where the force is acting. In AFM, the location where the force is measured is effectively at the top side of the cantilever. The forces acting on the tip cause the cantilever to deflect, and the deflection is measured. However, the forces are only acting on the end of the tip. What mediates the force measurement between these two locations is the compliance of the tip material and the cantilever's spring constant. When the tip interacts with the surface, it is extended and compressed. This behaviour is not taken into account in the measurements.

There can be jumps in the measurements in a general system with spring due to the effective spring constant. Fig. 2.6a shows a general spring system where plate A moves in and out, while plate B is fixed. A distance D separates the two smaller plates. The top smaller plate is attached to A by a spring. As plate A is moved inwards, there is a jump from D_1 to D_2. The cause of this jump is that the effective spring constant is lower than the maximum slope of the force curve. Similar jumps going outward are seen from D_3 to D_4. These jumps will occur as long as K is finite.

These instabilities can be further shown using amplitude-distance curves. In Fig. 2.6b, the curve shows a jump where it moves from a region that is attractive to a region that is both repulsive and attractive. There are three regions: the attractive, repulsive, and switching region [47]. In the attractive region, the peak amplitude is shifted slightly to a lower frequency (see Fig. 2.6b inset). For this reason, it is common practice to select a drive frequency that is a little to the left of the resonance peak in AC mode. In the repulsive region, at close distances, the opposite slope is measured. The peak amplitude is shifted a little to a higher frequency. At intermediate distances, there is the switching region. This region is the most unstable region to perform measurements. The oscillation frequency makes jumps stochastically, causing instabilities and artefacts, which distort results.

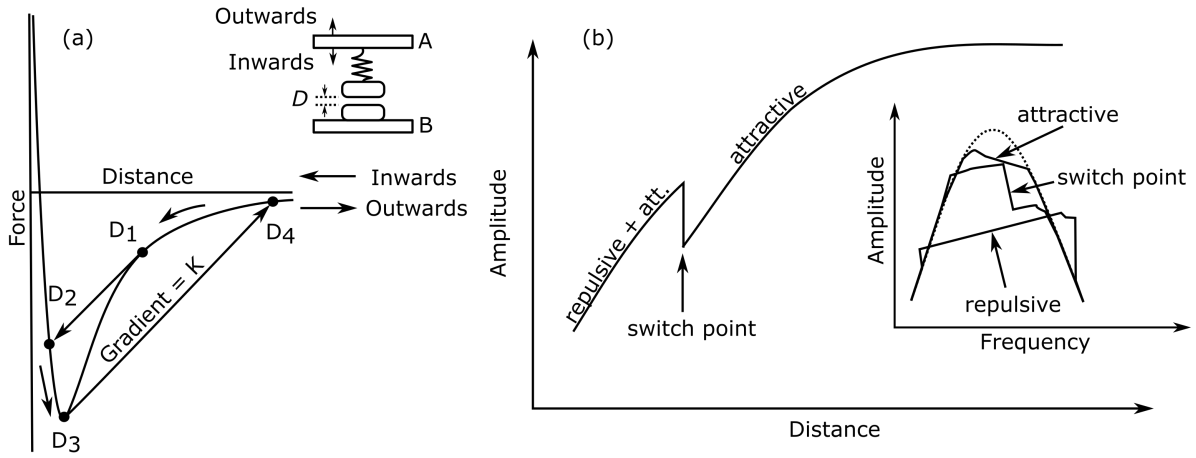

Figure 2.6: (a) Force distance curve of two objects, with one attached by a spring, as shown in the inset. In force measuring techniques with springs, instabilities occur when the effective spring constant is lower than the maximum slope of the force curve. (b) Schematic of the switching point which can occur due to changes between attraction and repulsion.

2.2.6 Laser detection in AFM

Essentially, what is being detected in AFM is the deflection of the cantilever. The cantilever is deflected when the tip interacts with the sample. This deflection causes the laser beam to be displaced at the photodiode detector. In this section, the minimum detectable deflection of the cantilever Δz_{min} will be analysed. This value is essential since its significance determines how effective AFM is at detecting nanoparticles. The signal from the photodiode is further transformed using a lock-in amplifier to extract a meaningful signal from the noise. Noise can be a result of air pressure and vibrations, which affect the cantilever.

Firstly, we will look at the sensitivity of the signal at the photodiode to the deflection of the cantilever. The size of the laser spot D at the photodiode from the ray optics is given by the equation,

$$D = D_0 \frac{L}{L_{foc}}, \tag{4}$$

where D_0 is the size of the lens aperture (see Fig. 2.7), L is the cantilever-photodiode distance, and L_{foc} is the lens-cantilever distance [48]. The size of the laser spot at the photodiode D can be made arbitrarily small by changing the aperture and distances, as shown by Eq. 4. In the ideal case, D must be as small as possible for laser detection to be as precise as possible. However, the laser

beam reflected at the top of the cantilever is also a diffracted beam, which is of great importance to consider. For this reason, in practice, the largest possible value for D must be used, constrained by both diffraction and ray optics. Hence, considering diffraction, the wavelength of the laser λ is

$$\lambda = dsin(\alpha) \approx d\frac{D}{L}, \tag{5}$$

where d is the size of the laser spot on the top of the cantilever and α is the angle of incidence [48]. The re-arranging gives

$$D \approx \frac{\lambda L}{d}, \tag{6}$$

which shows that d can be increased to make the laser spot at the photodiode smaller. However, this is limited by the size of the cantilever [48]. It is also possible to use smaller wavelengths, but this introduces greater power, resulting in the thermal drift of the cantilever. Next, we consider the total intensity of the laser at the photodiode S_0, which can be written as

$$S_0 = S_{area}D^2 \tag{7}$$

where S_{area} is the intensity or irradiation power per unit area [48]. The laser dot is assumed to be square with uniform intensity to simplify the equations. Realistically it would be Gaussian [48]. For different segments, the current I at the photodiode is assumed to be proportional to S_A and S_B, which are the intensities at segments A and B, respectively. Although two segments are used in these equations for simplicity, the AFM model used in this thesis has four segments. The difference in intensity between these two segments is

$$S_A - S_B = S_{area}2\Delta xD, \tag{8}$$

and using

$$\Delta x = 2\theta L, \tag{9}$$

which can be found from Fig. 2.7, since bending the cantilever by an angle θ, the laser beam is reflected by an angle 2θ [48]. This is because the angle of incidence equals the angle of reflection. Hence,

$$S_A - S_B = S_{area}2\Delta xD = \frac{S_0}{D^2}4\theta LD. \tag{10}$$

Now inserting Eqs. 5 and 9 gives

$$S_A - S_B = 6S_0 \frac{\Delta z}{l} \frac{d}{\lambda}. \tag{11}$$

The current at the photodiode can therefore be written as

$$I = \frac{6RS_0 d}{\lambda l} \Delta z, \tag{12}$$

where R is the sensitivity. The ratio of current I to deflection Δz is called the detection sensitivity [48].

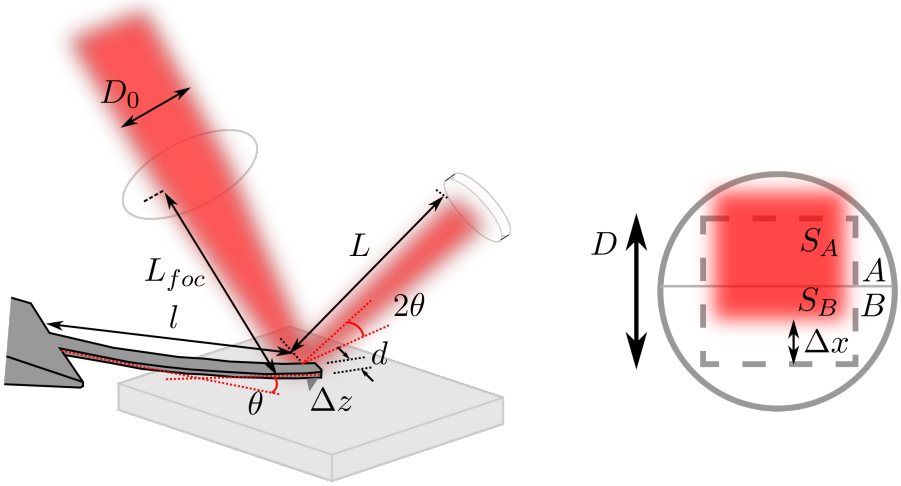

Figure 2.7: Schematic view of the laser beam reflected at the top of the deflected cantilever onto the photodiode. The inset on the right shows the laser spot at the photodiode. The laser spot (red) is assumed to be square to simplify the equations. The AFM model used in this thesis has four segments, however, only two (A and B) are shown here.

The source of noise at the photodiode comes from the shot noise. Photons that interact with the detector create a signal, i.e. current of electrons. The expression for current $I = Q/t$ can be expressed in terms of the number of electrons n flowing in a time interval Δt. The current through segment A is

$$I_A = \frac{en}{\Delta t}, \tag{13}$$

where e is the electron charge. If the time interval is large, the measurement of the current will be more precise. However, this would, in turn, reduce the scanning speed. The time interval can

also be expressed through a frequency, which is the largest frequency possible without great loss of signal or corresponding bandwidth B, which relates to the time interval: $B = 1/\Delta t$. The current at segment A will fluctuate with the number of charges, which is on average a fluctuation of $\sqrt{n}$. The shot noise at A is therefore

$$\Delta I_{shot,A} = eB\sqrt{n} = eB\sqrt{\frac{I_A}{eB}} = \sqrt{eBI_A}. \tag{14}$$

The total shot noise at the detector is therefore

$$\Delta I_{shot} = \sqrt{\Delta I_{shot,A}^2 + \Delta I_{shot,B}^2} = \sqrt{2e(I_A + I_B)B} = \sqrt{2eRS_0B}. \tag{15}$$

Following this, the photocurrent I (estimated in Eq. 12) with respect to shot noise can be expressed as

$$\frac{I}{\Delta I_{shot}} = \frac{6dS_0R\Delta z_{min}}{l\lambda\sqrt{2eS_0RB}}. \tag{16}$$

Re-arranging and replacing the ratio of I and ΔI_{shot} with the ratio of signal S to noise N, the minimum detectable deflection of the cantilever is

$$\Delta z_{min} = \frac{\lambda l}{6d}\frac{S}{N}\sqrt{\frac{2eB}{S_0R}}. \tag{17}$$

By estimation of the parameters in Eq. 17, the result for Δz_{min} is 0.2 pm [48]. This value suggests that the scanning technique has very high detection sensitivity, ideal for studies of nanoparticles. Next, we will examine how the AFM setup is changed for MFM using a magnetic tip.

2.2.7 Principles of MFM

In MFM, the tips used are typically coated with a 20 – 30 nm layer of hard magnetic material. By applying this magnetic coating to the tip, the tip interacts non-magnetically, like AFM, and magnetically with the sample. Typically, the case in studying magnetic materials with MFM is that the magnetic interaction is of interest and needs to be separated from the non-magnetic interaction. Separating magnetic and non-magnetic interaction is not a trivial problem, and it is an active field of research [19, 49–51]. As was the case in explaining surface effects on the topography measurements with AFM, the MFM cannot distinguish between magnetic interaction and non-magnetic interaction. The interaction leading to the deflection of the probe is a superposition of all forces acting on it. Although we are interested in separating the non-magnetic and magnetic interaction, the non-magnetic interaction is still crucial to measure the sample's topography.

As explained before, MFM and AFM using lift mode work by making two line scans of the sample. The first scan records the topography, and in the second scan, the probe is moved to a bigger height and follows the path of the measured topography. The purpose of the second scan is to move to a range at which short-range forces are not significant. If the tip is simply moved vertically 50 nm from the sample at one point, this may only be 10 nm from the sample at another point above the surface. Surfaces are rarely perfectly flat on the nanoscale. The solution is to make the distance between the sample and the probe constant at all points. For this reason, the first pass is essential.

Once the topography is known, the AFM can keep the tip-sample distance constant at all points above the sample, preventing changes in the interaction from short-range van der Waals force. Therefore, change in van der Waals interaction due to height modulation is removed. The interaction which remains in the second pass is therefore only long-range interaction, ideally only magnetic. However, electrostatic interaction can also be a factor, which will be explained in the section on challenges and possible solutions in MFM measurements.

In order to measure magnetic nanoparticles, which are possibly superparamagnetic, a strong permanent magnet (MFM magnet) is placed below the sample holder. This magnet stabilises the magnetic moment in one direction and prevents it from flipping, as mentioned in theory. Next, we will look at the component of the force to which MFM is sensitive.

2.2.8 Direction of sensitivity

In Fig. 2.8, the tip is connected at the end of the cantilever and, therefore, the component of force, which contributes to the deflection of the cantilever is $F_n = \hat{n} \cdot F$, where $\hat{n}$ is normal to the cantilever axis. Hence,

$$F' = \frac{dF_n}{dn} = \hat{n} \cdot \nabla F_n = \hat{n} \cdot \nabla(\hat{n} \cdot F). \tag{18}$$

The direction $\hat{n}$ should not be confused with $\hat{z}$, which is the sample normal since the cantilever axis is not necessarily parallel to the sample. Therefore $F' = dF_z/dz$ is an approximation. As seen in Fig. 2.8, the red lines indicate the MFM signal, which results from the tip interacting with the vertical component (grey arrows) of the sample stray field.

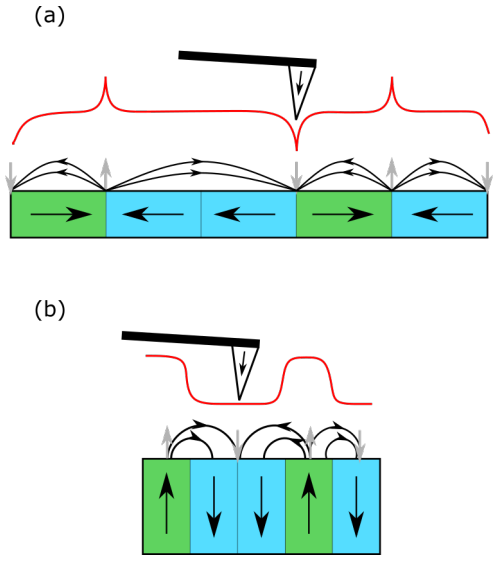

Figure 2.8: Schematic showing the principle of MFM scanning over a sample surface with (a) in-plane and (b) out-of-plane magnetisation. The MFM tip detects the vertical component of the stray field (grey arrows) emanating from the surface. Hence, the MFM signal (in red) exhibits changes at domain boundaries.

2.2.9 Challenges and possible solutions in MFM measurements

Long-range interaction from electrostatic forces can be present in addition to magnetic forces. Electrostatic interaction can be due to capacitive effects between the tip and surface [52]. This interaction can lead to phase shift maps with similar features to the topography, i.e. mirroring the topography. The origin of capacitive coupling effects is that the force gradient due to the capacitance of the tip is much greater closer to the surface (first pass) than at a greater height (second pass). Therefore, the decrease in force gradient, resulting from moving to a greater height, leads to a positive phase shift measured in the second pass. On the other hand, magnetic force should only be attractive if the nanoparticles are aligned with the MFM magnet and tip. These capacitive coupling effects can be presents no matter if the surface is conducting or insulating [53].

Several methods [49, 54, 55] have been developed in order to remove the contribution from electrostatic interaction between the tip and sample in MFM. These methods typically require changes to the MFM set up to perform them, or require the use of another technique in conjunction with MFM. One method, proposed by Angeloni et al. [49], involves controlling the magnetic state of the tip, so-called controlled magnetisation (CM-MFM). The first step in CM-MFM is to characterise

the tip by measuring the saturation magnetisation and coercivity of the tip. Angeloni et al. obtained these quantities using a floppy disk and an electromagnet. Observing when the magnetic contrast was strongest or weakest indicated when the tip had reached saturation or was demagnetised, respectively. After the tip was characterised, the sample of nanoparticles was placed in the MFM. Then, a magnetic field was applied to saturate the tip; this is the same procedure as in regular MFM. The magnetic field was then turned off, and subsequently, a scan was performed above the sample. After that, a negative magnetic field was applied so that the tip was in a demagnetised state. As before, the magnetic field was turned off, and another scan was performed. In this second scan, only the van der Waals and electrostatic interaction were recorded since the tip was not interacting magnetically with the sample. By subtracting the contrast of the first and second image, Angeloni et al. were able to obtain images with only magnetic contrast remaining.

Another possibility to remove the effects of capacitive coupling is by adding a dielectric layer between the tip and substrate [21, 50]. This is a relatively new technique being used [17, 56–58], which can be done by embedding the sample in a dielectric material. Krivcov et al. found that by incorporating a dielectric layer in their sample preparation by embedding their sample, capacitive coupling effects decreased with increasing dielectric thickness.

However, there seems to be a conflict in the literature regarding electrostatic interaction in MFM. Several authors [49, 54, 55] take the stance that active measures need to be performed to remove the electrostatic contribution to the phase shift. Therefore some literature has been found to include MFM images, which are not related to magnetism [59]. In [20], the authors mention that no studies compare magnetic and non-magnetic nanoparticles under the same conditions.

On the other hand, some authors state that since the nanoparticles are likely saturated magnetisation, due to the strong MFM magnet, the electrostatic interaction is not significant compared to the magnetic interaction [18]. Because of the differing points of view, the possibility of electrostatic interaction should be considered in experiments. MFM setups and samples are all different, and therefore, different requirements are expected for them.

2.2.10 Artefacts

An artefact is usually defined as something, which is not naturally occurring. Artefacts are, therefore, the result of the experimental procedure itself, which imposes uncharacteristic modifications of the signal. Sources of artefacts are from the tip, external magnetic field, sample surface, feed-

back parameters, and piezo-scanners [60]. Vibrations, acoustic noise, thermal gradients can also be factors that decrease the quality of images. These artefacts can appear as unusual contrast features, contours, height shifts and changes in apparent resolution. Artefacts can also arise due to direct contact between the sample and the tip. In some cases in AC mode, it is possible to pick up nanoparticles or pieces of the sample and to continue scanning with them [49]. As is the same with systematic error, these artefacts should be identified, and their causes understood to avoid the pitfalls in the sample study. For this and other reasons, which are beyond the scope of this thesis, MFM has remained mainly a qualitative tool.

Specific to the case of MFM, studies show that inhomogeneity in the MFM setup [61] and tip-sample interaction [62] lead to modification of the measured MFM signal. Therefore, this research is of great importance, which deepens our understanding of the effects imposed on the MFM signal. This is especially important, since the standard practice for the study of superparamagnetic nanoparticles is to apply an external magnetic field to the sample.

Another possible source of artefact is tilted oscillations and misalignment of tip magnetisation. These effects can give rise to contrast symmetry, with dark and light contrast on opposite sides along the scanning direction [62]. Ideally, the probe should only be interacting with the out-of-plane component of the sample stray field. This ideal case leads to the equations explained in the theory section (Eq. 2). A tilted tip is sensitive to in-plane and out-of-plane magnetic field components. This is because some of the tip magnetisation is in the direction of the plane and out of the plane (Fig. 2.9). The tip magnetisation, usually oriented perpendicular to the cantilever, is therefore tilted with respect to the sample normal and possibly the MFM magnet. During scanning, the tip oscillates and interacts with the sample in-plane magnetic stray field due to the tilt. Because of the tip interacting in this way, contrast symmetry appears with dark and light contrast observed along the cantilever's direction (Fig. 2.10). The AFM instrument used in [62] was NT-MDT which has a 20° tilt angle. The instrument model used in this thesis is JPK NanoWizard, which has a 10° tilt angle [63].

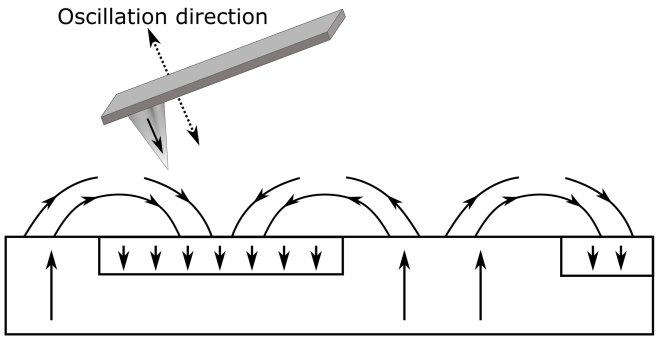

Figure 2.9: Schematic diagram of a source of artefact during scanning arising from the tilt angle between the tip and the sample normal and or MFM magnet.

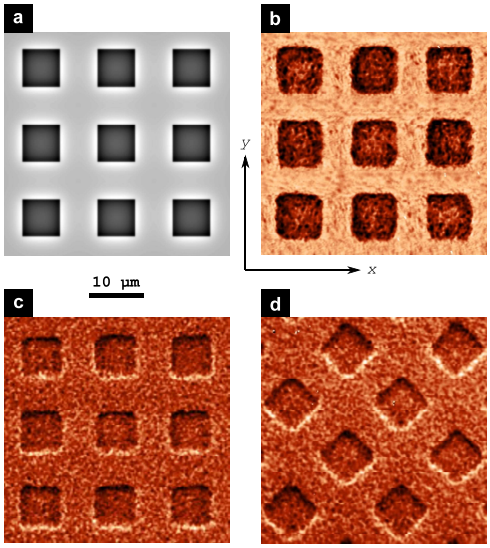

Figure 2.10: (a) shows a calculated map of the stray-field at 100 nm above a patterned SmCo film. (b) shows a phase map done with a flexible cantilever. (c) and (d) show phase maps measured with a stiff cantilever, with (d) rotated by an angle of 45 degrees. Dark and light contrast appears on opposite sides of the squares, showing two-fold contrast symmetry. This figure is taken from [62] ©2011 IEEE.

Some authors [64, 65], have differentiated between artefacts and actual magnetic signal by applying a magnetic field in the sample plane direction. This can also distinguish between magnetic

interaction and van der Waals interaction between the probe and sample. In [64] simulations are made of single-domain cobalt (Co) nanoparticles of the size 20 – 50 nm in diameter. They show these Co nanoparticles in different field strengths. Firstly when the external magnetic field, H_{ext}, is greater than the coercive field of the probe, H_t, the particle is uniformly magnetised in the direction of H_{ext}. The phase contrast of the simulation is shown in Fig. 2.11a. When the external magnetic field is greater than even the coercive field of the probe H_{ct}, stripes of contrast appear in the image (Fig. 2.11b). They concluded that this contrast transformation allows the separation of the contribution from magnetic interaction and van der Waals interaction since van der Waals interaction does not exhibit change under magnetic field.

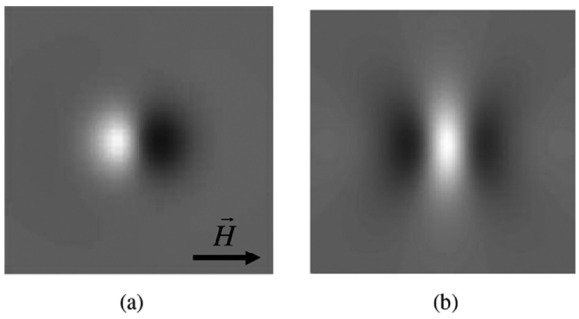

Figure 2.11: MFM contrast simulated for spherical Co particle with 50 nm diameter in the strong external field. (a) $H_{ext} > H_t$. (b) $H_{ext} > H_{ct}$. Scanning height is 50 nm. This figure is taken from [64]. 2007 ©IEEE.

2.2.11 Convolution effects of the tip and sample

This section discusses some limitations in AFM and MFM due to the size effects of the tip on measurements. MFM has a much greater spatial resolution (down to 10 nm) than, for example, SQUIDs. For this reason, MFM is suitable for characterising individual nanoparticles. Still, it is widely only used qualitatively since tip-sample interaction and configuration of the tip's stray field are not well-understood [37]. This is the case with many probe microscope techniques [66].

One limitation is that the MFM tip is convolved with the stray field of the sample at every point. In AFM the same occurs when measuring the topography. The knowledge that the images produced

by MFM is a convolution between the tip and the sample has some important implications. Lateral displacement cannot be quantitatively accurate. Since the tip has a finite size, any feature in the sample appears to have some dimensions or size. This does not necessarily mean that the tip radius, at the apex, is the minimum resolution of the microscope [18, 67]. It has been reported that the resolution is better than this. Nevertheless, the geometry of the tip does impact the measurement. As seen in Fig. 2.12, during the line scan, the geometry of the AFM tip convolves with the topographic features of the sample. For this reason, the lateral size of nanoparticles is not a good indicator of diameter. A better indicator is the height since the height of the nanoparticle does not enter into the convolution [18, 67].

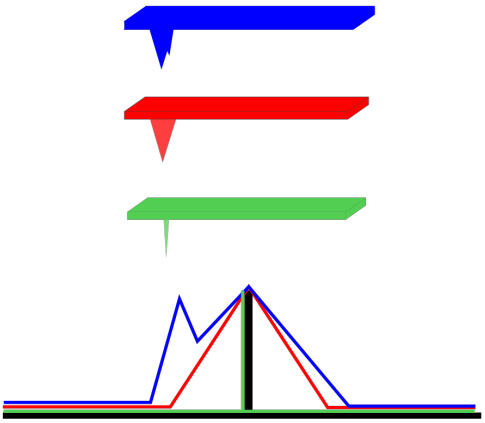

Figure 2.12: Figure showing how a topographic feature of the sample, in black, results in three different mappings corresponding to the different tips used to perform the measurements, as shown by the blue, red, and green tip, and lines.

In summary, this outlines some of the problems which can arise in MFM. Next, we will look at how the samples are produced and the methods used in this thesis to perform the experiments.

3 Materials & methods

3.1 Production of nanoparticles with bacteria

The nanoparticles in the samples were produced biologically. Escherichia coli BW25113 strain was used in the sample production of samples A, B and C (see Table 1). Solutions of sodium tetrachlopalladate and iron III chloride were added to the bacteria (in sample A), and sodium formate was used to start the reduction reaction. A washing process was done to remove any remaining solution around the bacteria, and then the bacteria were embedded in a resin. Afterwards, the samples were sliced with a diamond knife into approximately 0.5 μm thick slices, ready for study with the AFM. Please see the paper [68] in appendix C for the detailed production process.

3.2 List of samples and tip specifications

In Table 1, the list of samples studied in the thesis is shown. Each sample is given a name (A, B, and C) used throughout the text. The relative quantity of Pd to Fe in sample A is approximately 4.8:1, from EDX analysis. However, the analysis was not complete, and therefore this is used only as an estimate.

Table 1: List of the samples studied. The material and relative quantity is shown.

Sample name	Materials	Relative quantity
sample A	palladium and iron	Pd:Fe, 4.8:1
sample B	palladium	N/A
sample C	palladium and copper	N/A

The AFM instrument used in this thesis is JPK Nanowizard 4.0. The MFM tips used are manufactured by Nanosensors (Switzerland), model PPP-MFMR. The probe material is silicon with a hard magnetic coating on the tip and aluminium coating on the back/top of the cantilever. The AFM tips used are DP14 / Hi' Res-W/AIBS, manufactured by Mikromasch (Bulgaria). The specifications of the AFM and MFM tips are shown in Table 2.

Table 2: The specifications of the tips used. Nominal values are shown, which is given by the manufacturer.

Property	AFM probe	MFM probe
Resonance frequency (kHz)	160	75
Probe width (μm)	35	27
Probe length (μm)	125	224
Probe thickness (μm)	2.0	3.1
Force constant (N/m)	5.7	2.8
Tip height (μm)	20 - 30	10 - 15
Tip radius of curvature (nm)	1	≤ 50
Tip coercivity (Oe)	N/A	300
Tip remanence magnetisation (emu/cm^3)	N/A	300

3.3 Size and location of nanoparticles

The software ImageJ was used to find the size distribution of nanoparticles in the phase maps recorded above sample A. The scale of the image was set using the "Set Scale" tool. Afterwards, the region of interest was cropped from the whole image and converted to an 8-bit image (greyscale). Next, the "Threshold" tool was used to isolate the nanoparticles from the image. Some nanoparticles were erased from the image since they appeared as large clusters and could not be separated into smaller sections. Then, the "Analyse Particle" tool was used to measure the area and diameter of the nanoparticles.

Mapping sequential slices of resin were done by first finding a place on the sample with at least 2 or 3 slices of resin next to each other. The position of the cantilever was measured with respect to the resin slice in the optical camera window. This allowed the cantilever to be positioned approximately in the same position on each slice. Sections between 20 μm and 60 μm in width were imaged with a low scan rate (0.5 Hz) to locate the bacteria in sequential slices of resin. Usually, one would not be imaging so big areas at once. However, this was the most straightforward method since large areas were needed to ensure the same position in each slice was located. After the same area was indeed found, smaller regions were imaged. It took considerable effort to locate the same bacterium between slices, but was possible. Afterwards, the sections were stitched together in ImageJ to build a larger image of each slice.

3.4 Isolating magnetic interaction from short-range surface interaction and background interaction

Analysis was done on measurements to investigate the background and electrostatic interaction. A strong permanent magnet was used to demagnetise the tip when the AFM head was removed from the stage. The magnetic state of the tip was not checked after demagnetising, and therefore, could still have some remanent magnetisation. This is similar to CM-MFM, where the second scan is done with a demagnetised tip. However, in CM-MFM, the magnetic state of the tip is checked by imaging a piece of a floppy disk with the MFM. This was not done, and therefore the tip can be said to be pseudo-demagnetised.

In order to compare the signals from magnetic and non-magnetic probes, some samples were scanned sequentially with first the MFM and then the AFM probe. The sample was left in place while the cantilevers were exchanged. The microscope was used to re-position the tip in the exact location as with the previous probe.

In force spectroscopy measurements, the region of interest was first imaged in AC mode, and then the mode was changed to force spectroscopy. Force spectroscopy measurements were done in quick succession to avoid changes in the position of the tip due to drift. It was noticed that after doing force spectroscopy measurement and then returning to AC mode and imaging again, that the piezo had drifted slightly.

3.5 Comparison of MFM and AFM probes

In order to measure the behaviour of the AFM and MFM tips under the same conditions, measurements were taken on sample C without the MFM magnet. This should result in only non-magnetic interaction taking place between the sample and tip. This was done by placing sample C on a glass slide and then imaging in lift mode (two-pass technique) with an MFM tip, and subsequently removing it, and replacing it with an AFM tip, and scanning the same area. In this experiment, the MFM and AFM setpoints were equal to 0.3 V or otherwise specified in the results.

3.6 Data Analysis

In order to remove the background phase shift from the MFM magnet below the sample, three methods were tested to remove this. The first approach for subtracting the background phase shift

from the MFM magnet was to take the whole phase shift map, calculate the mean, and then shift all the values in the map such that the mean was equal to zero. Fig. 3.1b shows the results of zeroing the mean of mappings at several heights and then plotting the phase shift of three nanoparticles. The phase shift shown is not monotonic with increasing height from the surface. This behaviour was not expected since the pure magnetic signal should decay with increasing height. In addition, the MFM phase shift is greater than the AFM phase shift, and although the probes have not been compared (this will be mentioned later), this is unlikely.

The phase maps used in Fig. 3.1b are plotted as histograms in Fig. 3.1a. This shows the phase shift value of each pixel and the number of times (count) it appears in the phase shift map. Less than 20 nm from the surface (indicated by orange and blue in Fig. 3.1a), the distribution of pixels follows a Gaussian distribution and does not appear to be skewed. Further from the surface, e.g. at 20 nm, however, the distribution of pixels are skewed. The reason the distribution of pixels is skewed is likely that further from the surface, the background is less significant compared to the phase shift from the nanoparticles. Even at big heights, the nanoparticles could still create a large phase shift measured by the tip, which skews pixel distribution. This suggests that zeroing each mapping's mean to subtract the background is not a good approach to use as it varies with height.

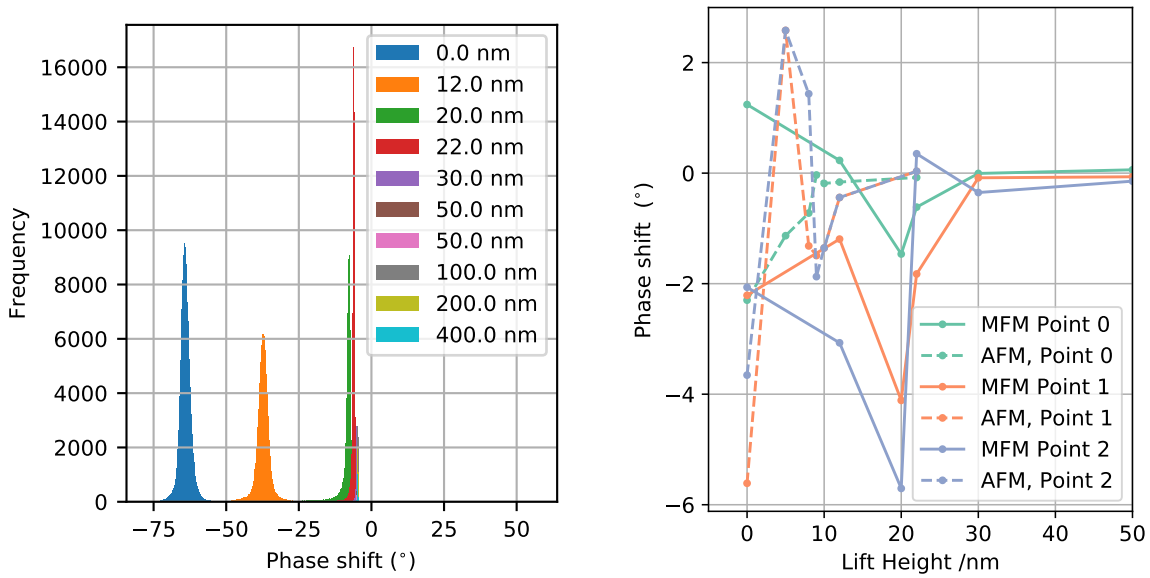

(a) (b)

Figure 3.1: (a) Distribution of pixels at several lift heights. The x-axis gives the phase shift of the pixels, and the y-axis indicates the frequency (count) of the pixel value appearing in the image. The legend indicates the lift height of each image distribution. (b) MFM phase shift above three nanoparticles in sample A, after subtracting the mean from each phase shift map.

The second method used was to subtract the background phase shift by looking at individual line scans within the phase maps. The limitation of this method is that the phase shift can have a significant variance across each line scan. It was challenging to distinguish between the background phase shift from the MFM magnet and the phase shift resulting from interaction with the nanoparticles. Hence, this also is not seen as a suitable method.

The third method was to ensure that some region in the imaging process was without nanoparticles. This section of the phase map could then be used to estimate the mean and standard deviation of the phase shift from the background. After the mean and standard deviation of this region was used, the phase shift from nanoparticles became monotonic, which is expected. This method is used in the data analysis of images in this thesis unless otherwise specified. All python scripts written for the data analysis can be found at the following GitHub address: `https://github.com/jamesbc123/magnetic_force_micro_repo.git`.

The roughness of the topography was calculated in the JPK software. The following equations

show how these calculations are made for both the RMS and Ra roughness. The RMS roughness, or the root-mean-squared roughness, is the standard deviation of the height values from the mean in a given area.

$$RMS = \sqrt{\frac{\sum_{i=1}^{N} (Z_i - Z_{ave})^2}{N}}, \tag{19}$$

where Z_i is the height value, Z_{ave} is the mean height, and N is the total number of height measurements in the given area. Ra roughness, is the average deviation of the height values from the centre plane going through the given area.

$$Ra = \frac{\sum_{i=1}^{N} |Z_i - Z_{cp}|}{N}, \tag{20}$$

where Z_{cp} is the height of the central plane.

3.7 Sample mounting and laser alignment

The procedure for mounting the probe was done with latex gloves to keep the AFM head clean. Fine tweezers were used to move the tip so as not to scratch the AFM head. These steps ensure that the glass remains in good condition for the laser to pass through. If the glass block becomes dirty with debris, the best way to clean it is to apply nitrogen gas. As much as possible, the head was handled carefully, not to make contact with the polished sides when mounting the tips and picking up the glass block. Once the tip and AFM head are mounted to the AFM instrument (Fig. 3.2a), the next step is to align the laser on the back of the cantilever. This alignment is performed in conjunction with an optical camera to see the laser spot. Using the two alignment screws for the laser (Fig. 3.2b), the laser spot was positioned at the very end of the cantilever. The voltage sum on the photo-detector should be at maximum. Next, the mirror screw was tuned to get the lateral voltage as close as possible to 0.0 V. The mirror screw was very sensitive. Attention should be taken to ensure that the sum remains maximum during this mirror tuning process (although it may change slightly). Next, the two detector screws were used to align the vertical voltage to zero. This can quickly be done using the crosshairs in the laser alignment panel. Finally, the laser filter was placed on top of the AFM to prevent reflection around the AFM casing and contact human eyes. Once the sample holder (see Fig. 3.2b) is placed under the AFM head, either before or after aligning the laser, the tip is ready for tuning and approaching the sample. The placement of sample on the holder should be done so that the area of interest is positioned in the centre of the MFM magnet. Tuning the probe resonance frequency should be done before approaching the surface.

Also, ensuring that the stepper motors are disengaged is essential. If it is engaged, this prevents the approach to the surface.

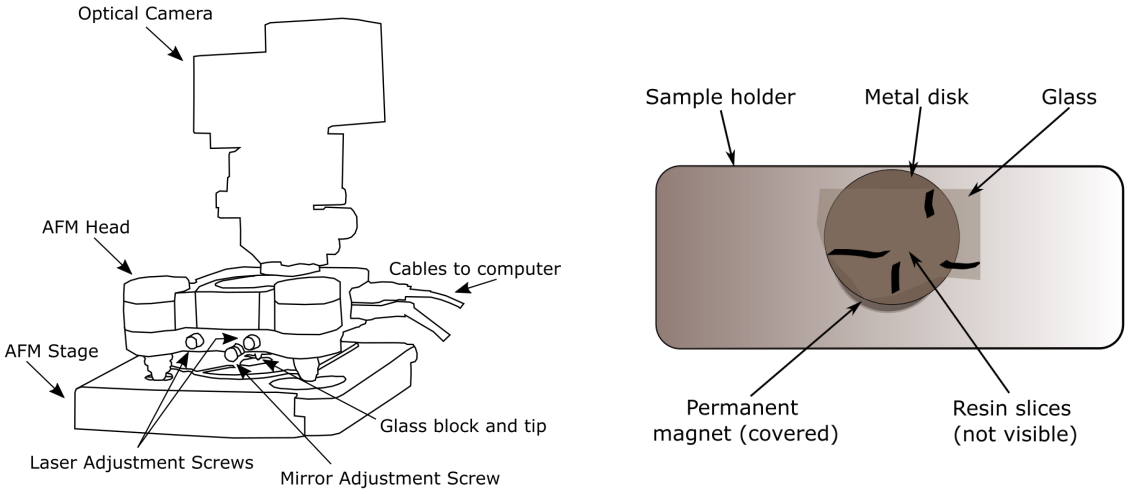

(a) (b)

Figure 3.2: (a) Figure showing the AFM instrument. Here the AFM head is mounted on to the AFM stage, as would be during measurements. The optical camera above is used to locate regions of interest on the sample. The adjustment screws are used in the laser alignment process. (b) The sample holder with a metal disk mounted. On the metal disk is the smooth glass, and sitting on the glass are the slices of resin. These slices are not visible in the figure. Below the metal disk is a 0.58 T permanent magnet, which is also not visible as it is below the metal disk. Black marks are drawn on the glass to help indicate where the resin slices are for measurements.

4 Results

4.1 Size and location of nanoparticles

MFM was used to characterise the size and location of nanoparticles with respect to the bacteria in sample A. Fig. 4.1a-c shows MFM height maps recorded on sample A. Fig. 4.1a shows three bacteria cross-sections, with large clusters of nanoparticles which appear to be attached to the outside of their membranes. The bacterium on the right is imaged in higher resolution (4.1b), and two nanoparticles are again imaged in higher resolution in Fig. 4.1c. The nanoparticles appear to be mostly covered by resin, with some parts exposed, as indicated by the dashed area in the bottom right. Fig. 4.1d shows the topography/height along the lines A and B. The size of the nanoparticles is estimated by how much is above the surface. However, it could be that this measurement is only the top surface of the nanoparticles.

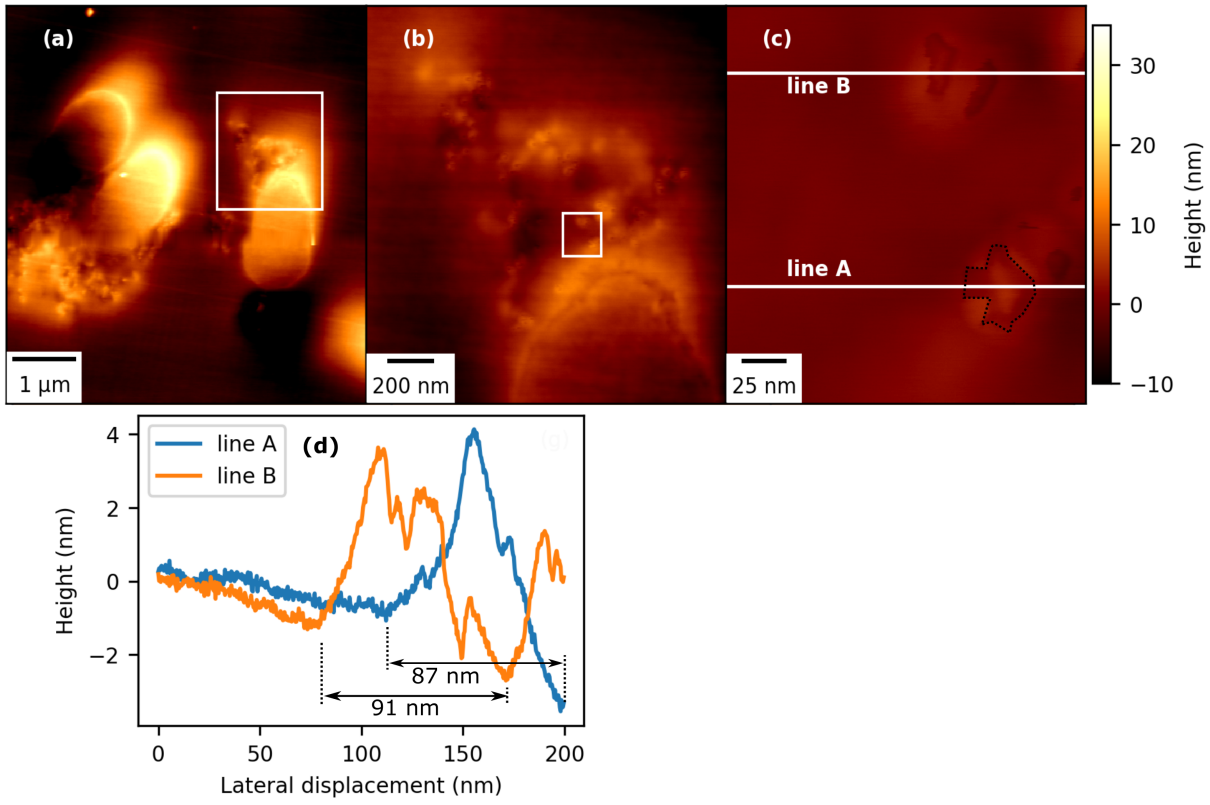

Figure 4.1: Topography of sample A, showing bacteria and nanoparticle locations. (a), (b) and (c) show MFM height maps, each is a higher resolution map of the previous, as indicated by the white boxes. (d) MFM topography along lines A and B.

Since the nanoparticles appear to be partially covered in resin, the size of the nanoparticles is not easily found from the topography. One option to estimate nanoparticle size is to use the "magnetic size" measured above the surface. Fig. 4.2a-b show the height and phase map of several cross-sections of bacteria with nanoparticles surrounding them. The phase map is recorded at 19 nm above the sample surface. In Fig. 4.2c, a cropped region after filtering and particle analysis is shown. The mean nanoparticle diameter, calculated from the black dots in Fig. 4.2c is 50 ± 10 nm, out of a total of 32 nanoparticles. In Fig. 4.2d, a histogram of the diameters is shown.

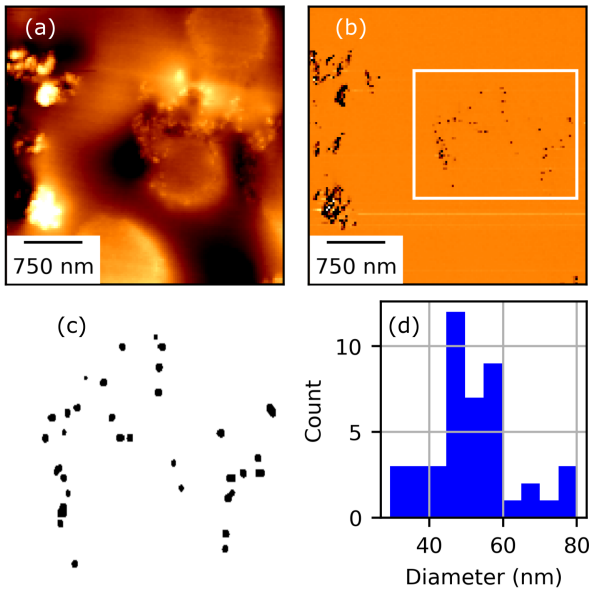

Figure 4.2: Size approximation of nanoparticles in sample A. (a) MFM height map of cross-sections of bacteria, with nanoparticles surrounding them. (b) MFM phase map of the same area, at 19 nm above the surface. (c) Cropped and filtered image of the phase map from with in the white box in b. (d) Histogram of nanoparticle diameter and the count. Of the 32 nanoparticles measured, the mean diameter is 50 ± 10 nm. The error used is the standard deviation in diameter size.

The location of nanoparticles with respect to the bacteria was further characterised, using MFM on several resin slices. Fig. 4.3 shows three slices of resin on sample A. White arrows indicate the edges of the slices, and the red arrow indicates the cantilever. The slices have been labelled 1, 2, and 3. Fig. 4.4 shows eight 20 μm^2 amplitude maps stitched together, recorded on slice 1. Fig. 4.5 shows eight similar-sized mappings of slice 2. Slice 3 mappings are not shown since imaging was not possible, likely due to a fold in the resin slice.

As seen in Figs. 4.4 and 4.5, similar features are visible. The most common features repeated in

both slice 1 and 2 come from bacteria which lie perpendicular to the mapped plane. These appear as circular cross-sections. The features coming from bacteria which lie parallel to the plane appear to be not often found repeated in both slice 1 and 2. An exception is the bacterium indicated by the blue arrows in Figs. 4.4 and 4.5. The blue arrow points to what appears to be the indentation of the bacterium in slice 1, and in slice 2, the majority of the bacterium appears to be visible.

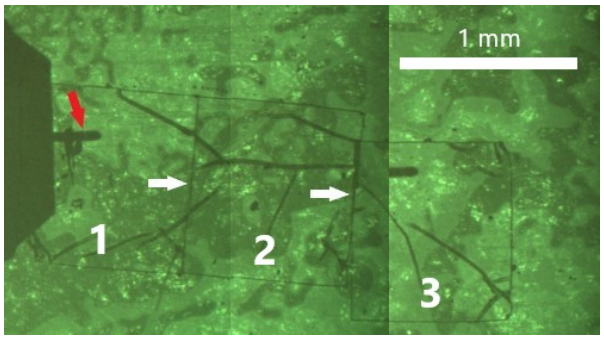

Figure 4.3: Optical image taken of three slices of resin on sample A. The image was stitched from a few sub-images, so contrast differences are visible. The red arrow is pointed at the probe cantilever, and the white arrows indicate the edges of the resin slices.

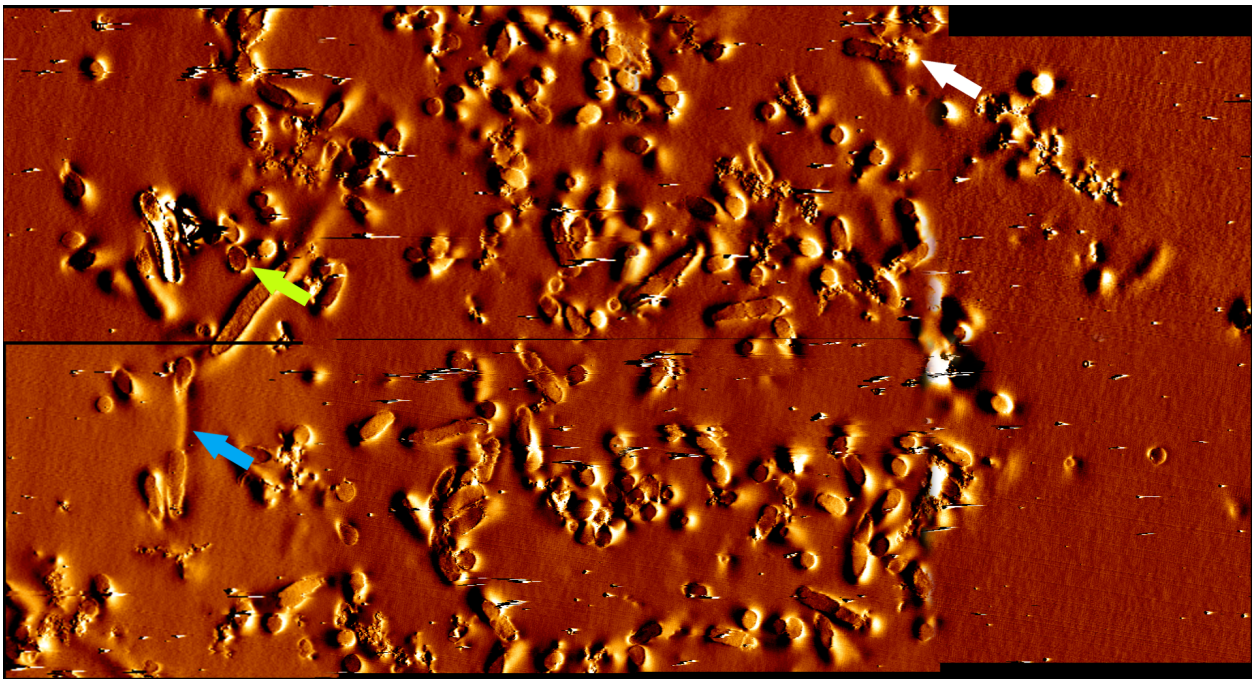

Figure 4.4: Stitched amplitude maps of several scans over a region of 80 μm by 40 μm. This is named slice 1.

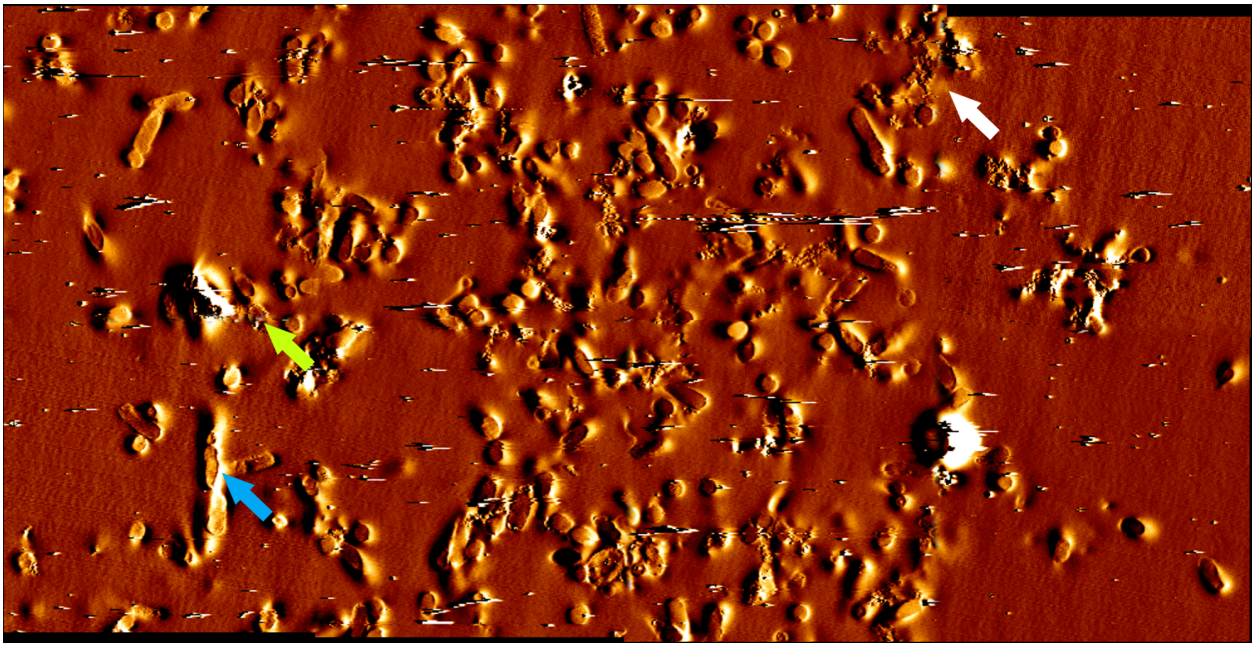

Figure 4.5: Stitched amplitude maps of several scans over a region of 80 μm by 40 μm. This is named slice 2.

Higher-resolution maps were performed to confirm further if the same place is imaged above both slices. Fig. 4.6 shows higher-resolution maps recorded at the white arrows in Figs. 4.4 and 4.5. The white arrows in Fig. 4.6 point towards four bacteria, at which in (a) all four bacteria cross-sections are visible. In Fig. 4.6b, the bottom two cross-section visible, whilst the upper two appear to be covered by resin and or nanoparticles. The blue arrow points towards a bacterium lying in the sample plane in Fig. 4.6a. In 4.6b, it appears this bacterium is also covered by resin and or nanoparticles. These images further demonstrate that the same position on multiple slices of resin sample can be found.

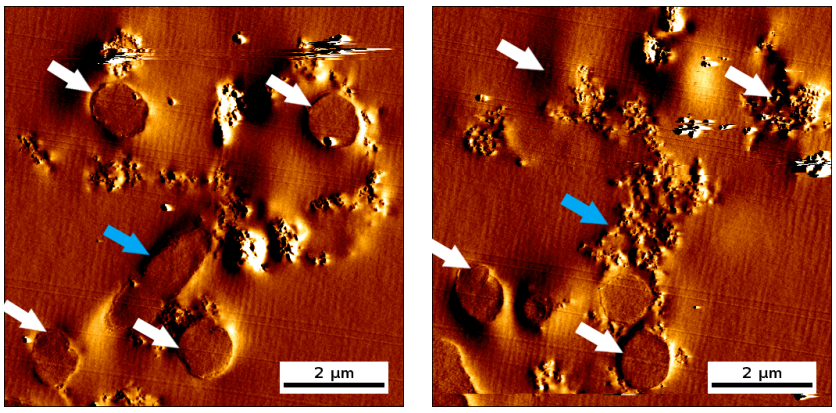

Figure 4.6: Higher resolution MFM amplitude maps of the region indicated by the white arrows in Figs. 4.4 and 4.5. (a) Amplitude map, imaged on slice 1. (b) Amplitude map, imaging on slice 2.

To study if the nanoparticles in sample A are located outside the bacteria cell membrane, inside the cell, within the cell membrane, or any combination of the above, higher-resolution imaging was done on a single bacterium. This was done using imaging on the bacterium indicated by the green arrow in Figs. 4.4 and 4.5. Fig. 4.7a-b shows height maps imaging on slice 1 and 2, respectively. The corresponding phase shift maps recorded at 19 nm above the surface are shown in Fig. 4.7c-d. The approximate area of nanoparticles found in the phase maps was analysed. In slice 1, the area of nanoparticles is approximately 30,000 nm^2, and in slice 2, 140,000 nm^2. No nanoparticles were excluded in the analysis, and therefore, includes the large clusters which are further (500 nm - 1 μm) from the cell walls.

Black lines are drawn in Fig. 4.7c-d, to indicate where the inner and outer cell membranes could be. It appears as though the nanoparticles could be located inside and outside the membranes and in between membranes. However, it could be that this is a misinterpretation. There are many places in the images where features appear to be repeated, as shown by the white arrows in Fig. 4.7b. This could be due to tip contamination, or the tip was damaged somehow during scanning. Therefore, it could be that what appears to be the cell membrane is the result of an artefact.

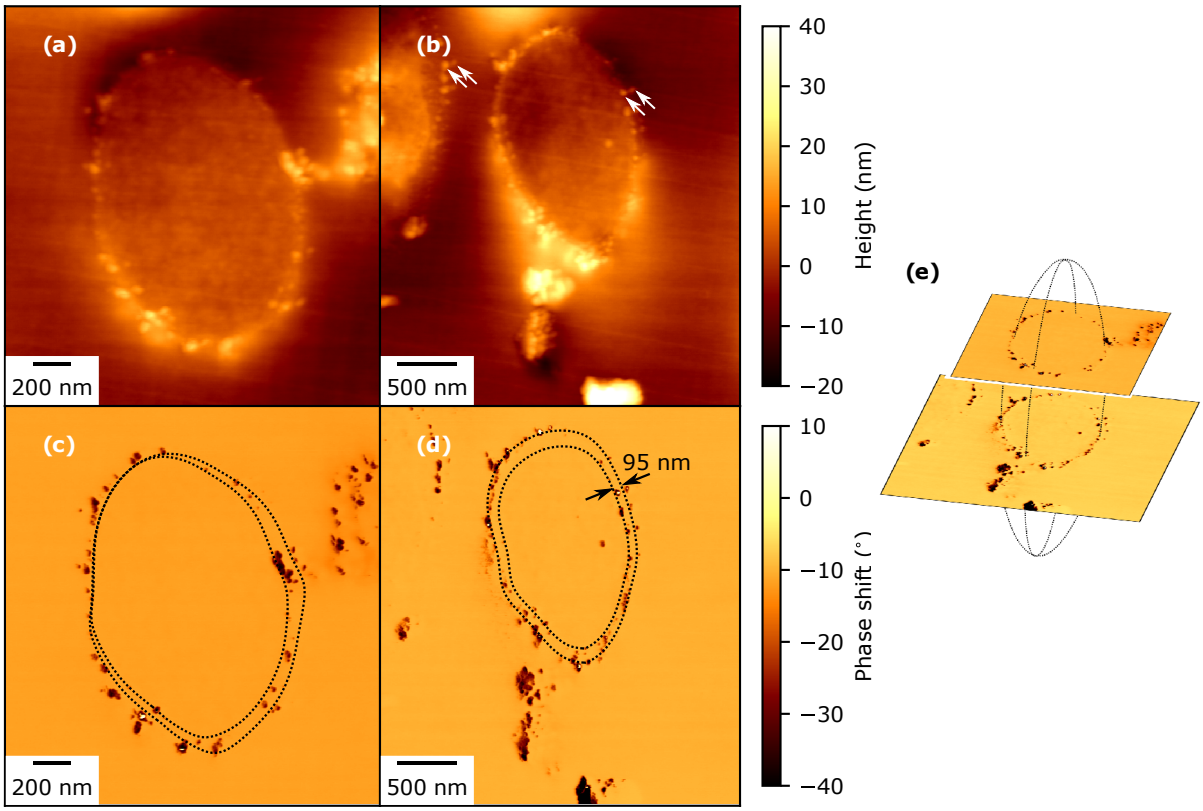

Figure 4.7: Higher resolution imaging of bacterium cross-section indicated by the green arrow in Fig. 4.5. (a) and (b) show height maps of slice 1 and slice 2, respectively. (c) and (d) show MFM phase maps recorded at 19 nm above the surface, again on slice 1 and 2, respectively. (e) Three-dimensional reconstruction of bacteria cross-sections.

4.2 Properties of samples specific to the application of MFM (sample A)

Specific to the application of MFM, measurements were performed to characterise how the material in the samples would behave in response to changes in the MFM parameters, such as the setpoint. Fig. 4.8a shows a height map of a bacterium cross-section, with nanoparticles surrounding it. Measurements were performed along line A using different setpoint values. The data was analysed by subtracting the same gradient from each line in python instead of a unique line done in other results in this study. Results show that along line A the measured MFM topography does not significantly change (Fig. 4.8b). It appears that the mean topography of the resin (black arrow) shows less deviation between measurements than the mean topography of the nanoparticles (blue arrow). However, this is within the error calculated.

Fig. 4.8c shows a height map of a different bacterium cross-section to Fig. 4.8a. Above two points, force spectroscopy was performed with various setpoint values (Fig. 4.8d, e). Force spectroscopy measures the deflection of the cantilever in the z direction. Increasing the setpoint appears to shift the curves to the left (Fig. 4.8d, e). Alternatively, in other words, increasing the setpoint results in the same level of phase shift, measured at a lower lift height from the surface.

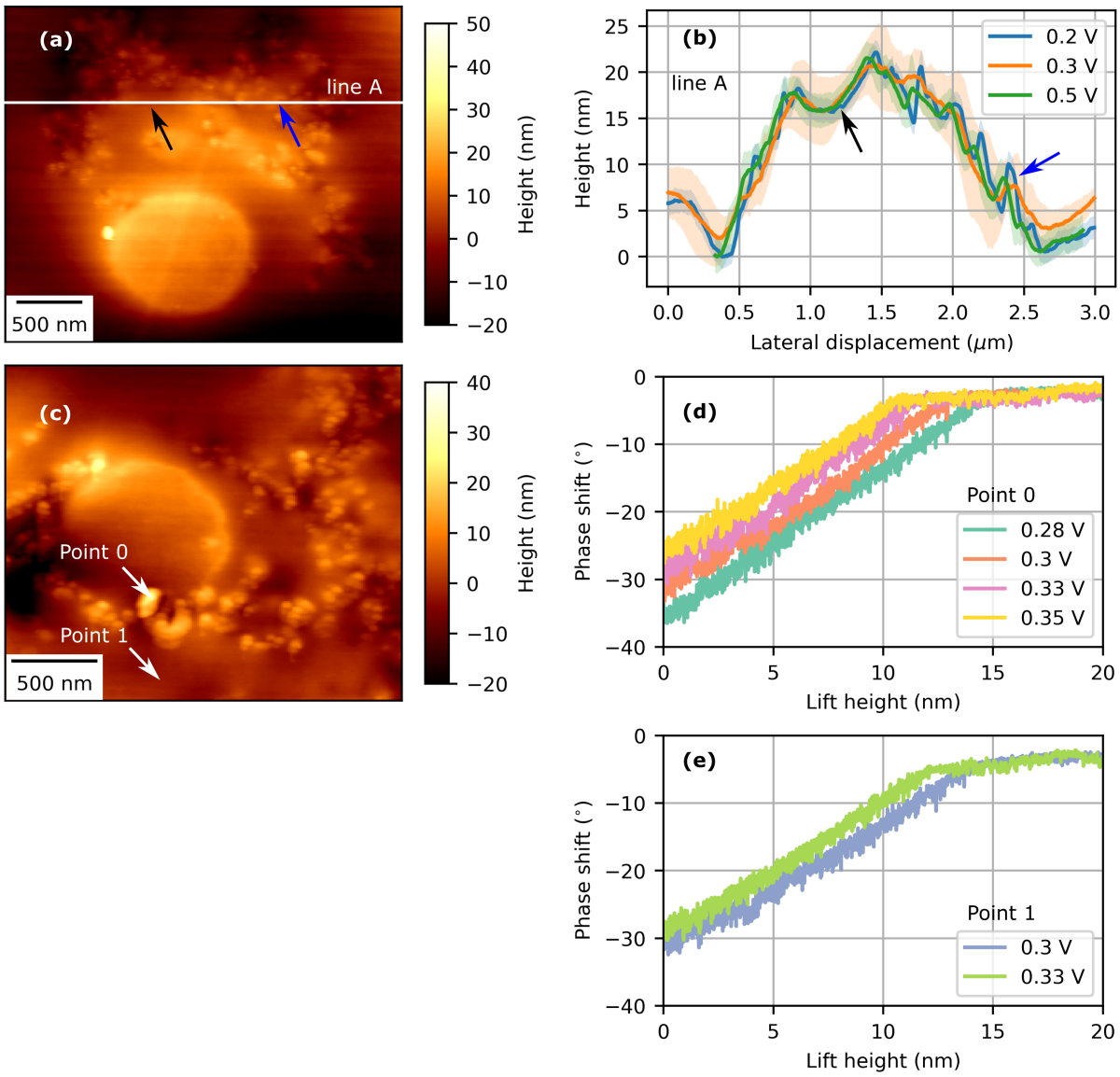

Figure 4.8: (a) Height map of a bacterium cross-section and nanoparticles surrounding it. (b) Height along line A as a function setpoint. Results show the mean and standard of 8 measurements. The standard deviation is shown using shadow. (c) Height map of different bacterium and nanoparticles. (d) Force spectroscopy above nanoparticle, as a function of setpoint. (e) Force spectroscopy above resin, as a function of setpoint.

4.3 Isolating magnetic interaction from short-range surface interaction and background interaction

4.3.1 Background interaction

Fig. 4.9 shows the results of scanning with a pseudo-demagnetised MFM tip and an AFM tip on sample A. Relative to the background signal, the MFM tip shows negligible interaction with the sample when scanning at 20 nm above the surface (Fig. 4.9b). The AFM measurements show that when scanning at 20 nm above the surface, the interaction with the sample is negligible (Fig. 4.9d). This suggests that there could be no electrostatic interaction.

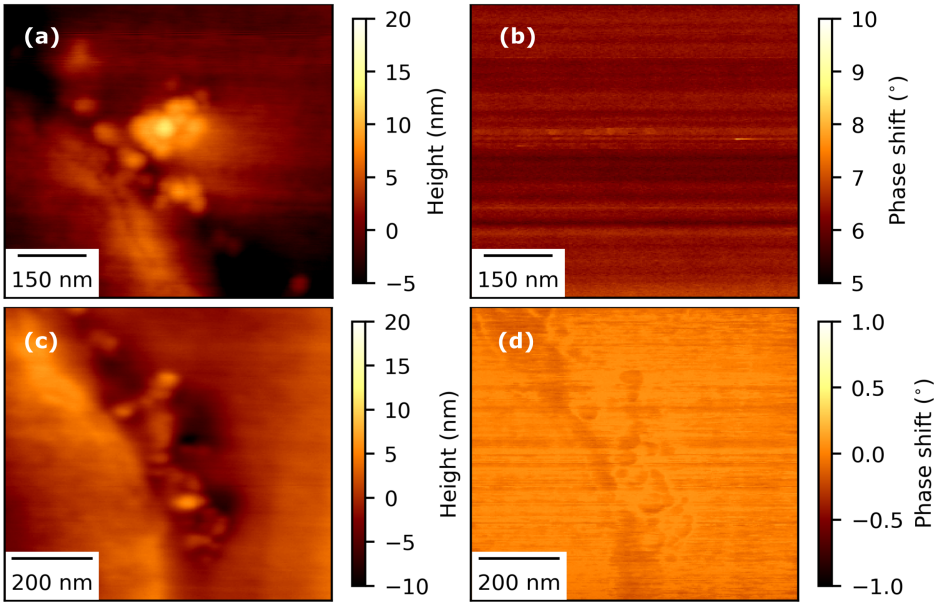

Figure 4.9: Imaging with a pseudo-demagnetised MFM tip and an AFM tip. (a) MFM height map, and (b) shows the corresponding MFM phase maps recorded at 20 nm above the surface. (c) AFM height map, and in (d) is the corresponding AFM phase map recorded at 20 nm above the surface.

4.3.2 Short-range surface interaction

To isolate the magnetic interaction from the short-range interaction, imaging was done in both AFM and MFM of the same area. Fig. 4.10a-l show phase shift maps at 0, 5, 10, 15, 20, 22, 24, 27, 30, 40, 70, and 100 nm above the surface of sample A. The imaged area contains a bacterium near the top of the image and clusters of nanoparticles surrounding it. The bacterium cross-section near the top has a length and width of approximately 1.8 μm and 1 μm, respectively (Fig. 4.10b). The tip-sample interaction above the nanoparticles shows large negative phase shifts. The outline

of the bacterium wall is visible in the phase shift maps also, which could be due to nanoparticles surrounding the cell wall. Fig. 4.10m-p shows zoomed views of the nanoparticle indicated by the blue arrows in Fig. 4.10a-l. This nanoparticle has a diameter of 200 nm, approximated from the phase map.

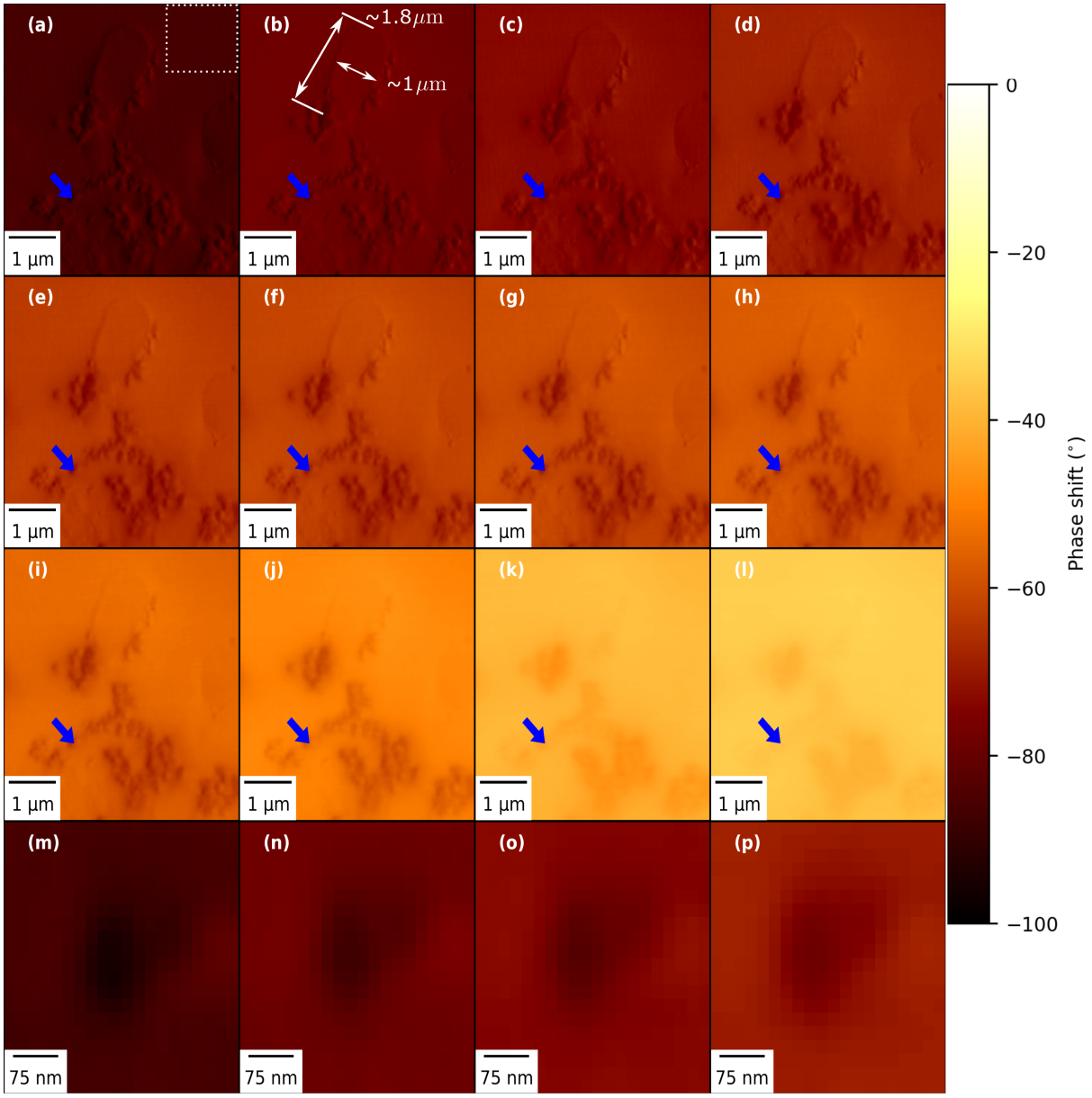

Figure 4.10: MFM phase maps of cross-sections of bacteria with Pd-Fe nanoparticles surrounding them. In (a)-(l), the phase maps are recorded at heights 0, 5, 10, 15, 20, 22, 24, 27, 30, 40, 70, and 100 nm above the surface. In (m)-(p), MFM phase maps are shown zoomed in on area indicated by the blue arrow. These are recorded at (m) 0 nm, (n) 5 nm, (o) 10 nm, and (p) 15 nm above the sample surface. The dashed box in (a), indicates the region used to calculate the background.

The same area was imaged in AFM at 0, 5, 10, and 15 nm above the surface (Fig. 4.11). Measurements were taken at bigger heights than 15 nm from the surface in AFM; however, they are not shown, as the maps show little contrast. The AFM and MFM phase shift maps are plotted

with different scale bars to increase the visibility of the contrast. Fig. 4.11e-h shows images of the same nanoparticle as in Fig. 4.10m-p.

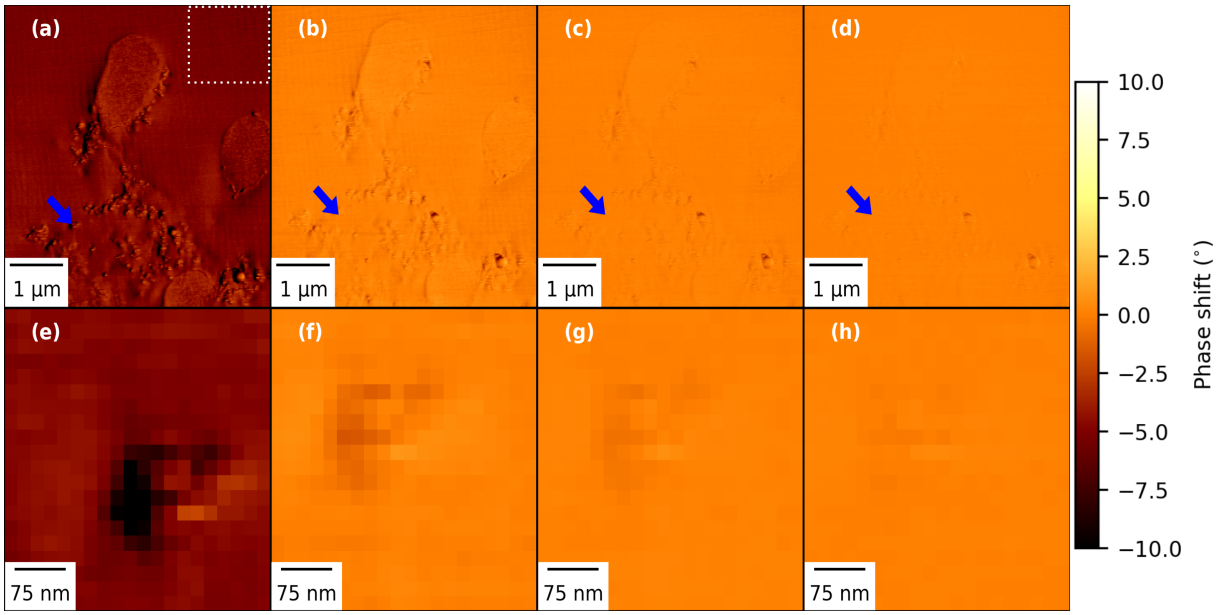

Figure 4.11: AFM phase maps, corresponding to the same area in Fig. 4.10. The phase maps are recorded at (a) 0 nm, (b) 5 nm, (c) 10 nm, and (d) 15 nm above the sample surface. (e)-(h) are closer views of the nanoparticles indicated by the blue arrow. The phase maps in (e)-(h) are recorded at the same heights as in (a)-(d), respectively. The dashed box in (a), indicates the region used to calculate the background.

The MFM and AFM background phase shift at each height is shown in Fig. 4.12a. In MFM, the tip interaction with the MFM magnet can contribute to the background signal. The method for subtracting this background is discussed in the methods section. Fig. 4.12a shows that the background signal is large negative in MFM and increases towards zero, with increasing lift height from the surface. However, even at 300 nm, the phase shift has not levelled off yet and could increase further. The AFM background is almost negligible, except at 0 nm above the surface.

Fig. 4.12b shows the MFM and AFM phase shift above the selected nanoparticle after the background is subtracted. The MFM phase shift is larger negative than AFM at all heights. The AFM phase shift is approximately -3 ° just above the surface and decays to 0 ° at approximately 20 nm above the surface. The error bars in AFM are plotted in the figure. However, they are almost negligible or hidden behind symbols. On the other hand, the MFM phase shift is much

larger negative and decays less rapidly than in AFM. The MFM negative peak is not at 0 nm, like in AFM, but a little higher above the surface (20 - 25 nm). However, this could be due to the error, which is significant at this height.

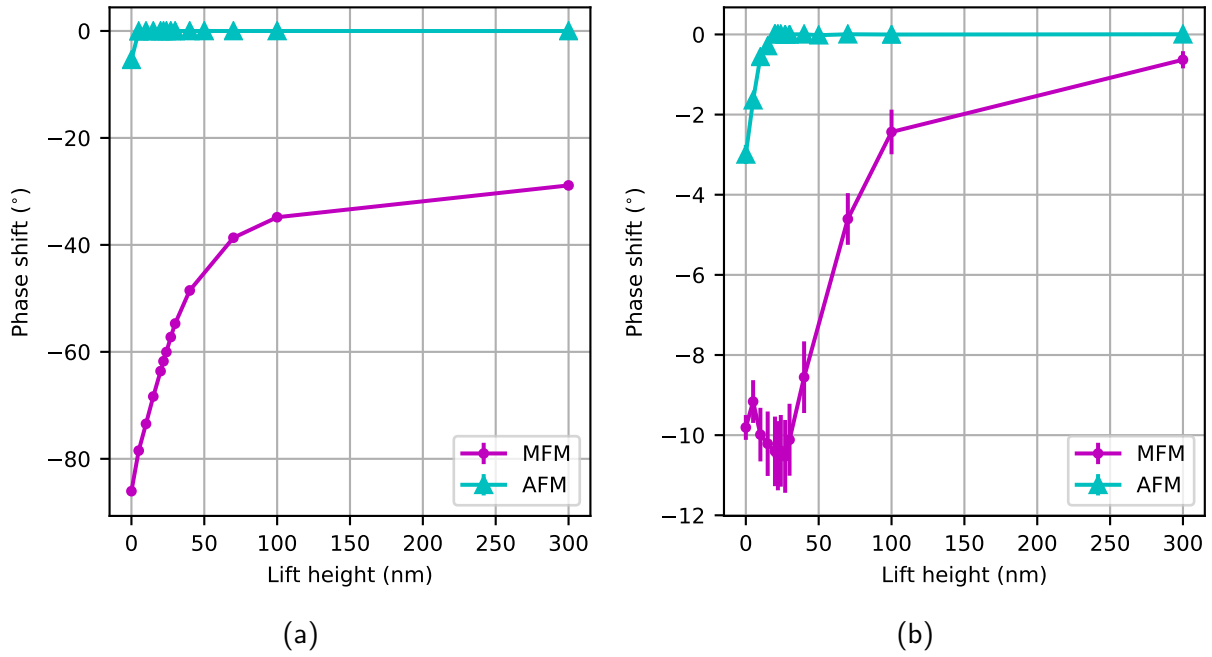

Figure 4.12: (a) MFM and AFM background phase shift. (b) MFM and AFM phase shift above the nanoparticle in Figs. 4.10 and 4.11, after subtracting the background.

4.3.3 Force spectroscopy

Force spectroscopy was also performed at several points to investigate the deflection above nanoparticles, which are close to each other, as a function of lift height. Fig. 4.13a-b shows height maps with the force spectroscopy points indicated, in MFM and AFM, respectively. To study the deflection above these points in both MFM and AFM, care was taken to locate the same points. Fig. 4.13c shows the MFM phase shift decays gradually with increasing height from the surface, which begins to flatten after 400 nm. However, it is possible that the curves would continue to flatten off at a bigger height. This information, however, was not recorded. Points 7-10 are assumed not to be above magnetic material, whilst we assume points 0-6 are. Some points are so close to a nanoparticle, like point 5, that it is labelled as magnetic. Above points 7-10 (non-magnetic), less negative phase shift is measured, compared to that above points 0-6 (magnetic) (Fig. 4.13c). However, very close to the surface (0-5 nm), the phase shift appears to be almost uniform between points

before diverging at greater heights. This could be due to (i) stronger surface forces at low heights than magnetic forces or (ii) the effects of roughness on the nanoscale. Points 0 and 9 are the two closest magnetic and non-magnetic points in lateral distance (150 nm) from each other. As seen in Fig. 4.13c, at approximately 150 nm above the surface, all the measurements (above magnetic and non-magnetic points) appear to converge together. It could be that where the distance above the surface is similar to the lateral distance between points, the measured phase shift is nearly the same above the points.

Fig. 4.13d shows the force spectroscopy points measured with an AFM probe. The AFM phase shift decays much more rapidly compared to measurements with the MFM tip. However, different setpoints were used for the MFM (0.4 V) and AFM (0.3 V) force spectroscopy, which could affect results. The phase shift flattens out above approximately 12 nm, for all points (Fig. 4.13d). The phase shift above points 7-10 (non-magnetic) does not clearly distinguish from the phase shift above points 0-6. This is expected since the tip-sample interaction is assumed to be non-magnetic, with an AFM tip. Note that some of the measurements above the magnetic points are hidden beneath the non-magnetic measurements (Fig. 4.13d inset). Although there is no clear distinction between measurements above magnetic and non-magnetic points, the measurements deviate from each other. This deviation could be due to the surface roughness on the nanoscale.

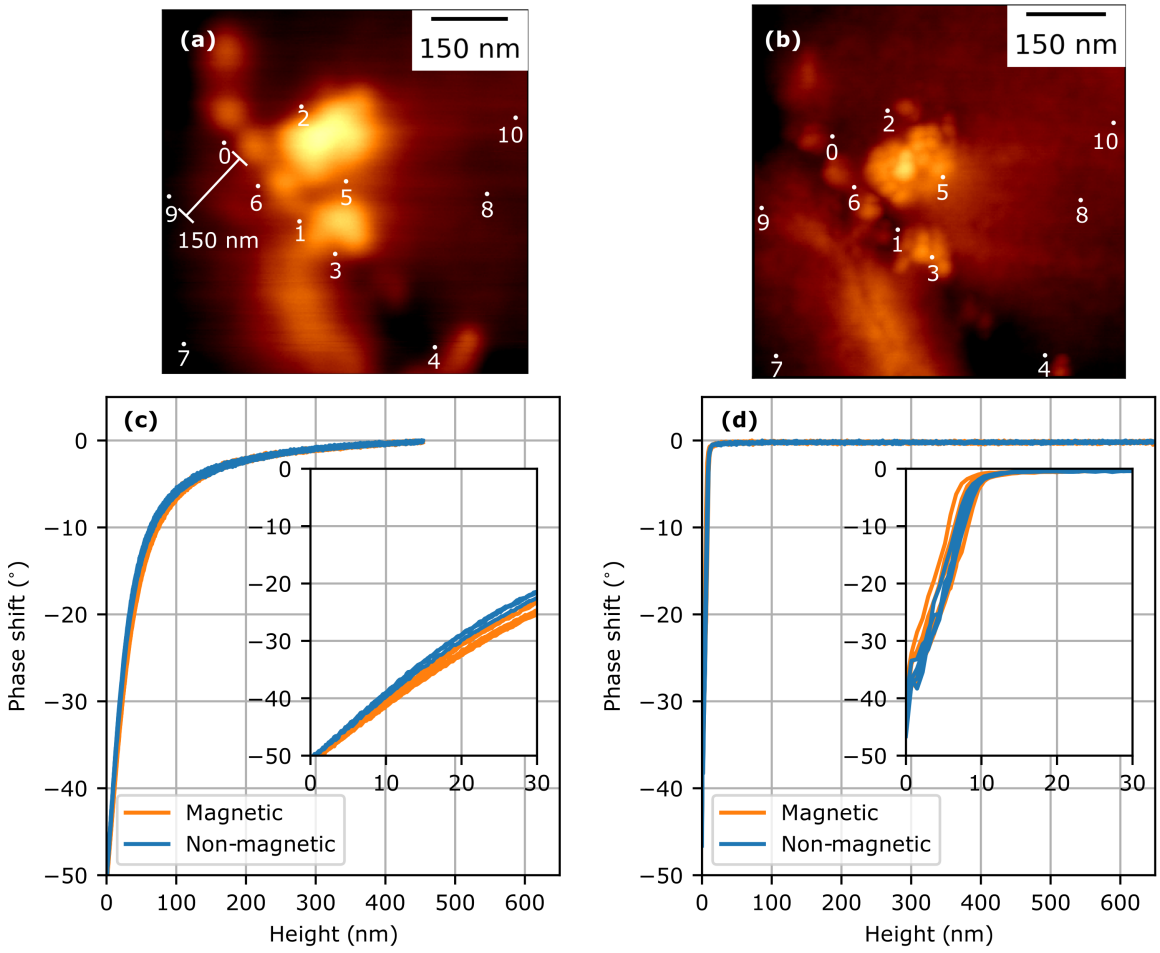

Figure 4.13: Force spectroscopy. (a) and (b) show height maps in MFM and AFM, respectively, with the force spectroscopy points indicated. (c) MFM force spectroscopy curves. (d) AFM force spectroscopy curves. In MFM, the setpoint used was 0.4 V, and 0.3 V in AFM. The calculated error (± 0.2 °) is not plotted in the figure.

4.3.4 Comparing magnetic signals from Pd-Fe and Pd nanoparticles (samples A and B)

To compare the magnetic signal above samples A and B, measurements were performed at several heights above sample B. Fig. 4.14a-d, shows phase shift maps at 3, 6, 9, and 12 nm above the surface of a cross-section of a bacterium on sample B. Measurements were done at bigger heights, but are not shown. This bacterium has a length and width of approximately 1 μm and 0.7 μm, respectively. Fig. 4.14e-h, shows zoomed-in views of the area indicated by the blue arrows in Fig. 4.14a-d, respectively. The resolution of the image does not appear to be high enough to

resolve where the nanoparticles are. Fig. 4.14i shows the background phase shift as a function of height from the surface. The background phase shift starts at -50 ° and levels off at approximately -5 °. This is different to the background measured above sample A, where the phase shift is approximately -90 ° at 0 nm above the surface and decays more slowly to approximately -30 ° at 300 nm above the surface. This difference could be due to the different thicknesses of the samples, and therefore, different distance from the MFM magnet. The phase shift above the selected point, after the background is subtracted, does not appear to decay monotonically (Fig. 4.14j). This could be, however, explained by the error.

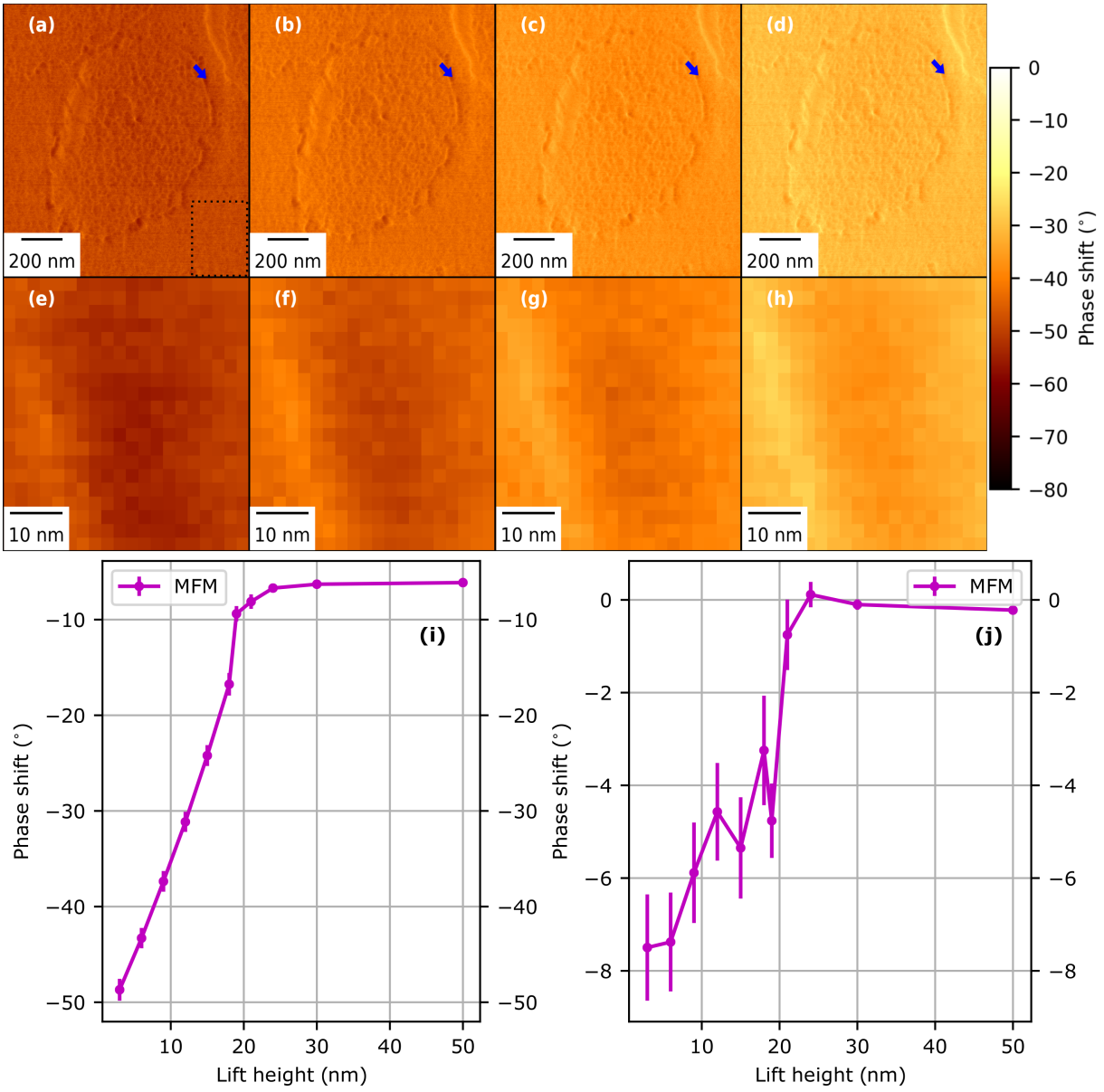

Figure 4.14: MFM phase shift maps of a cross-section of a bacterium in sample B. Phase shift maps are recorded at (a) 3 nm, (b) 6 nm, (c) 9 nm, (d) 12 nm above the surface. (e)-(h) show MFM phase shift maps zoomed in on the region indicated by the blue arrow. The heights, at which (e)-(h) are recorded are the same as in (a)-(d), respectively. (i) MFM background phase shift. (j) MFM phase shift as a function of height after subtracting the background. The dashed box in (a), indicates the region used to calculate the background.

Fig. 4.15a, b shows the phase shift measured above several points in both samples A and B, respectively, after the subtraction of the background. The AFM phase shift above sample B was

not measured. It is hypothesised to be similar to the AFM phase shift above sample A, but this was not studied. The MFM phase shift above sample A is larger negative in general than both the AFM phase shift and the MFM phase shift above sample B. The MFM phase shift above sample B appears to be greater negative than the AFM phase shift above sample A. However, at some heights (approximately 25 nm), the MFM phase shift above sample B appears positive and greater than the AFM phase shift. The positive phase shift could be due to the error.

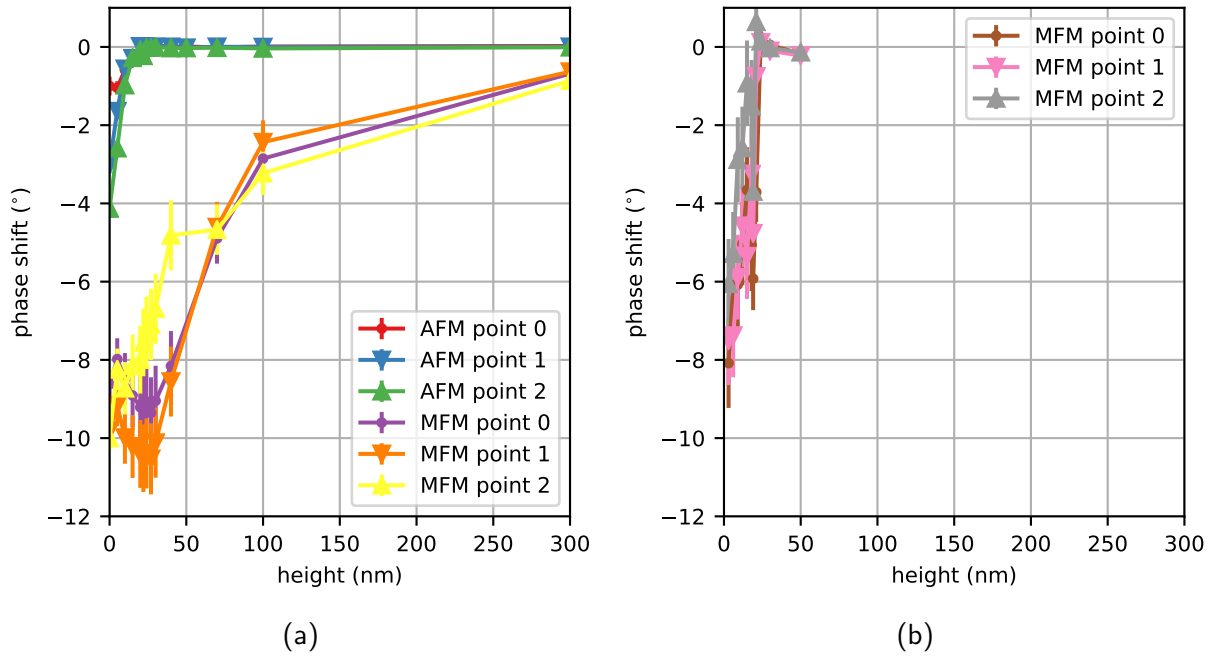

Figure 4.15: (a) MFM and AFM phase shift in sample A, above several nanoparticles. (b) MFM phase shift in sample B, above several points.

4.4 Comparison of MFM and AFM probes

4.4.1 Apparent size of nanoparticles and bacteria (Samples A and C)

Measurements were performed above samples A and C to compare the properties of the AFM and MFM probes. In Fig. 4.16a-b, are two cross-sections of bacteria on sample A with clusters of nanoparticles attached to them, imaged in MFM and AFM. Higher resolution images of the region in the white boxes shows that the topographic features in MFM are less distinguished compared to the features imaged in AFM (Fig. 4.16c, d). The topography of the nanoparticles appears more defined in AFM compared to MFM, which is consistent with the tip geometry (see Table 2).

The topography along lines A and B is shown in Fig. 4.16e. Line B has been shifted laterally

and vertically, so that the largest peaks in lines A and B are aligned. Again, the AFM measurements appear to be more detailed. For example, the MFM tip was not able to resolve the small peak recorded in AFM (see red arrow), from the two peaks on the left side (see green arrows). There is a height difference d, between the two lines, which could be (i) due to the different signal subtracted from the height maps in Fig. 4.16c-d, or (ii), due to the different tip properties. Data analysis was repeated by removing identical signals from the data, suggesting that d could originate from different tip properties (Appendix Fig. A.1). Roughness measurements along the lines show that the MFM topography is rougher than the AFM topography (see Table 3).

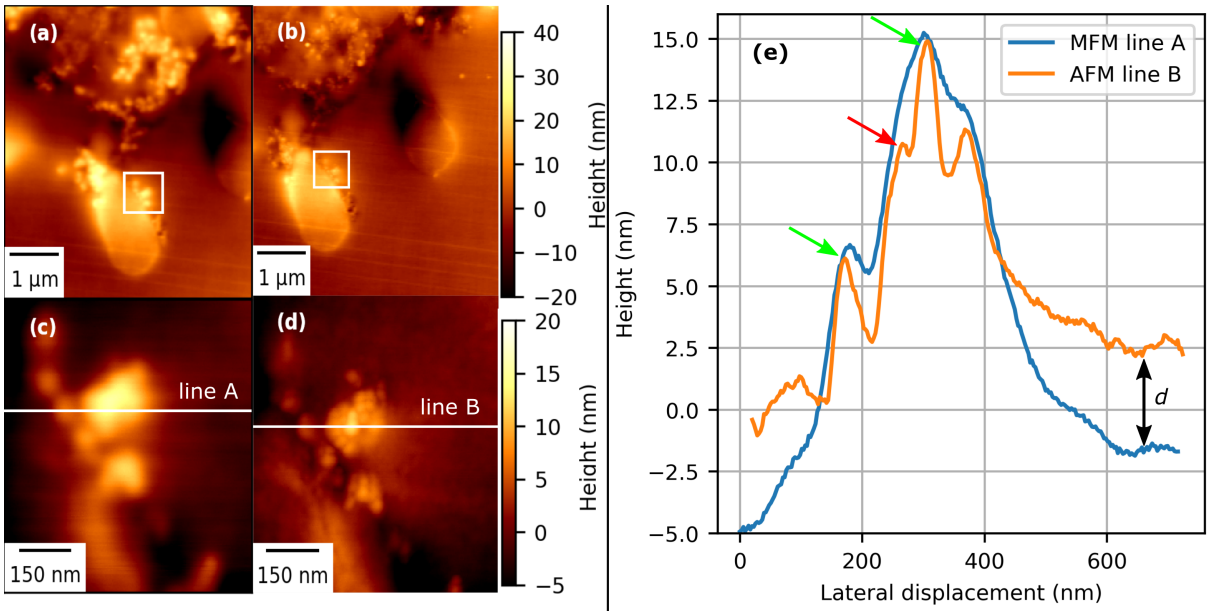

Figure 4.16: Comparison of AFM and MFM images. (a) MFM height map (b) AFM height map. (c) and (d) are higher resolution imaging within in white boxes in (a) and (b), respectively. (e) MFM and AFM topography along lines A and B.

Table 3: Roughness along the lines A and B in Fig. 4.16. Results show the mean and range of three repeated measurements along similar lines.

	AFM	MFM
Line length (nm)	704	716
Average Roughness Ra (nm)	3.0 ± 0.2	5.3 ± 0.1
RMS Roughness Rq (nm)	3.6 ± 0.2	6.1 ± 0.1
Peak-to-valley Roughness (nm)	15.2 ± 0.1	20.3 ± 0.4

Measurements were also done on sample C without the MFM magnet, to compare the topography measured and the phase shift above the surface, using an MFM and AFM probe. Fig. 4.17a-b show height maps centred on a single bacterium, imaged in both MFM and AFM, respectively. It is not clear from these height maps, whether there are nanoparticles attached to the bacterium. In contrast to Fig. 4.16, the measurements along lines A and B show that topography is reproduced quite well on the micron scale by the two probes (Fig. 4.17c).

The corresponding phase shift to lines A and B, is measured at 20 nm above the surface (Fig. 4.17d). Although the phase shift measurements are similar in profile, they are offset from each other by a constant value of approximately 10-12 °. The MFM phase shift has a larger negative value than the AFM phase shift.

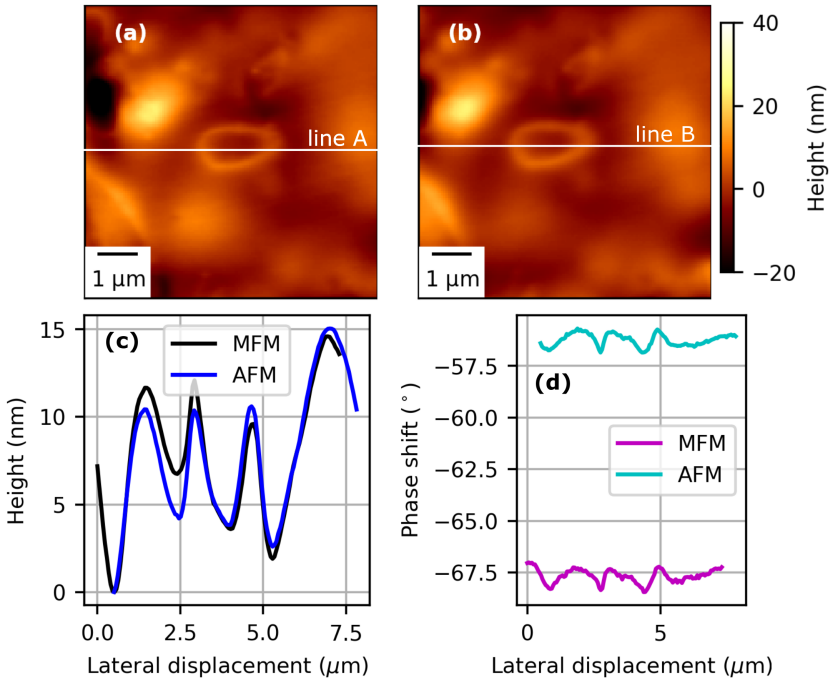

Figure 4.17: Comparison of topography and phase shift in MFM and AFM, above sample C without the MFM magnet. (a) MFM height map. (b) AFM height map. (c) MFM and AFM topography along the lines A and B. (d) corresponding MFM and AFM phase shift, along lines A and B, at 20 nm above the suface.

4.4.2 Force spectroscopy (Sample C)

To further investigate the behaviour of the phase shift above sample C without the MFM magnet, force spectroscopy was performed. Unfortunately, the force spectroscopy points were not performed

in the same positions by AFM and MFM (Fig. 4.18a, b). The measured phase shift is large negative in value far above the sample surface, above even $\geq$ 20 nm (Fig. 4.18c). In addition, the phase shift differs slightly between points, with increasing lift height. This could be due to the nanoscale topography, although it is higher above the surface than in previous measurements (Fig. 4.13d). The same behaviour appears to be in the AFM scans. Force spectroscopy measurements were repeated three times at each point, and the error calculated was $\pm$ 0.2 $^\circ$ using the standard deviation of the measurements. Consistent with results in Fig. 4.17, the MFM and AFM measurements are offset from each other, and here, the phase shift difference changes with height. At big distances above the surface, the interaction appears to flatten off (Fig. 4.18d).

These findings are important, as this could show that the AFM and MFM measurements can not be compared to each other.

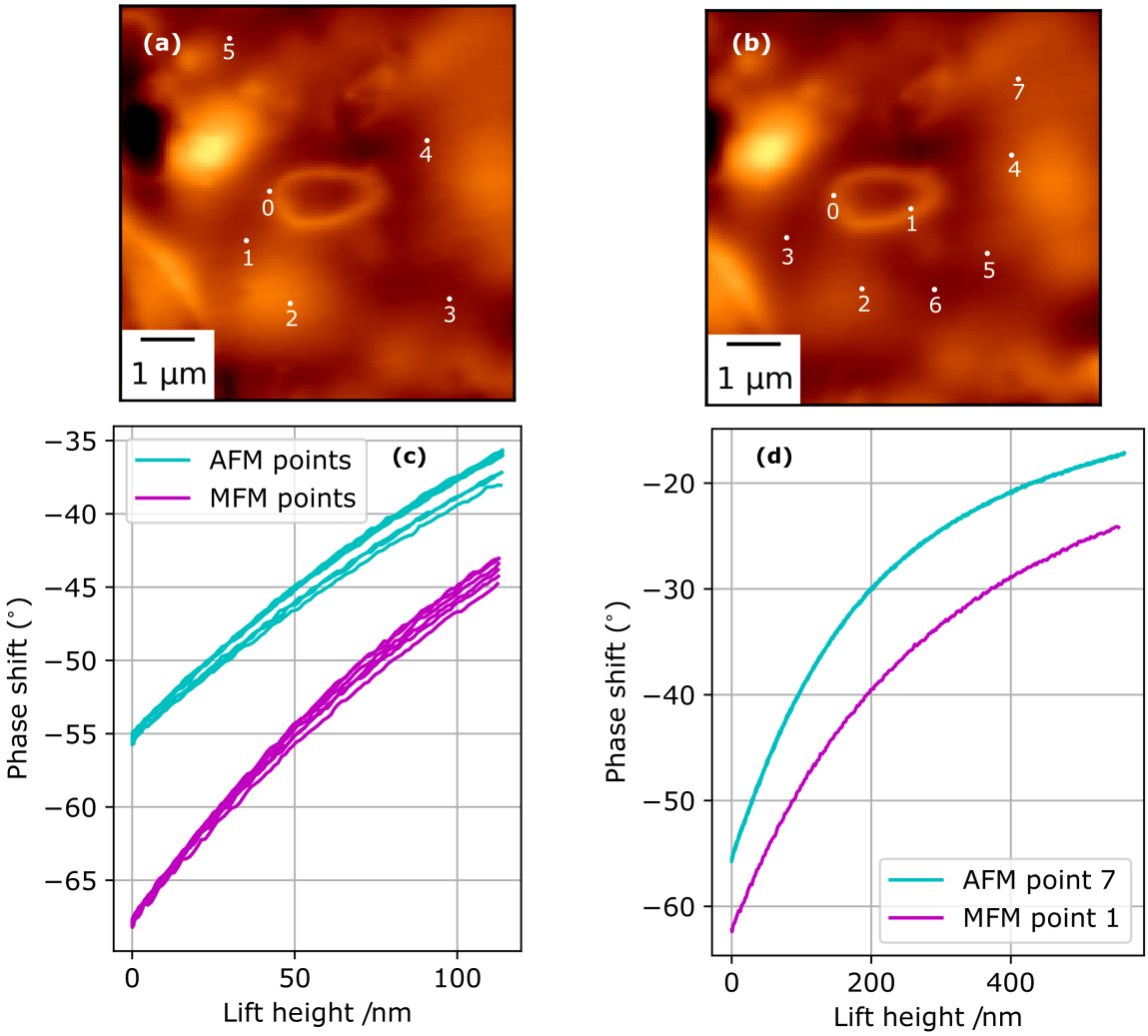

Figure 4.18: (a) MFM height map showing force spectroscopy points. (b) AFM height map showing force spectroscopy points. (c) MFM and AFM force spectroscopy curves. (d) Long distance force spectroscopy in AFM and MFM. The error (± 0.2 °) is not visible in the figure.

4.5 MFM artefacts and interpreting the signals

4.5.1 Micrometre resolution imaging

To study the behaviour of the MFM tip-sample interaction above nanoparticles, imaging was done at different scanning angles above the surface. Fig. 4.19a-d show height maps of nanoparticles, recorded at various scanning angles above sample A. Fig. 4.19e-h show the corresponding phase shift maps, measured at 19 nm above the surface. Dark and light contrast appears on opposite sides of the nanoparticles with respect to the cantilever scan direction (see the nanoparticle indicated by

blue arrows). Similar results are found in amplitude maps measured at 19 nm above the surface (appendix B). The contrast in height, however, remains the same, independent of the scanning direction.

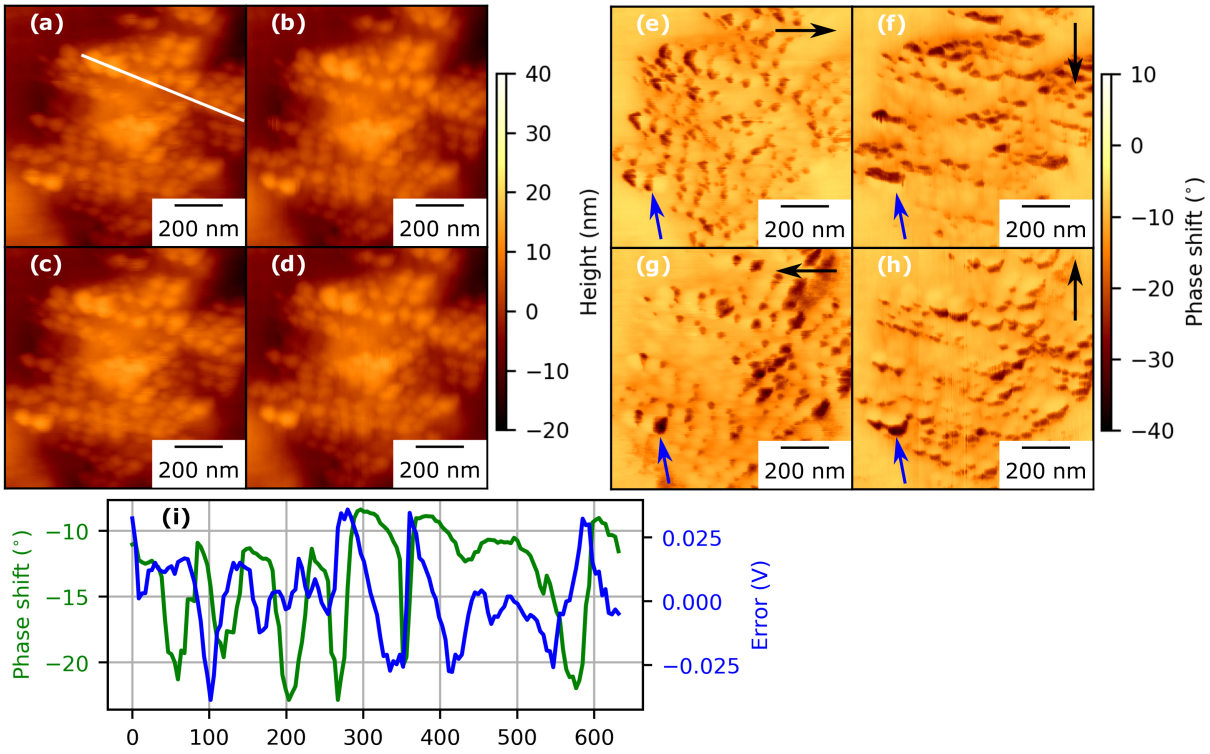

Figure 4.19: MFM height maps (a)-(d) and phase maps (e)-(h), measured at four scanning angles, at 19 nm above the surface. The scan angles are: (a) 90 °, (b) 0 °, (c) 180 °, and (d) -90 °, and the same for (e)-(h), respectively. The black arrows in the phase shift maps indicate the direction of the cantilever scanning. (i) Phase shift and error signal along white line in (a).

To evaluate if this dark and light contrast on opposite sides, could originate from the feedback loop, the error signal is analysed (Fig. 4.19i). The white line through several nanoparticles is drawn to indicate where the measurements are analysed (Fig. 4.19a). It appears that the error does not peak exactly in the positions where the phase shift peaks (Fig. 4.19i). The maximum absolute error is 0.039 V. Compared to the setpoint (0.3 V), this error is 13 % of the setpoint.

4.5.2 Nanometre resolution imaging

Similar experiments were performed at higher resolution, on the same slice of resin in sample A. Fig. 4.20, shows height and phase shift maps of a nanoparticle in the centre, which is approximately

100 nm in width and length. The phase shift does not appear to show the same dark and light contrast on opposite sides as in Fig. 4.19. Here, the phase shift is relatively uniform across the nanoparticle, although there are some places where the interaction appears to vary, as indicated by the blue arrows. Measurements were also done at 22 nm above the surface (appendix B), where interaction shows less negative phase shift, but also fairly uniform contrast. The error signal maps (appendix B) show that the error from the feedback loop is not greater than 1 mV, which is 0.3 % of the setpoint.

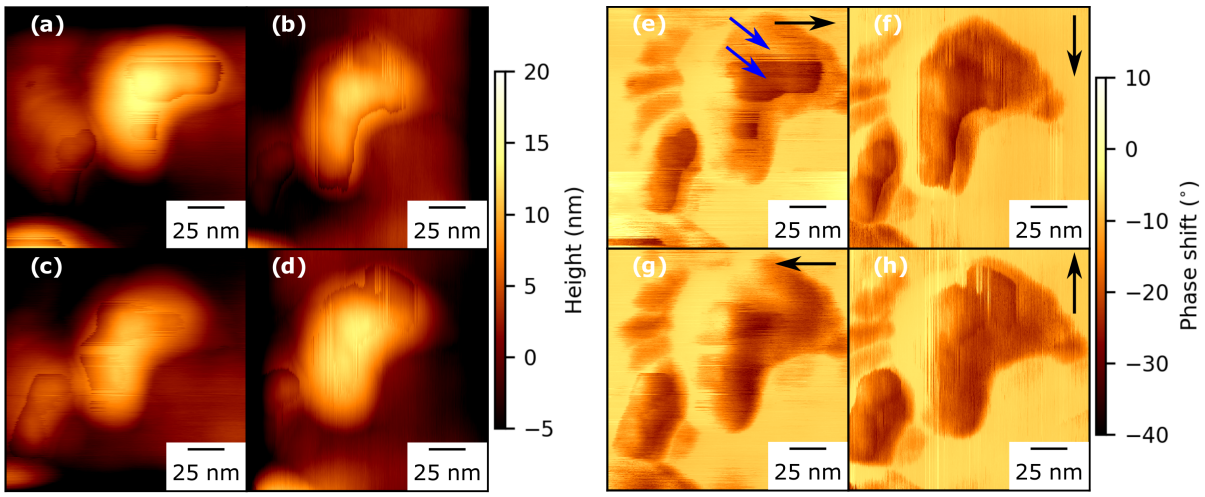

Figure 4.20: MFM height maps (a)-(d) and phase maps (e)-(h), at four scanning angle. The scan angles are: (a) 90 °, (b) 0 °,(c) 180 °, and (d) -90, and the same angles in (e)-(h), respectively. The phase maps are recorded at 20 nm above the surface of sample A. The black arrows in the phase shift maps indicate the direction of the cantilever scanning.

4.5.3 Nanometre resolution imaging 2

This experiment was again repeated at high resolution to investigate another nanoparticle, on the same slice of resin. Fig. 4.21a-b shows a group of nanoparticles in sample A, in both height and phase shift, respectively. The nanoparticle in the white box is approximately 67 nm in width and 70 nm in length. However, it appears in the phase shift map that this could be an agglomerate of several nanoparticles (Fig. 4.21b). The nanoparticles were imaged in four different directions to record the phase map at these angles (Fig. 4.21c-f). Dark contrast appears predominantly on one side of the nanoparticles, independent of the scanning direction. It also appears, that there is bright contrast in between dark contrast, as indicated by the blue arrows (Fig. 4.21e).

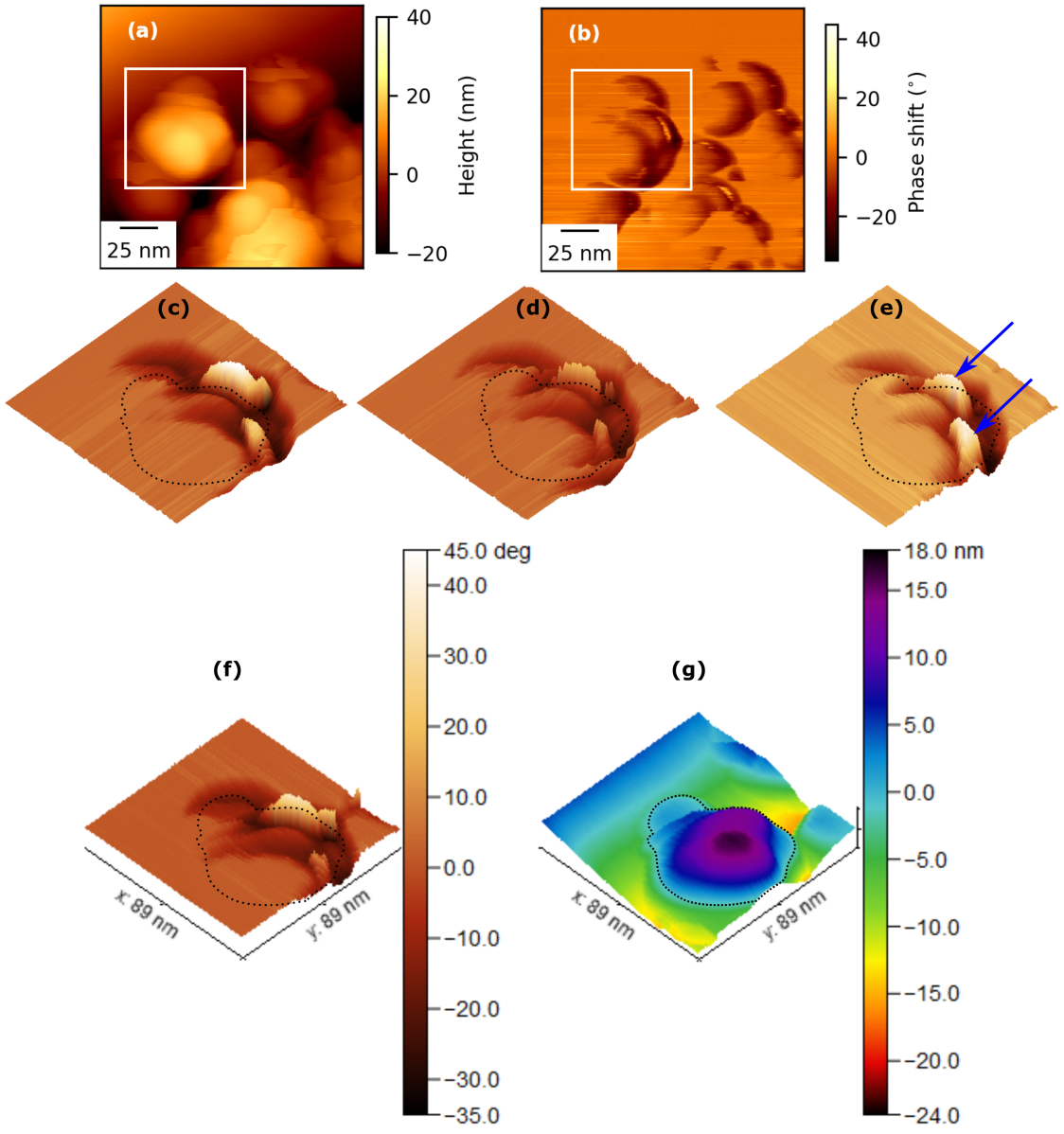

Figure 4.21: High resolution MFM images of nanoparticles at different scan angles, above sample A. (a) Height map. (b) Phase shift map. (c)-(f) Phase shift maps were recorded in the white box in b, in which the scan angles are: (c) 0 °, (d) 180 °,(e) 90 °, and (f) -90. All phase maps are recorded at 20 nm above the surface. Dashed lines are drawn to indicate a height contour around the nanoparticles. (g) Height map, imaged in the white box in a. Images are shown in 3D to better visualise the contrast.

5 Discussion

5.1 Size and location of nanoparticles

Since the nanoparticles and bacteria were found to be partially embedded in resin (Fig. 4.1), it was found challenging to use the topography to estimate the nanoparticle size since it was not clear how to distinguish between the resin and the nanoparticle (Fig. 4.1d). In addition, contrary to the suggested practice [18,67] of avoiding the tip-sample convolution (Fig. 2.12), it was not possible to measure the height of the nanoparticles since they are partially embedded.

Instead, the size estimation was done using a phase map recorded at 19 nm above the surface. The average nanoparticle diameter was calculated to be 50 $\pm$ 10 nm. Often, bacteria were surrounded by large agglomerates of nanoparticles, like on the left-hand side of Fig. 4.2b. Therefore, it was challenging to find a "good" area to perform measurements. On the one hand, using MFM could be appropriate for this task, since research done [6] suggests that the nanoparticles have a magnetic surface and non-magnetic core, which would enable MFM to observe magnetically, the "true" size. On the other hand, perhaps using another approach like TEM would be more beneficial since it does not have this limitation. Also, MFM is limited since the tip geometry can contribute to measurements (Fig. 2.12). TEM, however, cannot distinguish between non-magnetic and magnetic nanoparticles.

To further analyse the location of the nanoparticles with respect to the bacteria, imaging across several slices was done. It was not apparent beforehand that this experiment was possible. Since the resin slices are approximately half the length of a bacterium, it could have been that none of the bacteria cross-sections was repeated in consecutive slices. However, the results show that it is possible to map the same bacterium in two sequential slices of 0.5 μm thick resin slices. This sequential imaging could be done in more slices if they are still intact. This method could be advantageous for localising nanoparticles, determining whether they are located inside the bacteria cell or in the membrane. The results shown here, do not have sufficient resolution and quality to distinguish if the nanoparticles are within the cell membrane or inside the cell. An artefact was found in the images, and therefore, suggests that what was imaged was not nanoparticles in the cell membranes (Fig. 4.7). The results do show, however, that most nanoparticles are found outside the cell wall.

It is possible, however, to perform such measurements to get conclusive results. These measure-

ments would be an exciting avenue of future investigation. If a new tip is used and with slightly higher resolution imaging on the membrane, this would be possible.

In addition to this, imaging several slices of resin could be used to study if there are regions of the bacteria with more or fewer nanoparticles. For example, if more nanoparticles are localised at the poles of the bacteria. This information could be essential in tuning parameters for nanoparticle production. The total area of the nanoparticles in each image of the slices (Fig. 4.7) was also calculated. This calculation could be refined to measure the number of nanoparticles at a certain distance from the cell membrane, allowing for quantifying the number of nanoparticles that the bacteria produce in specific regions and giving feedback for the production process.

5.2 Properties of samples specific to the application of MFM

AFM topography has been demonstrated to be sensitive to variation in the setpoint amplitude [42]. Results on sample A show that the MFM topographies do not deviate from each other by more than 2 - 6 nm when varying the setpoint between 0.2 and 0.5 V (Fig. 4.8). This information suggests that changes to the force applied by the tip do not significantly deform the sample surface. At least, it is not significant compared to the error in the measurements. In [42], it is shown that the peak force is greater when tapping harder surfaces. However, the average force over one oscillation is the same. This information suggests the hardness should not affect results. The topographies in Fig. 4.8 do appear to deviate from each other more where there are nanoparticles, compared to scanning above resin, but this is within the error. Hence this distinction cannot be made.

The phase shift, however, does show significant changes. Since the setpoint is inversely proportional to the force [42], as the force applied by the tip increases, the measured phase shift becomes more negative (Eq. 2). The phase shift between measurements is significant compared to the error calculated in other results (Fig. 4.12). For example, at 5 nm above the surface the measured phase shift between setpoint 0.28 V and 0.35 V is 9 ± 1 ° (Fig. 4.8), using the error from Fig. 4.12. This result suggests that increasing the force applied by the tip reduces the height necessary to measure tip-sample forces. In addition, these force spectroscopy results show that the measurements are not susceptible to instabilities, as was discussed in theory (section 2.2.5), since the phase shift decreases monotonically.

These results also show that the MFM method is appropriate for the task of studying these samples. As was shown in theory, the AFM is sensitive to cantilever deflections of 0.2 pm [48].

Since the measured error in the topography is ± 3 nm (Fig. 4.8), and the estimated size of the nanoparticles is 50 ± 10 nm, it shows that the sensitivity of the AFM (0.2 pm) is sufficient to detect these nanoparticles and the changes in surface roughness.

5.3 Isolating magnetic interaction from short-range surface interaction and background interaction

5.3.1 Background interaction

The results suggest that scanning with a pseudo-demagnetised MFM tip (Fig. 4.9b) and AFM tip (Fig. 4.9d), that the long-range phase shift is not significant, compared to the magnetic signal (Fig. 4.10). The MFM measurements show that the background interaction is approximately 6 - 7 °, which could be due to the pseudo-demagnetised MFM tip still interacting slightly with the MFM magnet (Fig. 4.9b). Relative to this value, the phase shift is negligible. These results, therefore, suggest that there is not enough evidence to indicate that electrostatic interaction occurs between the MFM and AFM tips and the sample surface. In addition, other authors [21, 50] show that electrostatic interaction above embedded nanoparticles in a dielectric material is negligible, although the nanoparticles in sample A are partially embedded.

5.3.2 Short-range surface interaction

Measurements were done to compare the MFM and AFM phase shift above the nanoparticles. Above sample A, the MFM phase shift is larger negative than the AFM phase shift suggesting strong magnetic interaction between the nanoparticles and the tip (4.12b), lasting even up to 300 nm. However, the AFM phase shift appears to be negligible above 20 nm (Fig. 4.12b). The bacterium wall appears to be visible in the MFM phase maps (Fig. 4.10), suggesting non-magnetic interaction. However, this is likely due to nanoparticles surrounding the bacterium, as shown in Figs. 4.1, 4.6, 4.7.

MFM force spectroscopy shows that measurements above magnetic material have greater negative phase shift, than above non-magnetic material (Fig. 4.13c). This result was expected since above magnetic material the MFM tip-sample interaction should be stronger. At a distance greater than approximately 150 nm, the phase shift above all the points appears to converge together. This result suggests that the magnetic stray-field from the sample diverges above the surface. Similar phase shift is measured when the lateral distance between points is approximately the same as the

vertical distance above the surface, where the measurements are done. Very close to the surface (0-5 nm), the phase shift appears to be almost uniform between the points before diverging at greater heights. This suggests that the short-range forces dominate the tip-sample interaction in this height range.

Results of force spectroscopy using the AFM probe suggest that the phase shift above non-magnetic material is not distinguishable from that above magnetic material (Fig. 4.13f). This is expected since there should be no magnetic tip-sample interaction. Therefore, the difference in phase shift between points is likely due to the roughness in nanoscale topography. This information suggests that the AFM tip is still sensitive to the topography roughness, up to approximately 12 nm above the surface.

5.3.3 Comparing magnetic signals from Pd-Fe and Pd nanoparticles (sample A and B)

Measurements above A and B were compared to study the difference in magnetic signal between the two samples (Fig. 4.15). The nanoparticles in sample B were not distinguishable in the MFM images (Fig. 4.14). Since the composition of sample B (Pd) is different from sample A (Pd-Fe), it could be that different sizes of nanoparticles are produced by the bacteria and, therefore, could require higher resolution to image them.

The background MFM phase shift above sample A is greater negative than above sample B (Figs. 4.12a and 4.14i). This result was unexpected since the MFM magnet should result in the same phase shift independent of the sample. However, the phase shift contribution from the MFM magnet is dependent on height. Hence, samples A and B could be of different thickness, which results in different measured background phase shift. A second possibility is that even in the region used to calculate the background phase shift, the nanoparticle stray-field could be interacting with the MFM tip, causing different background measurements. Alternatively, one of the samples could be shifted from the centre of the MFM magnet.

In summary, the MFM phase shift measured above nanoparticles in sample A is much larger negative than the AFM phase shift. It is significant at considerable heights (100-300 nm) above the sample, where the AFM signal has already decayed. The AFM phase shift is shown to be negligible above approximately 20 nm. The MFM phase shift measured above sample B is less negative than above sample A. However, it is still greater negative than the AFM phase shift above

sample A. This information suggests weak magnetic tip-sample interaction above sample B due to Pd nanoparticles present there, which could be on the same level as short-range interaction at the same height. The AFM and MFM probes do, however, have different properties (see Table 2), and therefore systematic error would be useful to discuss.

5.4 Comparison of MFM and AFM probes

Next, measurements were done above sample A and C to study the MFM and AFM probe behaviour. On the nanoscale, results show the AFM tip can resolve smaller peaks than the MFM tip (Fig. 4.16e). This result is likely due to the differences in geometry of the tips (see Table 2), since the AFM tip has a nominal radius of 1 nm, compared to 50 nm for the MFM tip.

Results also show that the MFM topography is rougher than the AFM topography (Table 3) and that there is a vertical difference d in the measured topographies (Fig. 4.16e, Appendix Fig. A.1). This difference could be due to the different probe properties. One explanation could be that the tip volume affects the interaction with the surface. Although the tip-sample convolution is expected to be a lateral one, this suggests a contribution from the volume (Appendix Fig. A.1). The authors in [67] and [18], suggest that using the vertical height of features is more accurate than using lateral distance, as shown by the schematic in Fig. 2.12. However, these results suggest that the different volumes/radii of the MFM and AFM tips have a significant influence over the measurements, as mentioned in theory [44, 45].

Although the AFM and MFM nanoscale topography measurements show differences, the topographies are reproduced relatively well on the micron scale (Fig. 4.17c). However, the corresponding phase shift in these measurements suggests that the MFM and AFM interaction above the surface of the sample is not the same (Fig. 4.17d). The AFM and MFM phase shift at 20 nm above the surface are similar in profile but offset by 10 - 15 °. Force spectroscopy measurements are also consistent with this (Fig. 4.18c, d). Since the MFM magnet is not present, and the phase shift difference is present at low heights, where short-range interaction is dominant, suggests that the interaction is non-magnetic. Hence, the difference is phase shift could be due to probe properties.

However, it appears that there is a systematic error in the measurements. Figs. 4.17c and 4.18c-d, show that the phase shift is very large negative far above the sample surface, which is not consistent with previous measurements on sample A (Figs. 4.12 and 4.13).

In summary, despite this systematic uncertainty in the phase measurements, the topography measurements give evidence to suggest that the measurements from the AFM and MFM probes are not comparable. In addition, in Eqs. 2 - 3, the measurements, as well as being dependent on the amplitude setpoint, also depend on (i) the quality factor Q , (ii) the spring constant k, (iii) the drive frequency, and (iv) drive amplitude. Since these values are not the same (see Table 2), it suggests that even using the same amplitude setpoint for measurements, the AFM and MFM probes do not behave the same.

5.5 MFM artefacts and interpreting the signals

Characterising the external magnetic field and tip-sample interaction is crucial to interpret MFM results. Understanding the difference between artefact and "real" magnetism is important. A useful parameter in this differentiation is the scanning direction, which the microscope software allows changing. By changing the scan direction, unusual features are observed in phase shift maps. Dark and light contrast appears on opposite sides of nanoparticles, with respect to the cantilever scanning direction (Fig. 4.19e-h). The maximum error in the scan is 13 % of the setpoint. However, this does not indicate the error contribution to the phase shift. Fig. 4.19i suggests the error signal (from the feedback loop) is not entirely responsible for this behaviour. Higher-resolution imaging (at another nanoparticle) appears not to show this behaviour (Fig. 4.20e-h), since relatively uniform contrast is found. Although there is some non-uniformity, this could be explained by the topography effects (Fig. 4.21a-d). Repeating higher resolution imaging at another nanoparticle or agglomerate of nanoparticles shows that dark and light contrast appears on the same side, independent of the scan direction.

The source of these results appears to be unlikely due to MFM inhomogeneity [61], or tilted scanning [62] since the measurements from all three experiments seem to rule these out. Suppose the interaction was due to (i) MFM inhomogeneity in the MFM magnet alignment. In that case, it is expected that dark and light contrast should always appear on the same side, like in Fig. 4.21, independent of scanning direction. If the interaction were due to (ii) tilted scanning, the dark and light contrast is expected to constantly change with scanning direction, like in Fig. 4.19.

If we, therefore, consider this interaction to be magnetic, but not from an artefact, it appears that in Figs. 4.19 and 4.21 two directions of the nanoparticle magnetisation is detected, and in Fig. 4.20 that one direction is detected. Since in Fig. 4.19 the contrast changes with the cantilever scan

direction, it suggests that the tip orients the nanoparticle magnetic moment as it scans. However, in Fig. 4.21, the interaction suggests the tip magnetisation is insufficient to orient the nanoparticles. Whether the nanoparticles are single-domain (superparamagnetic) or multi-domain (ferromagnetic) could be responsible for this behaviour.

6 Conclusion

In conclusion, characterising biologically-produced Pd and Pd-Fe nanoparticles using MFM and AFM was very productive. Great focus was put on locating the nanoparticles with respect to bacteria and investigating the possible use of several slices of the sample for this purpose. In addition, studies were done to isolate and interpret magnetic interaction.

Though the size of the Pd-Fe nanoparticles was estimated to be 50 $\pm$ 10 nm, there is some degree of inaccuracy since the estimation relies on measurements performed above the surface (at about 20 nm). Nanoparticles were found outside of the bacteria wall and possibly in the membrane. However, artefacts were found in the analysis of results, and therefore more research is necessary to conclude this study. It was shown that consecutive imaging slices of resin sample enable the three-dimensional reconstruction of bacteria. This investigation outlines the excellent potential for consecutive imaging in the localisation of nanoparticles within the volume and membranes of bacteria.

The magnetic interaction measured above Pd and Pd-Fe nanoparticles was isolated from short-range and background interaction using MFM and AFM. Although the Pd-Fe nanoparticles have a strong magnetic signal far above the surface ($\geq$ 20 nm), the measurements above Pd nanoparticles were found to be on a similar level with the AFM measurements. However, the MFM and AFM probe measurements above the Pd-Cu sample without the MFM magnet were found somewhat inconsistent with each other. This suggests that the AFM measurements cannot be subtracted from the MFM measurements to calculate the magnetic signal.

Magnetic interaction and artefacts using MFM were studied. Results show that the interaction above nanoparticles changes significantly between measurements of different nanoparticles on the sample. The measurements suggest that both one and two magnetisation directions of the nanoparticles have been detected. This result could be due to the superparamagnetic or the ferromagnetic nature of the nanoparticles.

7 Future Outlook

Suggestions for possible future work are the following:

1. For the characterisation of the size of nanoparticles, it would be useful to compare results with TEM analysis.

2. Since the consecutive imaging of resin slices was found to be very successful, it would be beneficial to investigate the localisation of nanoparticles in bacteria further. Repeating measurements with a new tip and a slightly higher resolution around the bacterial membranes would be helpful. If the sample preparation can be changed to enable thinner slices of resin to be cut and analysed in MFM, this would also be of great benefit, allowing more cross-sections of a single bacterium to be imaged.

3. To further isolate the magnetic interaction from the background and short-range interaction, it could be possible to acquire probes with similar properties. However, even more appropriate would be using a method like CM-MFM [49]. This method would allow more accurate measurements of the short-range and background interaction since the probe is unchanged physically, only magnetically. The method is relatively simple, requiring only an electromagnetic coil and a piece of floppy disk as a reference sample. However, it does have limitations of its own.

4. For the interpretation of the magnetic signal, it could be interesting to simulate the magnetic interaction using software, such as object-oriented micro-magnetic framework (OOMMF), which is free to use. In addition, applying an in-plane magnetic field was found by other authors [64] to be very useful for magnetic characterisation, and this could also be pursued.

References

[1] T. T. V. Phan, T.-C. Huynh, P. Manivasagan, S. Mondal, and J. Oh, "An up-to-date review on biomedical applications of palladium nanoparticles," *Nanomaterials*, vol. 10, p. 66, Dec 2019.

[2] T. T. V. Phan, T.-C. Huynh, P. Manivasagan, S. Mondal, and J. Oh, "An up-to-date review on biomedical applications of palladium nanoparticles," *Nanomaterials*, vol. 10, no. 1, p. 66, 2020.

[3] Z. Li and X. Meng, "Recent development on palladium enhanced photocatalytic activity: A review," *Journal of Alloys and Compounds*, vol. 830, p. 154669, 2020.

[4] M. Moreno-Manas and R. Pleixats, "Formation of carbon- carbon bonds under catalysis by transition-metal nanoparticles," *Accounts of chemical research*, vol. 36, no. 8, pp. 638–643, 2003.

[5] M. A. Miller, B. Askevold, H. Mikula, R. H. Kohler, D. Pirovich, and R. Weissleder, "Nano-palladium is a cellular catalyst for in vivo chemistry," *Nature Communications*, vol. 8, no. 1, 2017.

[6] S. Angappane, J. Park, Y. Jang, T. Hyeon, and J.-G. Park, "Magnetic Pd nanoparticles: effects of surface atoms," *Journal of Physics: Condensed Matter*, vol. 20, no. 29, p. 295209, 2008.

[7] T. Shinohara, T. Sato, and T. Taniyama, "Surface ferromagnetism of pd fine particles," *Physical Review Letters*, vol. 91, no. 19, p. 197201, 2003.

[8] A. Murani, A. Tari, and B. Coles, "Critical concentration for the onset of ferromagnetism in pd-ni alloys," *Journal of Physics F: Metal Physics*, vol. 4, no. 10, p. 1769, 1974.

[9] A. K. Gupta and M. Gupta, "Synthesis and surface engineering of iron oxide nanoparticles for biomedical applications," *biomaterials*, vol. 26, no. 18, pp. 3995–4021, 2005.

[10] A.-H. Lu, E. e. Salabas, and F. Schüth, "Magnetic nanoparticles: synthesis, protection, functionalization, and application," *Angewandte Chemie International Edition*, vol. 46, no. 8, pp. 1222–1244, 2007.

[11] M. Neamtu, C. Nadejde, V.-D. Hodoroaba, R. J. Schneider, L. Verestiuc, and U. Panne, "Functionalized magnetic nanoparticles: Synthesis, characterization, catalytic application and assessment of toxicity," *Scientific reports*, vol. 8, no. 1, pp. 1–11, 2018.

[12] A. M. Abu-Dief and S. M. Abdel-Fatah, "Development and functionalization of magnetic nanoparticles as powerful and green catalysts for organic synthesis," *Beni-Suef University Journal of Basic and Applied Sciences*, vol. 7, no. 1, pp. 55–67, 2018.

[13] K. Deplanche, R. D. Woods, I. P. Mikheenko, R. E. Sockett, and L. E. Macaskie, "Manufacture of stable palladium and gold nanoparticles on native and genetically engineered flagella scaffolds," *Biotechnology and bioengineering*, vol. 101, no. 5, pp. 873–880, 2008.

[14] M. Naghdi, M. Taheran, S. K. Brar, M. Verma, R. Y. Surampalli, and J. R. Valéro, "Green and energy-efficient methods for the production of metallic nanoparticles," *Beilstein journal of nanotechnology*, vol. 6, no. 1, pp. 2354–2376, 2015.

[15] X. Yang, Q. Li, H. Wang, J. Huang, L. Lin, W. Wang, D. Sun, Y. Su, J. B. Opiyo, L. Hong, *et al.*, "Green synthesis of palladium nanoparticles using broth of cinnamomum camphora leaf," *Journal of Nanoparticle Research*, vol. 12, no. 5, pp. 1589–1598, 2010.

[16] M. T. Matsena, S. M. Tichapondwa, and E. M. N. Chirwa, "Synthesis of biogenic palladium nanoparticles using citrobacter sp. for application as anode electrocatalyst in a microbial fuel cell," *Catalysts*, vol. 10, no. 8, p. 838, 2020.

[17] G. Cordova, B. Lee, and Z. Leonenko, "Magnetic force microscopy for nanoparticle characterization," *NanoWorld J*, vol. 2, no. 1, pp. 10–14, 2016.

[18] C. Iacovita, J. Hurst, G. Manfredi, P. Hervieux, B. Donnio, J. Gallani, and M. Rastei, "Magnetic force fields of isolated small nanoparticle clusters," *Nanoscale*, vol. 12, no. 3, pp. 1842–1851, 2020.

[19] M. Fuhrmann, A. Krivcov, A. Musyanovych, R. Thoelen, and H. Möbius, "The role of nanoparticles on topographic cross-talk in electric force microscopy and magnetic force microscopy," *physica status solidi (a)*, vol. 217, no. 13, p. 1900828, 2020.

[20] C. S. Neves, P. Quaresma, P. V. Baptista, P. A. Carvalho, J. P. Araújo, E. Pereira, and P. Eaton, "New insights into the use of magnetic force microscopy to discriminate between magnetic and nonmagnetic nanoparticles," *Nanotechnology*, vol. 21, no. 30, p. 305706, 2010.

[21] A. Krivcov, J. Schneider, T. Junkers, and H. Möbius, "Magnetic force microscopy of in a polymer matrix embedded single magnetic nanoparticles," *physica status solidi (a)*, vol. 216, no. 12, p. 1800753, 2019.

[22] B. Torre, G. Bertoni, D. Fragouli, A. Falqui, M. Salerno, A. Diaspro, R. Cingolani, and A. Athanassiou, "Magnetic force microscopy and energy loss imaging of superparamagnetic iron oxide nanoparticles," *Scientific reports*, vol. 1, no. 1, pp. 1–8, 2011.

[23] R. C. O'handley, *Modern magnetic materials: principles and applications*. Wiley, 2000.

[24] A. H. Morrish, *The Physical Principles of Magnetism*. Wiley-IEEE Press, 2001.

[25] G. C. Papaefthymiou, "Nanoparticle magnetism," *Nano Today*, vol. 4, no. 5, pp. 438–447, 2009.

[26] R. Skomski, "Nanomagnetics," *Journal of physics: Condensed matter*, vol. 15, no. 20, p. R841, 2003.

[27] W. Pei, H. Kumada, T. Natusme, H. Saito, and S. Ishio, "Study on magnetite nanoparticles synthesized by chemical method," *Journal of Magnetism and Magnetic Materials*, vol. 310, no. 2, pp. 2375–2377, 2007.

[28] G. Sergeev and K. Klabunde, "Chapter 10 - size effects in nanochemistry," in *Nanochemistry (Second Edition)* (G. Sergeev and K. Klabunde, eds.), pp. 275 – 297, Oxford: Elsevier, second edition ed., 2013.

[29] M. Respaud, J. Broto, H. Rakoto, A. Fert, L. Thomas, B. Barbara, M. Verelst, E. Snoeck, P. Lecante, A. Mosset, *et al.*, "Surface effects on the magnetic properties of ultrafine cobalt particles," *Physical Review B*, vol. 57, no. 5, p. 2925, 1998.

[30] P. Gambardella, S. Rusponi, M. Veronese, S. Dhesi, C. Grazioli, A. Dallmeyer, I. Cabria, R. Zeller, P. Dederichs, K. Kern, *et al.*, "Giant magnetic anisotropy of single cobalt atoms and nanoparticles," *Science*, vol. 300, no. 5622, pp. 1130–1133, 2003.

[31] T. Sun, Z. Zhang, J. Xiao, C. Chen, F. Xiao, S. Wang, and Y. Liu, "Facile and green synthesis of palladium nanoparticles-graphene-carbon nanotube material with high catalytic activity," *Scientific reports*, vol. 3, no. 1, pp. 1–6, 2013.

[32] K. Deplanche, J. Bennett, I. Mikheenko, J. Omajali, A. Wells, R. Meadows, J. Wood, and L. Macaskie, "Catalytic activity of biomass-supported pd nanoparticles: influence of the biological component in catalytic efficacy and potential application in 'green'synthesis of fine chemicals and pharmaceuticals," *Applied Catalysis B: Environmental*, vol. 147, pp. 651–665, 2014.

[33] O. V. Singh, *Bio-nanoparticles: biosynthesis and sustainable biotechnological implications*. John Wiley & Sons, 2015.

[34] M. N. Alam, N. Roy, D. Mandal, and N. A. Begum, "Green chemistry for nanochemistry: exploring medicinal plants for the biogenic synthesis of metal nps with fine-tuned properties," *Rsc Advances*, vol. 3, no. 30, pp. 11935–11956, 2013.

[35] S. Mishra and H. Singh, "Biosynthesized silver nanoparticles as a nanoweapon against phytopathogens: exploring their scope and potential in agriculture," *Applied microbiology and biotechnology*, vol. 99, no. 3, pp. 1097–1107, 2015.

[36] J. R. Lloyd, P. Yong, and L. E. Macaskie, "Enzymatic recovery of elemental palladium by using sulfate-reducing bacteria," *Applied and Environmental Microbiology*, vol. 64, no. 11, pp. 4607–4609, 1998.

[37] H. Corte-León, V. Neu, A. Manzin, C. Barton, Y. Tang, M. Gerken, P. Klapetek, H. W. Schumacher, and O. Kazakova, "Comparison and validation of different magnetic force microscopy calibration schemes," *Small*, vol. 16, no. 11, p. 1906144, 2020.

[38] Y. Martin and H. K. Wickramasinghe, "Magnetic imaging by "force microscopy" with 1000 Å resolution," *Applied Physics Letters*, vol. 50, no. 20, pp. 1455–1457, 1987.

[39] G. Binnig, C. F. Quate, and C. Gerber, "Atomic force microscope," *Physical review letters*, vol. 56, no. 9, p. 930, 1986.

[40] A. de Lozanne, "Application of magnetic force microscopy in nanomaterials characterization," *Microscopy Research and Technique*, vol. 69, no. 7, pp. 550–562, 2006.

[41] M. Savla, R. P. Pandian, P. Kuppusamy, and G. Agarwal, "Magnetic force microscopy of an oxygen-sensing spin-probe," *Israel Journal of Chemistry*, vol. 48, no. 1, pp. 33–38, 2008.

[42] J. Legleiter, "The effect of drive frequency and set point amplitude on tapping forces in atomic force microscopy: simulation and experiment," *Nanotechnology*, vol. 20, no. 24, p. 245703, 2009.

[43] D. Passeri, C. Dong, M. Reggente, L. Angeloni, M. Barteri, F. A. Scaramuzzo, F. De Angelis, F. Marinelli, F. Antonelli, F. Rinaldi, *et al.*, "Magnetic force microscopy: Quantitative issues in biomaterials," *Biomatter*, vol. 4, no. 1, p. e29507, 2014.

[44] J. N. Israelachvili, *Intermolecular and surface forces*. Academic press, 2011.

[45] H. Skulason and C. D. Frisbie, "Rupture of hydrophobic microcontacts in water: correlation of pull-off force with afm tip radius," *Langmuir*, vol. 16, no. 15, pp. 6294–6297, 2000.

[46] F. L. Leite, C. C. Bueno, A. L. Da Róz, E. C. Ziemath, and O. N. Oliveira, "Theoretical models for surface forces and adhesion and their measurement using atomic force microscopy," *International journal of molecular sciences*, vol. 13, no. 10, pp. 12773–12856, 2012.

[47] A. Kühle, A. H. Sørensen, J. B. Zandbergen, and J. Bohr, "Contrast artifacts in tapping tip atomic force microscopy," *Applied Physics A: Materials Science & Processing*, vol. 66, no. S, pp. S329–S332, 1998.

[48] V. Bert, *Atomic force microscopy*. Springer, 2019.

[49] L. Angeloni, D. Passeri, M. Reggente, D. Mantovani, and M. Rossi, "Removal of electrostatic artifacts in magnetic force microscopy by controlled magnetization of the tip: application to superparamagnetic nanoparticles," *Scientific reports*, vol. 6, no. 1, pp. 1–14, 2016.

[50] A. Krivcov, J. Ehrler, M. Fuhrmann, T. Junkers, and H. Möbius, "Influence of dielectric layer thickness and roughness on topographic effects in magnetic force microscopy," *Beilstein journal of nanotechnology*, vol. 10, no. 1, pp. 1056–1064, 2019.

[51] M. Fuhrmann, A. Musyanovych, R. Thoelen, S. von Bomhard, and H. Möbius, "Magnetic imaging of encapsulated superparamagnetic nanoparticles by data fusion of magnetic force microscopy and atomic force microscopy signals for correction of topographic crosstalk," *Nanomaterials*, vol. 10, no. 12, p. 2486, 2020.

[52] A. Krivcov, T. Junkers, and H. Möbius, "Understanding electrostatic and magnetic forces in magnetic force microscopy: towards single superparamagnetic nanoparticle resolution," *Journal of Physics Communications*, vol. 2, no. 7, p. 075019, 2018.

[53] L. H. Li and Y. Chen, "Electric contributions to magnetic force microscopy response from graphene and MoS2 nanosheets," *Journal of Applied Physics*, vol. 116, no. 21, p. 213904, 2014.

[54] M. Jaafar, O. Iglesias-Freire, L. Serrano-Ramón, M. R. Ibarra, J. M. de Teresa, and A. Asenjo, "Distinguishing magnetic and electrostatic interactions by a kelvin probe force microscopy–magnetic force microscopy combination," *Beilstein journal of nanotechnology*, vol. 2, no. 1, pp. 552–560, 2011.

[55] V. Cambel, P. Eliáš, D. Gregušová, J. Martaus, J. Fedor, G. Karapetrov, and V. Novosad, "Magnetic elements for switching magnetization magnetic force microscopy tips," *Journal of magnetism and magnetic materials*, vol. 322, no. 18, pp. 2715–2721, 2010.

[56] V. Novotná, J. Vejpravová, V. Hamplová, J. Prokleška, E. Gorecka, D. Pociecha, N. Podoliak, and M. Glogarová, "Nanocomposite of superparamagnetic maghemite nanoparticles and ferroelectric liquid crystal," *RSC advances*, vol. 3, no. 27, pp. 10919–10926, 2013.

[57] V. Raman, A. Bose, B. D. Olsen, and T. A. Hatton, "Long-range ordering of symmetric block copolymer domains by chaining of superparamagnetic nanoparticles in external magnetic fields," *Macromolecules*, vol. 45, no. 23, pp. 9373–9382, 2012.

[58] C. Xu, K. Ohno, V. Ladmiral, D. E. Milkie, J. M. Kikkawa, and R. J. Composto, "Simultaneous block copolymer and magnetic nanoparticle assembly in nanocomposite films," *Macromolecules*, vol. 42, no. 4, pp. 1219–1228, 2009.

[59] M. Raşa and A. Philipse, "Scanning probe microscopy on magnetic colloidal particles," *Journal of magnetism and magnetic materials*, vol. 252, pp. 101–103, 2002.

[60] K. K. Sinha, "Artifacts in afm." Available: https://kk-sinha.blogspot.com/2014/09/artifacts-in-afm.html, 2009. Accessed on: January 8, 2021. [Online].

[61] I. Cinar, D. Lacour, F. Montaigne, V. Puliafito, S. P. Watelot, M. Hehn, G. Finocchio, O. Ozatay, and T. Hauet, "Artifacts in magnetic force microscopy under in-plane applied magnetic field: Magnetic bubble as a case study," *Journal of Magnetism and Magnetic Materials*, vol. 500, p. 166296, 2020.

[62] G. Ciuta, F. Dumas-Bouchiat, N. M. Dempsey, and O. Fruchart, "Some aspects of magnetic force microscopy of hard magnetic films," *IEEE Transactions on Magnetics*, vol. 52, no. 9, pp. 1–8, 2016.

[63] J. Instruments, *Nanowizard 3 User Manual*. JPK Instruments.

[64] V. L. Mironov, D. S. Nikitushkin, C. Bins, A. B. Shubin, and P. A. Zhdan, "Magnetic force microscope contrast simulation for low-coercive ferromagnetic and superparamagnetic nanoparticles in an external magnetic field," *IEEE Transactions on Magnetics*, vol. 43, no. 11, pp. 3961–3963, 2007.

[65] S. Schreiber, M. Savla, D. V. Pelekhov, D. F. Iscru, C. Selcu, P. C. Hammel, and G. Agarwal, "Magnetic force microscopy of superparamagnetic nanoparticles," *Small*, vol. 4, no. 2, pp. 270–278, 2008.

[66] D. Nečas, P. Klapetek, V. Neu, M. Havlíček, R. Puttock, O. Kazakova, X. Hu, and L. Zajíčková, "Determination of tip transfer function for quantitative mfm using frequency domain filtering and least squares method," *Scientific Reports*, vol. 9, Jul 2019.

[67] L. Angeloni, D. Passeri, S. Corsetti, D. Peddis, D. Mantovani, and M. Rossi, "Single nanoparticles magnetization curves by controlled tip magnetization magnetic force microscopy," *Nanoscale*, vol. 9, no. 45, pp. 18000–18011, 2017.

[68] J. Claxton, N. Joudeh, A. Røyne, D. Linke, and P. Mikheenko, "Sequential magnetic mapping of bacteria loaded with pd-fe nanoparticles," in *2020 IEEE 10th International Conference Nanomaterials: Applications & Properties (NAP)*, pp. 1–5, IEEE, 2020.

A Comparison of MFM and AFM probes

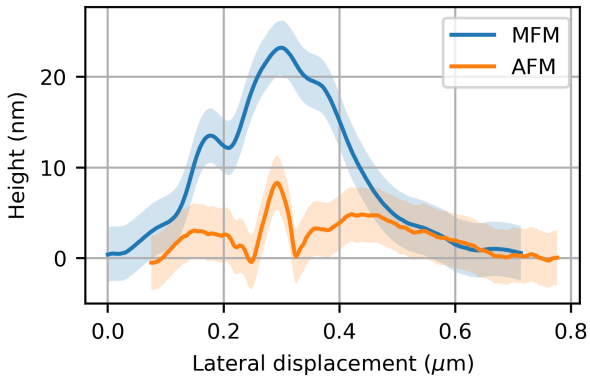

Figure A.1: MFM and AFM topography after identical plane subtraction, along the topography in Fig. 4.16c, d. The error used is from the error found in Fig. 4.8b with setpoint equal to 0.3 V.

B MFM artefacts and interpreting signals

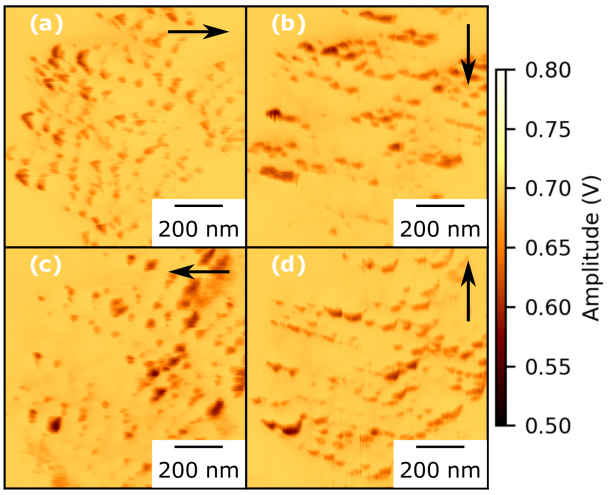

Figure B.1: MFM amplitude maps at four scanning angles, recorded at 19 nm above the surface. The scan angles are: (a) 90 °, (b) 0 °, (c) 180 °, and (d) -90 °. The black arrows indicate the cantilever scanning direction.

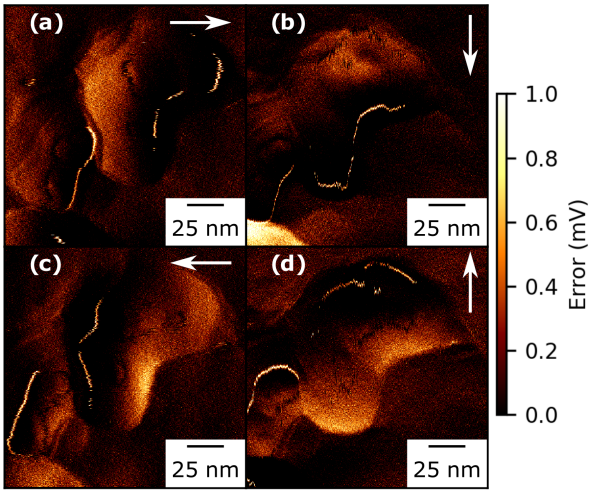

Figure B.2: MFM error maps, at four scanning angles. The scan angles are: (a) 90 °, (b) 0 °,(c) 180 °, and (d) -90 °. The error maps are recorded at 20 nm above the surface of sample A. The white arrows indicate the cantilever scanning direction.

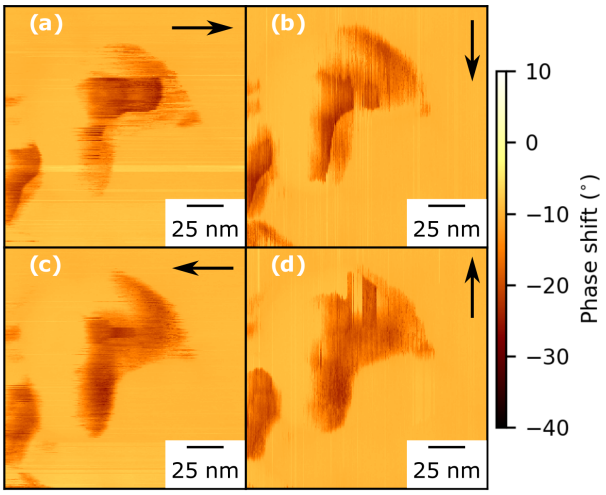

Figure B.3: MFM phase maps at four scanning angles, recoreded at 22 nm above the surface. The scan angles are: (a) 90 °, (b) 0 °,(c) 180 °, and (d) -90 °. The black arrows indicate the cantilever scanning direction.

C Sequential magnetic mapping - NAP 2020

In reference to IEEE copyrighted material which is used with permission in this thesis, the IEEE does not endorse any of University of Oslo's products or services.

IEEE International Conference on
"Nanomaterials: Applications & Properties" (NAP-2020)
Sumy, Ukraine, 9-13 Nov. 2020

Sequential Magnetic Mapping of Bacteria Loaded with Pd-Fe Nanoparticles

James Claxton
Department of Physics
University of Oslo
Oslo, Norway
j.b.claxton@fys.uio.no

Nadeem Joudeh
Department of Biosciences
University of Oslo
Oslo, Norway
nadeem.joudeh@ibv.uio.no

Anja Røyne
Department of Physics
University of Oslo
Oslo, Norway
anja.royne@fys.uio.no

Dirk Linke
Department of Biosciences
University of Oslo
Oslo, Norway
dirk.linke@ibv.uio.no

Pavlo Mikheenko
Department of Physics
University of Oslo
Oslo, Norway
pavlo.mikheenko@fys.uio.no

***Abstract*— Magnetic nanoparticles are of widespread use in nanotechnology. Palladium nanoparticles are among the most unusual since they combine magnetism with high catalytic activity. These nanoparticles could be obtained biologically by exposing bacteria to a palladium salt. However, due to the small size and weak magnetism, it is challenging to measure their magnetic properties. One of the solutions to enhance their magnetism is to incorporate a small number of iron atoms into them. After this procedure, the nanoparticles and bacteria can be embedded in resin and characterized by magnetic force microscopy. This technique allows imaging cross-sections of the bacteria with nanoparticles but cannot give information from the depth of the sample. Here we report on an approach partially solving this problem. Its novelty lies in measurements of consecutive thin slices of resin, which allows mapping cross-sections of individual bacteria and different parts of the material surrounding the same bacterium. An interesting observed feature is the formation of magnetic chains of nanoparticles outside of the bacteria.**

Keywords*— *Palladium nanoparticles, magnetic mapping, bacteria, magnetic force microscopy

I. Introduction

Magnetic nanoparticles are becoming indispensable tools in nanotechnology. Their applications range from magnetic recording media [1] to delivery of drugs [2] and treatment of cancer [3]. Special attention is attracted to palladium (Pd) nanoparticles that become magnetic when their size is in the range of a few nanometers [4,5]. Combined with excellent catalytic properties, these nanoparticles are especially efficient in cancer treatment [6]. A biological method for producing Pd nanoparticles in large amounts is to introduce bacteria to a Pd salt solution [7]. In their exchange with the environment, bacteria can supply electrons for redox reactions and efficiently reduce Pd salts from solution due to the very high redox potential of the latter [8,9]. Adding iron (Fe) salt to the solution allows obtaining Pd particles that incorporate a small amount of Fe, which strongly increases their magnetism [10]. It could be straightforward to use these Pd-Fe nanoparticles for applications, but it is not easy to measure their magnetic properties. Here a technique is reported allowing doing this with the help of magnetic force microscopy (MFM).

II. Experimental

A. Magnetic Force Microscopy

Magnetic force microscopy (MFM) [11-13] is a technique allowing mapping the magnetic properties of a sample with a magnetic tip, which is scanned above its surface. In order to distinguish between magnetic and Van der Waals forces, which are acting on the tip at small distances, a two-pass scanning technique is used [11,12]. In the first pass, topography close to the surface is mapped. In the next scan, the probe is moved along a path following the measured topography, but at a larger height, so that the probe-sample distance is kept constant. If the height is large enough, Van der Waals forces become weak, and the pure magnetic response can be measured. According to [11,13,14], the shift in the phase of oscillations, if AC mode is used, is proportional to the gradient of force acting on the tip. The measurements were done using JPK NanoWizard 4.0 in AC mode at a frequency of about 74 kHz in an applied field of 0.58 T, created by a permanent magnet within the sample holder. The probes used were manufactured by Nanosensors, model type PPP-MFMR-10, with a tip radius of approximately 50 nm.

B. Production and Preparation of Samples

A single colony of *Escherichia coli* BW25113 strain was inoculated into 10 ml lysogeny broth (LB) medium in a test tube overnight at 37 °C while shaking it at 200 rpm. On the next day, 1 ml of this medium was used to inoculate 49 ml fresh LB medium in a 250 ml flask. The flask was also incubated at 37 °C while shaking at the same speed until the optical density ($O.D._{600}$) reached 0.5. The medium was transferred to a 50 ml falcon tube and centrifuged at 4250 g for 10 mins. The supernatant was removed, and the pellet was resuspended in 10 ml 20 mM pH 7 3-(N-morpholino) propanesulfonic acid (MOPS) buffer. This washing step was done two more times, except for the last round, the pellet was resuspended in 8 ml 20 mM pH 7 MOPS buffer. 1 ml of this suspension was transferred to a 1.5-ml Eppendorf tube. 1 mM of sodium tetrachloropalladate (Na_2Cl_4Pd) and 1 mM of iron III chloride ($FeCl_3$) (both dissolved in 0.01M nitric acid) were added to the tube, shaken well by hand, and incubated for 1 hour. Then, 10 mM sodium formate was added to the

tube to start the reduction. The suspensions turned black within 20 minutes.

Pd-Fe loaded bacteria were washed twice with distilled water by centrifuging at 5900 g for 2 min. After the second centrifugation step, the pellet was resuspended in 0.5 ml fixative solution (4% paraformaldehyde and 2% glutaraldehyde (w/v) dissolved in 20 mM pH 7 MOPS buffer) and left for 10 minutes at room temperature. Another round of fixation was done with the same concentration of the solution, and the sample was left in the fridge overnight. On the next day, the sample was washed twice with distilled water by centrifuging it at 3500 g for 10 minutes. Then, the sample was dehydrated by using an ascending ethanol concentration series (50, 70, 90, 96, and 100%). The sample was incubated with each concentration for 10 min except for the last concentration. For the last concentration, four rounds of dehydration were done, each taking 15 min. Next, one additional round with 100% acetone was applied for 15 minutes. Lastly, one round of 1:1 acetone to epoxy was done overnight, leaving the cap off; therefore, the epoxy concentration slowly increased. The next day, the sample was centrifuged at 3500 g for 10 minutes, then 0.5 mL of 100% epoxy was added and incubated for 1 hour at room temperature. Afterward, the tube was moved to the oven and incubated at 60 $^{\circ}$C for three days. The embedded sample was then sliced with a diamond knife into 0.5-1 μm thin slices. The slices were moved in a water droplet, put on smooth glass slides, and left for the water to evaporate. After evaporation of water, the slices firmly stick on the slides, ready for MFM measurements. The thickness of the slices was kept above 500 nm. The reason for this was that the sliced resin would bend and fold if slices are too thin. Very flat surfaces were found to be of key importance for MFM imaging at high resolution.

C. Sequential MFM Imaging

With the accurate cutting of the slices and setting them to the glass, they form a chain, in which each next slice was below (or above) the previous one in the sliced volume of resin. A fragment of a chain of slices is shown in Fig. 1. Imaging slices individually allows us to characterize different cross-sections of the resin, which may include cuts of the same bacteria and give information about the three-dimensional distribution of nanoparticles around them. Collecting different parameters of tip oscillation during the scans allows reconstructing both topography and magnetic properties of bacteria and nanoparticles.

Finding the same group of bacteria on each slice requires considerable effort. Its approximate position was determined using an optical microscope with a camera above the MFM stage designed to see a cantilever above a slice. When scanning the surface, large areas (90 x 90 μm^2) were initially mapped in order to compare features on a large scale. Scanning an area larger than 20 x 20 μm^2 at a typical scan rate of 1 Hz is usually not recommended, as the tip moves across the surface too rapidly. Therefore, to achieve desirable resolution, the scan rate was reduced to 0.2 Hz doing the measurement much slower than usual.

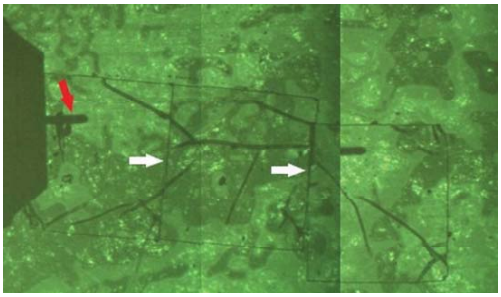

Fig. 1. Optical image of the slices of bacteria prepared for MFM imaging. The red arrow indicates the probe cantilever and the white arrows indicate the edges between slices of resin.

III. Results and Discussion

A. Magnetic Mapping of Pd-Fe Nanoparticles

Magnetic mapping was done with the two-pass technique at an optimal distance of 20 nm above the surface, at which Van der Waals forces become weak, but magnetic forces are still strong. Fig. 2 shows a selected magnetic map with clearly visible Pd-Fe nanoparticles concentrated around the cross-section of bacteria and forming extended magnetic chains and clusters. The nanoparticles are also seen on the outline of the bacteria. In the figure, the phase shift is proportional to the gradient of the magnetic force acting on the tip. Negative (dark) contrast represents the attraction of the tip to a nanoparticle. In a few places, the attraction is replaced by repulsion when the tip is coming too close to the surface, and the Van der Waals forces become a dominant force.

B. Sequential MFM Imaging

The sequential imaging was done on the slices of resin shown in Fig. 1. Fig. 3 gives amplitude maps (measured during the first pass) of a 90 x 90 μm^2 area selected in the same place on each of the three slices. The cantilever in Fig. 1 shows an approximate position inside the scanned area in the left-hand slice. In Figs. 3a, 3b, and 3c, the same features can be seen confirming that the imaged clusters of bacteria belong to the same place, and even that three cross-sections of the same bacteria could be found. The images differ slightly since some bacteria begin or end in the imaged slices. Specifically, the bacteria embedded with their long axis parallel to the surface are less likely to be found in the sequential slices. By imaging smaller regions, individual bacteria can be found in each slice. Fig. 4 shows higher resolution 20 x 20 μm^2 maps of the amplitude of oscillations in each slice of the resin. In these maps, a region of interest was a bacterium (outlined by dashed lines) with the chains of nanoparticles attached to it. These scans with even higher magnification are shown in Fig. 5. In Fig. 5a and 5b, the cross-sections of the bacterium are visible at the top with the

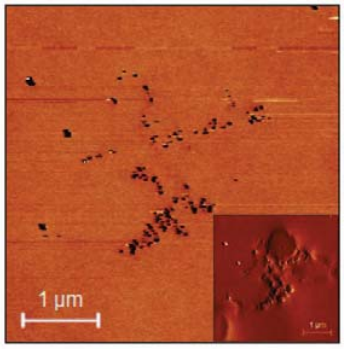

Fig. 2. Magnetic map of a cross-section of bacteria with chains of magnetic nanoparticles. The magnetic map displays the phase shift at lift height of 20 nm. Inset: Amplitude map representing topography of the same area.

attached nanoparticles. In Fig. 5c, the bulging at the edge of the bacterium is visible. These maps suggest that it is possible to image bacteria and nanoparticles in a three-dimensional way, allowing detailed topographical characterization. Fig. 6 shows the same areas as Fig. 5 but displays the shift in the phase of oscillations measured during the second pass. Negative (dark) and positive (light) contrast indicate attractive and repulsive interaction between the sample and the tip. Most nanoparticle-tip interactions appear

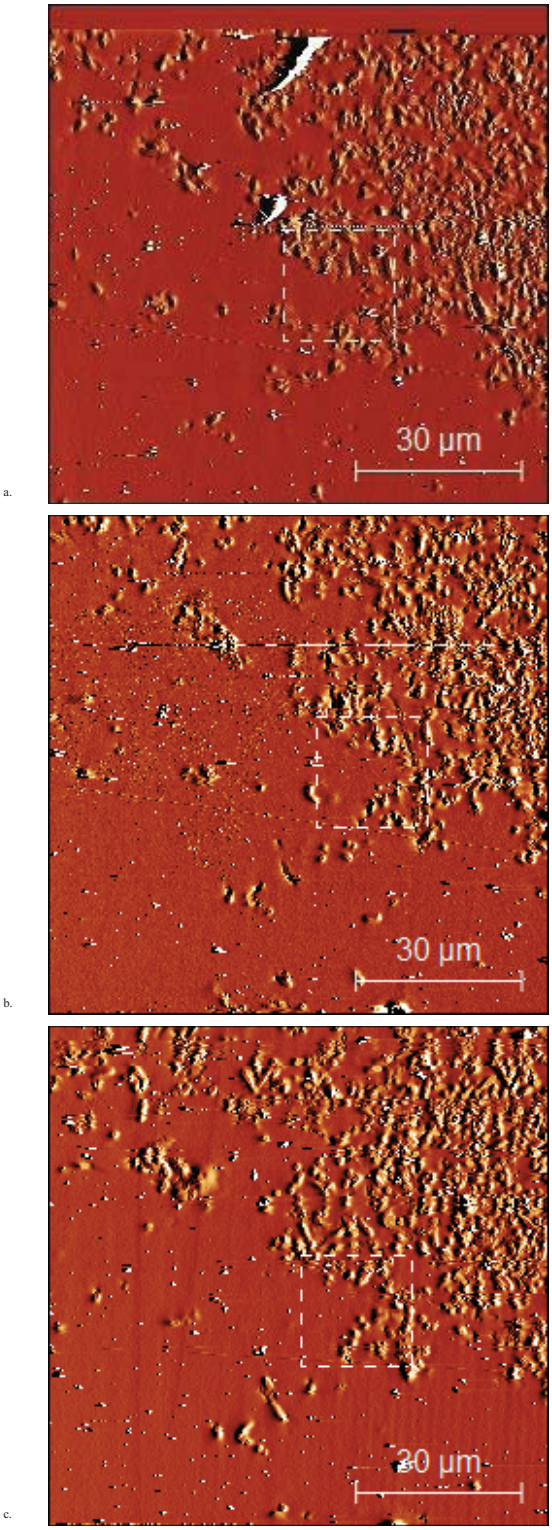

Fig. 3. Amplitude maps of three consecutive slices of resin measured during the first pass. An area of 90 x 90 µm^2 has been imaged.

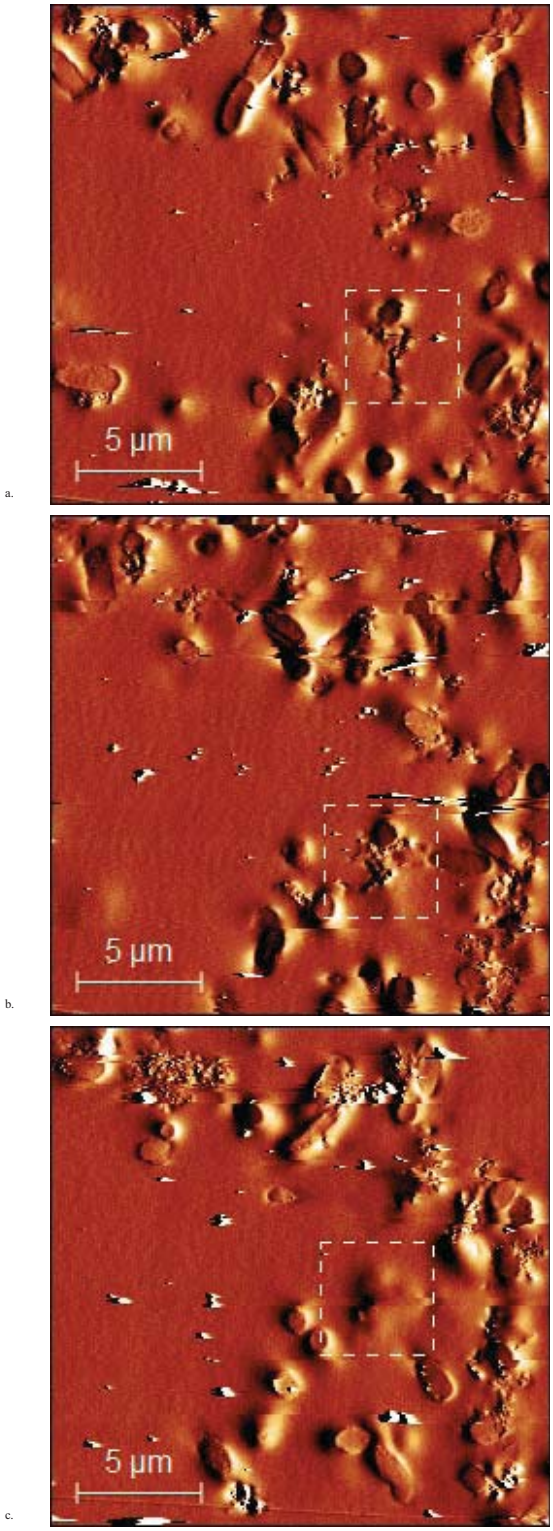

Fig. 4. Amplitude maps of three slices of resin measured during the first pass. A 20 x 20 µm^2 area has been imaged to compare individual bacteria. The location of these scans is indicated by the squares surrounded by dashed lines in Fig. 3.

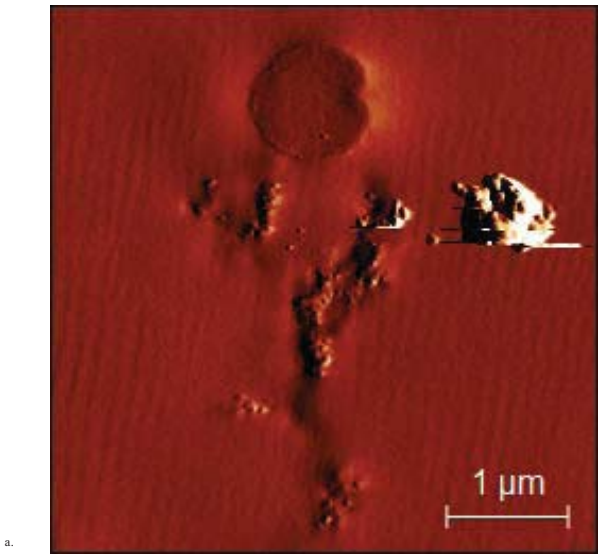

a.

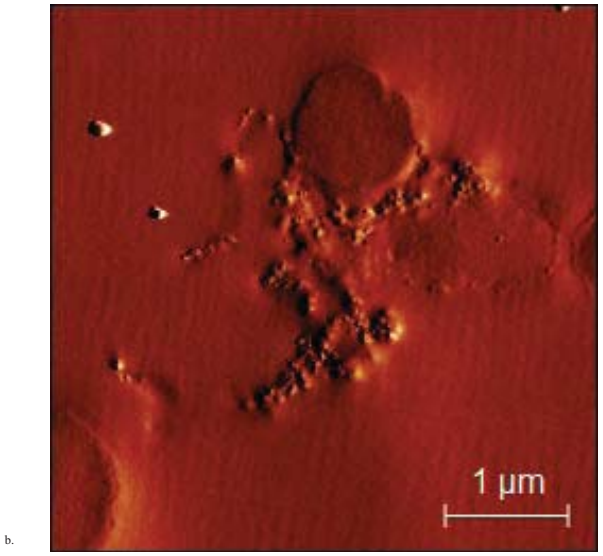

b.

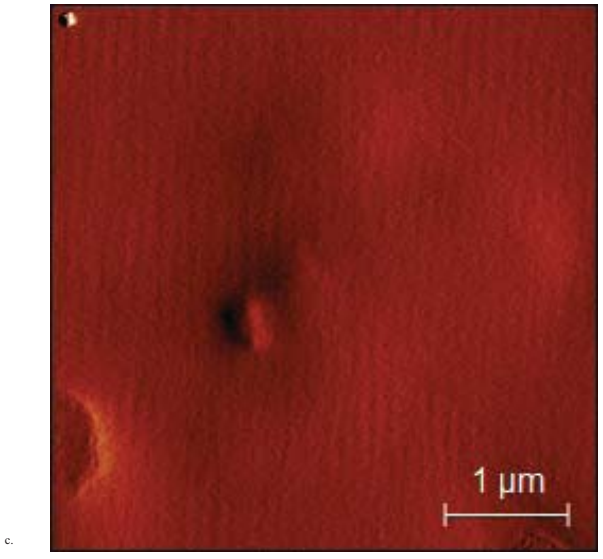

c.

Fig. 5. Amplitude maps of three slices of resin measured during the first pass. Nanoparticle chains are visible connected to bacteria. Location of scans is indicated by the squares surrounded by dashed lines in Fig. 4.

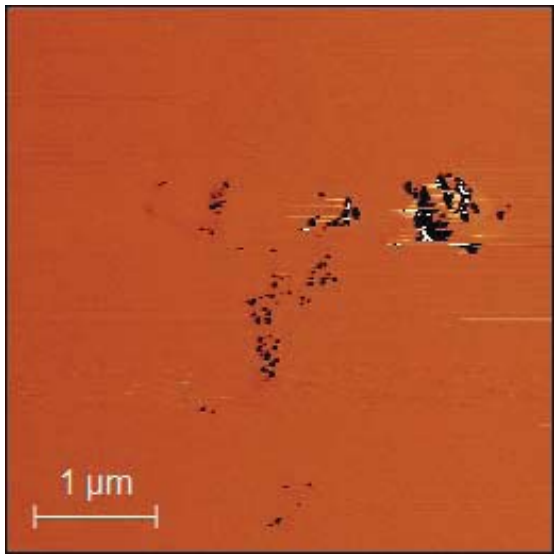

a.

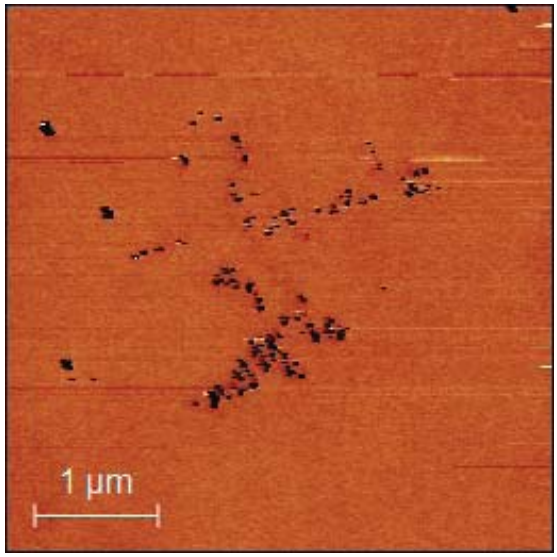

b.

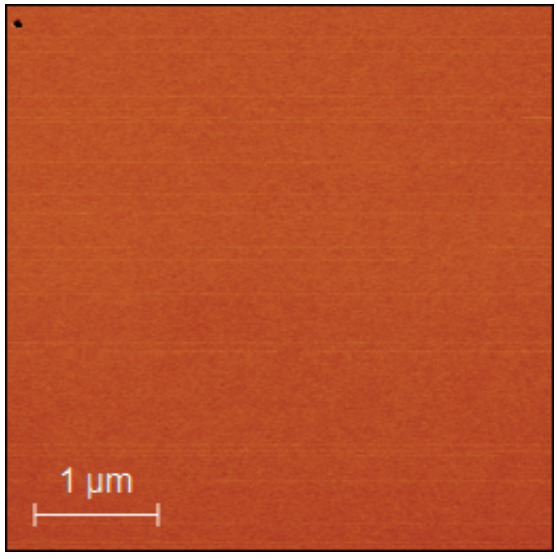

c.

Fig. 6. Phase maps of three slices of resin, measured during the second pass at lift height of 20 nm, in the same location as Fig. 5.

in negative contrast, indicating that the probe and nanoparticles are attracted to each other. On the other hand, there are clusters of nanoparticles (Fig. 6a), which show bright positive contrast, suggesting strong repulsion. The aim of this figure is to present the pure magnetic signal coming from the magnetic interaction between the sample and the tip. The clusters and chains of nanoparticles, the formation of which is currently not well understood, are found outside of the bacteria. During the sample preparation, the solution was washed several times. However, the chains and clusters remain attached to the bacteria, suggesting a strong chemical or magnetic interaction between the nanoparticles themselves and the bacteria and nanoparticles.

Images in Fig. 6 were recorded at lift height set to 20 nm. This height was selected experimentally for the following two reasons. Firstly, the bacterial cell walls, which are visible in Fig. 5, are not visible in Fig. 6, suggesting that atomic forces from a mainly non-magnetic material (bacteria still tend to accumulate weakly-magnetic pure Pd particles between the outer and inner membranes) are not acting on the tip. Secondly, it was found that mounting a non-magnetic probe and repeating the same scans at 20 nm above the sample resulted in negligible interaction between the sample and the tip. This suggests that 20 nm from the sample surface to the tip apex is a sufficient enough distance to measure a pure magnetic response with negligible atomic and electrostatic interaction. Fig. 7 shows a three-dimensional representation of the cross-sections. The approximate position of the bacteria is indicated by the blue ellipsoids.

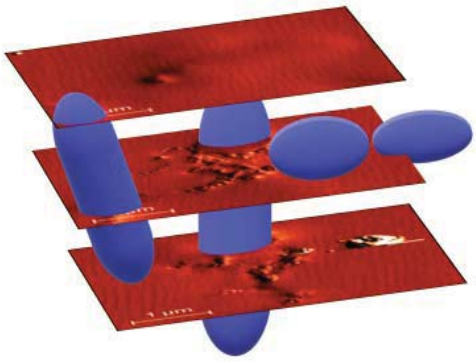

Fig. 7. A 3D representation of the slices of bacteria shown in Fig. 5. The sequence of slices is changed to better show bulging in the top layer.

IV. Conclusions

In conclusion, by embedding bacteria and biologically produced palladium-iron nanoparticles into a resin, slicing it into several cross-sections, and imaging the sequence of slices by magnetic force microscopy, a three-dimensional view of the structures was reconstructed. This method partially solves the problem of characterization restricted to the surface of the material only. In this case, the method has enabled nanoparticles and bacterial cross-sections deeper in the resin to be mapped. Unusual nanoparticle chains and clusters were observed extending from the bacterial cross-sections. The optimal height for mapping the magnetic response was found, which isolates the tip-sample magnetic interaction from the atomic interactions. This allows the magnetic characterization of nanoparticles to be performed without being affected by the short-range atomic forces. The iron atoms were added to enhance the magnetic response of the palladium nanoparticles, which now could be used in various applications with additional functionality, allowing to recover them magnetically after use.

Acknowledgment

This work is part of the Project "BEDPAN - Bio-engineered Palladium Nanoparticles," funded by the Research Council of Norway, RCN294605.

References

[1] J. Wang, "FePt magnetic nanoparticles and their assembly for future magnetic media," Proceedings of the IEEE, vol. 96, pp. 1847– 1863, December 2008.

[2] S. Mirza, M. S. Ahmad, M. I. A. Shah, and M. Ateeq, "Magnetic nanoparticles: drug delivery and bioimaging applications," in Metal Nanoparticles for Drug Delivery and Diagnostic Applications. Amsterdam: Elsevier, 2020, pp. 189– 213.

[3] J. Jose, R. Kumar, S. Harilal, G. E. Mathew, D. G. T Parambi, A. Prabhu, M. S. Uddin, L. Aleya, H. Kim, B. Mathew, "Magnetic nanoparticles for hyperthermia in cancer treatment: an emerging tool," Environmental Science and Pollution Research, vol. 27, pp. 19214–19225, December 2019.

[4] T. Shinohara, T. Sato, and T. Taniyama, "Surface ferromagnetism of Pd fine particles," Physical Review Letters, vol. 91, 197201, November 2003.

[5] S. Angappane, J. Park, Y. Jang, T. Hyeon, and J.-G. Park, "Magnetic Pd nanoparticles: effects of surface atoms," Journal of Physics: Condensed Matter, vol. 20, 295209, July 2008.

[6] M. A. Miller, B. Askevold, H. Mikula, R. H. Kohler, D. Pirovich, and R. Weissleder, "Nano-palladium is a cellular catalyst for in vivo chemistry," Nature Communications, vol. 8, pp. 1–13, July 2017.

[7] S. Tarver, D. Gray, K. Loponov, D. B. Das, T. Sun, and M. Sotenko, "Biomineralization of Pd nanoparticles using phanerochaete chrysosporium as a sustainable approach to turn platinum group metals (pgms) wastes into catalysts," International Biodeterioration and Biodegradation, vol. 143, 104724, September 2019.

[8] S. Jang, S. A. Hira, D. Annas, S. Song, M. Yusuf, J. C. Park, S. Park, and K. H. Park, "Recent novel hybrid Pd–Fe_3O_4 nanoparticles as catalysts for various C–C coupling reactions," Processes, vol. 7, 422, July 2019.

[9] K. Deplanche, I. Caldelari, I. P. Mikheenko, F. Sargent and L. E. Macaskie, "Involvement of hydrogenases in the formation of highly catalytic Pd(0) nanoparticles by bioreduction of Pd(II) using Escherichia coli mutant strains," Microbiology, vol. 156, pp. 2630–2640, June 2010.

[10] L. E. Macaskie, V. S. Baxter-Plant, N. J. Creamer, A. C. Humphries, I. P. Mikheenko, P. M. Mikheenko, D. M. Penfold and P. Yong, "Applications of bacterial hydrogenases in waste decontamination, manufacture of novel bionanocatalysts and in sustainable energy," Biochem. Soc. Trans., vol. 33, pp. 76–79, February 2005.

[11] D. Passeri, C. Dong, M. Reggente, L. Angeloni, M. Barteri, F. A. Scaramuzzo, F. De Angelis, F. Marinelli, F. Antonelli, F. Rinaldi, C. Marianecci, M. Carafa, A. Sorbo, D. Sordi, I. WCE Arends, and M. Rossi, "Magnetic force microscopy. Quantitative issues in biomaterials," Biomatter, vol. 4, e29507, July 2014.

[12] G. Cordova, B.Y. Lee, and Z. Leonenko, "Magnetic force microscopy for nanoparticle characterization," NanoWorld Journal, vol 2, pp. 10-14, April 2016.

[13] B. Torre, G. Bertoni, D. Fragouli, A. Falqui, M. Salerno, A. Diaspro, R. Cingolani, and A. Athanassiou, "Magnetic, force microscopy and energy loss imaging of superparamagnetic iron oxide nanoparticles," Sci. Rep., vol.1, 202, December 2011.

[14] Sarid D, Scanning Force Microscopy. New York, USA: Oxford University Press, 1994.